



UCTEA Turkish Chamber of Civil Engineers

Teknik Dergi

Technical Journal

Volume 30 Issue 4 July 2019

TEKNİK DERGİ PUBLICATION PRINCIPLES

Teknik Dergi is a scientific and technical journal indexed by the Science Citation Index Expanded. Annually six issues are published, three in Turkish in the months of January, May and September, three in English in March, July and November. Its main principles of publication are summarized below:

1. Articles reporting original scientific research and those reflecting interesting engineering applications are accepted for publication. To be classified as original, the work should either produce new scientific knowledge or add a genuinely new dimension to the existing knowledge or develop a totally new method or substantially improve an existing method.
2. Articles reporting preliminary results of scientific studies and those which do not qualify as full articles but provide useful information for the reader can be considered for publication as technical notes.
3. Discussions received from the readers of the published articles within three months from publication are reviewed by the Editorial Board and then published together with the closing remarks of the author.
4. Manuscripts submitted for publication are evaluated by two or three reviewers unknown to the authors. In the light of their reports, final decision to accept or decline is taken by the Editorial Board. General policy of the Board is to get the insufficient manuscripts improved in line with the reviewers' proposals. Articles that fail to reach the desired level are declined. Reasons behind decisions are not declared.
5. A signed statement is taken from the authors, declaring that the article has not been published as a "journal article or book chapter". In case the Editorial Board is in the opinion that the article has already been published elsewhere with minor changes or suspects plagiarism or a similar violation of ethics, then not only that article, but none of the articles of the same authors are published.
6. Papers reporting works presented as conference papers and developed further may be considered for publication. The conference it was presented to is given as a footnote in the first page.
7. Additionally, a document signed by all authors, transferring the copyright to UCTEA Chamber of Civil Engineers is submitted together with the manuscript.



UCTEA Turkish Chamber of Civil Engineers

Teknik Dergi

Technical Journal

Volume 30 Issue 4 July 2019



UCTEA

Turkish Chamber of Civil Engineers

Necatibey St. No: 57, Kızılay 06440 Ankara, Turkey

Tel: +90.312.294 30 00 - Faks: +90.312.294 30 88

E-mail: imo@imo.org.tr - www.imo.org.tr

Publisher:

Cemal GÖKÇE

On behalf of UCTEA Turkish Chamber of Civil Engineers

Administrative Officer:

Bahaettin SARI

Volume 30 - Issue 4 - July 2019

Published bi-monthly. Local periodical.

Date of Print: 01 July 2019 / Number of copies: 1.000

Quotations require written approval of the Editorial Board.

ISSN: 1300-3453

Printed by:

Lotus Life Ajans Rek.Tan.Bas.Yay.Org.Amb.İth.İhr.San.ve Tic.Ltd.Şti.

Sokullu Cad. Perçem Sok. No: 9/A Çankaya / Ankara - Tel: 0.312.433 23 10

UCTEA Turkish Chamber of Civil Engineers

Teknik Dergi

Editorial Board:

Süheyl AKMAN
Ender ARKUN
İsmail AYDIN
Özer ÇİNİCİOĞLU
Metin GER
Gürkan Emre GÜRCANLI
Alper İLKİ
Cem OĞUZ
Kutay ORAKÇAL
Günay ÖZMEN
Baki ÖZTÜRK
İsmail ŞAHİN
Özkan ŞENGÜL
Tuğrul TANKUT

Editor in Chief:

Tuğrul TANKUT

Co-Editors:

Ender ARKUN
İsmail AYDIN
Özer ÇİNİCİOĞLU
Metin GER
Gürkan Emre GÜRCANLI
Alper İLKİ
Kutay ORAKÇAL
İsmail ŞAHİN
Özkan ŞENGÜL

English Proof Reader:

Ender ARKUN

Secretary:

Cemal ÇİMEN

Teknik Dergi is indexed by

- Science Citation Index Expanded
- Scopus
- Journal Citation Reports / Science Edition
- Engineering Index
- Concrete Abstracts (American Concrete Institute)
- National Technical Information Service (US NTIS)
- CITIS
- Ulrich's International Periodical's Directory
- TÜBİTAK / ULAKBİM

Teknik Dergi is a peer reviewed open access periodical publishing papers of original research and interesting practice cases. It addresses both the research community and the practicing engineers.

Reviewers:

This list is renewed each year and includes reviewers who served in the last two years of publication.

Ayda Şafak AĞAR ÖZBEK	Hilmi Berk ÇELİKOĞLU	M. Rifat KAHYAOĞLU	Mehmet SALTAN
Ragıp AKBAŞ	Kemal Önder ÇETİN	Volkan KALPAKÇI	Altuğ SAYGILI
Sami Oğuzhan AKBAŞ	Mecit ÇETİN	Erhan KARAESMEN	Hasan SAYGIN
Rıfat AKBIYIKLI	Reha ÇETİNKAYA	Halil KARAHAN	Neslihan SEÇKİN
Özge AKBOĞA KALE	Safiye Feyza ÇİNİCİOĞLU	Himmet KARAMAN	Serdar SELAMET
Burcu AKÇAY	Erdal ÇOKÇA	Mustafa KARAŞAHİN	Serdar SÖYÖZ
ALDANMAZ	Kutlu DARILMAZ	İlker KAZAZ	Ayşe Filiz SUNAR
Cihan Taylan AKDAĞ	Cem DEMİR	Cevza Melek	Erol ŞADOĞLU
Cem AKGÜNER	Ender DEMİREL	KAZEZYILMAZ ALHAN	Burak ŞENGÖZ
M. Vefa AKPINAR	Mehmet Cüneyd DEMİREL	Mustafa Kubilay	Aykut ŞENOL
Atakan AKSOY	Fatih DİKBAŞ	KELEŞOĞLU	Ali Ünal ŞORMAN
Zuhal AKYÜREK	Seyyit Ümit DİKMEN	Elçin KENTEL	Özcan TAN
Fatih ALEMDAR	İrem DİKMEN TOKER	Havvanur KILIÇ	Ali Hamza TANRIKULU
Pelin ALPKÖKİN	Ahmet Anıl DİNDAR	Ufuk KIRBAŞ	Serhan TANYEL
Sinan ALTIN	Emrah DOĞAN	Veysel Şadan Özgür KIRCA	Ergin TARI
Hilmi Doğan ALTINBİLEK	Nurhan ECEMİŞ ZEREN	Gökhan KIRKIL	Taha TAŞKIRAN
Adlen ALTUNBAŞ	Özgür EKİNCİOĞLU	Niyazi Uğur KOÇKAL	Gökmen TAYFUR
Fuat ARAS	Alper ELÇİ	Önder KOÇYİĞİT	Berrak TEYMUR
Davit ARDITI	Şebnem ELÇİ	Mete KÖKEN	H. Onur TEZCAN
Deniz ARTAN İLTER	Nilay ELGINÖZ KANAT	Ali Ümran KÖMÜŞÇÜ	Mesut TİĞDEMİR
Hakan Nuri ATAHAN	Murat Altuğ ERBERİK	Özgür KURÇ	Şahnaz TİĞREK
Shady ATTIA	E. Mete ERDEMGİL	Akif KUTLU	Vedat TOĞAN
Mustafa Tamer AYVAZ	Saffet ERDOĞAN	Semih KÜÇÜKARSLAN	Onur Behzat TOKDEMİR
Lale BALAS	Esin ERGEN PEHLEVAN	Hilmi LUŞ	Nabi Kartal TOKER
Selim BARADAN	Aysen ERGİN	Kasım MERMERTAŞ	Mustafa TOKYAY
Bekir Oğuz BARTIN	Gökmen ERGÜN	Mehmet Murat MONKUL	Ali TOPAL
Bilge BAŞ	Esra Ece ESELLER BAYAT	Yetiş Şazi MURAT	Cem TOPKAYA
Zeynep BAŞARAN	Tuğba ESKİŞAR TEFCİ	Elif OĞUZ	Ahmet TORTUM
BUNDUR	Güngör EVREN	Mehmet Hakkı OMURTAG	Gökçe TÖNÜK
Cüneyt BAYKAL	Antonio FORMISANO	Sema ONURLU	Nursu TUNALIOĞLU
Zerrin BAYRAKДАР	Nuray GEDİK	Engin ORAKDÖĞEN	Eda TURAN
İdris BEDİRHANOĞLU	Ergun GEDİZLIOĞLU	Şeref ORUÇ	Ahmet TÜRER
Serkan BEKİROĞLU	Haluk GERÇEK	Okan ÖNAL	Kaan TÜRKER
Mehmet BERİLGİN	İlgin GÖKAŞAR	Akın ÖNALP	Handan TÜRKOĞLU
Saadet Arzu BERİLGİN	Çağlar GÖKSU	Aybike ÖNGEL	Cüneyt TÜZÜN
Niyazi Özgür BEZGİN	Burcu GÜLDÜR ERKAL	Bihra ÖNÖZ	Eren UÇKAN
Selçuk BİLDİK	Fazlı Erol GÜLER	Ali Hakan ÖREN	Berna UNUTMAZ
Senem BİLİR MAHÇİÇEK	Zeynep GÜLERCE	Murat ÖZEN	Mehmet UTKU
Barış BİNİCİ	Taylan GÜNAY	Pelin ÖZENER	Volkan Emre UZ
İlknur BOZBEY	Necmettin GÜNDÜZ	Abdullah Tolga ÖZER	Deniz ÜLGEN
Zafer BOZKUŞ	Abdurrahman GÜNER	Eren Arman ÖZGÜVEN	Aslı ÜLKE KESKİN
Burcu BURAK BAKIR	Ülker GÜNER BACANLI	Hakkı Oral ÖZHAN	Alper ÜNLÜ
Erdem CANBAY	Aslı Pelin GÜRGÜN	Zeynep Huri ÖZKUL	Ahmet YAKUT
Zekai CELEP	İpek GÜRSEL DİNO	BİRGÖREN	İsmail Özgür YAMAN
Cihan CENGİZ	Gürşans GÜVEN İŞİN	Beliz ÖZORHON	A. Melih YANMAZ
Halim CEYLAN	Soner HALDENBİLEN	ORAKÇAL	Mert Yücel YARDIMCI
Ömer CİVALEK	Murat HAMDERİ	Sadık ÖZTOPRAK	Ufuk YAZGAN
Mustafa CÖMERT	Zeki HASGÜR	Turan ÖZTURAN	Anıl YAZICI
Ali Fırat ÇABALAR	Abdul HAYIR	Baki ÖZTÜRK	Emine Beyhan YEĞEN
Barlas Özden ÇAĞLAYAN	Nejan HUVAJ SARIHAN	Mustafa ÖZUYSAL	İrem Zeynep YILDIRIM
Özgür ÇAKIR	Zeynep İŞİK	Tolga Yılmaz ÖZÜDOĞRU	Koray Kamil YILMAZ
Gülben ÇALIŞ	Sabriye Banu İKİZLER	Nilüfer ÖZYURT	M. Tuğrul YILMAZ
Necati ÇATBAŞ	Eren İNCİ	ZİHNİOĞLU	Mehmet YILMAZ
Erkan ÇELEBİ	Pınar İNCİ	Bekir Yılmaz PEKMEZCİ	İsmail YÜCEL
Kutay ÇELEBİOĞLU	Erdal İRTEM	Şamil Şeref POLAT	Yeliz YÜKSELEN AKSOY
Ahmet Ozan ÇELİK	Recep İYİSAN	Gül POLAT TATAR	Nabi YÜZER
Oğuz Cem ÇELİK	Nihat KABAY	Selim PUL	Ahmet Şahin ZAİMOĞLU
Osman Nuri ÇELİK		Selman SAĞLAM	

UCTEA Turkish Chamber of Civil Engineers

Teknik Dergi

Volume: 30 Issue: 4 July 2019

CONTENTS

- Effects of Mixing Temperature on the Mechanical Properties of Hot Mix Asphalt... 9221
Gül BALIK, Mehmet YILMAZ, Baha Vural KÖK, Taner ALATAŞ
- Examination of the Efficiency of Retrofitting Methods through Fragility Analysis .. 9243
Murat S. KIRÇIL, Erdem Çağlar KOCABEY
- Timber Floors and Strengthening Techniques
(Illustrated With a Numerical Example)..... 9261
Žiga UNUK, Miroslav PREMROV, Vesna ŽEGARAC LESKOVAR
- Rotary Inertia and Higher Modes Effect on the Dynamic Response of
Timoshenko Beams on Two-Parameter Elastic Foundation..... 9289
Çağlayan HIZAL, Hikmet Hüseyin ÇATAL
- Roughness Coefficient of a Highly Calcinated Penstock..... 9309
Kutay ÇELEBIOĞLU
- Efficient Dynamic Analysis of Foundation via a Coupled Axisymmetric
SBFEM-3D FEM..... 9327
Mojtaba ASLMAND, Iradj Mahmoudzadeh KANI, Mehmet Cemal GENES

Effects of Mixing Temperature on the Mechanical Properties of Hot Mix Asphalt

Gül BALIK¹
Mehmet YILMAZ²
Baha Vural KÖK³
Taner ALATAŞ⁴

ABSTRACT

In this study, the effects of mixing temperature on the performance of hot mix asphalt (HMA) were investigated. 5% Styrene-butadiene-styrene (SBS) and 18% America Gilsonite were used as binder modifiers. HMA samples were prepared at the mixing temperatures 10°C, 15°C, and 20°C lower temperatures than the mixing temperature. Marshall Stability and flow, resistance to moisture-induced damage and indirect tensile fatigue tests were conducted on the hot mix asphalt samples. As a result of the experimental study, it was observed that use of additives increased the performance of the HMAs. In addition, it was seen that, in general, the stability, Marshall quotient, indirect tensile strength and fatigue life of the mixtures decreased and the flow values increased with decreasing mixing temperature.

Keywords: Mixing temperature, hot mix asphalt, styrene-butadiene-styrene, gilsonite, superpave, performance.

1. INTRODUCTION

Hot mix asphalts (HMAs), which can be used in the base and surface layers of flexible pavements, are comprised of bituminous binder and aggregate. Due to the rheological properties of bituminous binders, they act as an elastic solid at high vehicle speeds and low temperatures while demonstrating viscous liquid properties at low vehicle speeds and high-temperatures [1,2]. Because these properties of bituminous binders are reflected in the

Note:

- This paper has been received on March 14, 2018 and accepted for publication by the Editorial Board on November 12, 2018.
- Discussions on this paper will be accepted by September 30, 2019.
- <https://dx.doi.org/10.18400/tekderg.405948>

1 Firat University, Department of Civil Engineering, Elazığ, Turkey - guldoner23@hotmail.com
<https://orcid.org/0000-0001-7614-9862>

2 Firat University, Department of Civil Engineering, Elazığ, Turkey - mehmetyilmaz@firat.edu.tr
<https://orcid.org/0000-0002-2761-2598>

3 Firat University, Department of Civil Engineering, Elazığ, Turkey - bvural@firat.edu.tr
<https://orcid.org/0000-0002-7496-6006>

4 Firat University, Department of Civil Engineering, Elazığ, Turkey - talatas@firat.edu.tr
<https://orcid.org/0000-0002-2762-0440>

mixture, the rheological behaviors of bituminous binders are significant regarding pavement performance.

Various materials are added to the bituminous binders for different reasons and a modified kind of bitumen is obtained. The main reasons for bitumen modification are increases in the price of crude oil, consequently preference of thinner pavements due to high costs, significant increases in traffic loads, thereby shortening the service life of pavements, inability of classical binders to provide the desired level of performance, the inclination toward use of industrial wastes, the need for an increase in strength to prevent formation of deformations and high costs of maintenance [3].

Modifiers are substances, which can change the chemical, physical and/or mechanical properties of pure binders when added to pure binders. For a long time, researchers and chemists have conducted studies on modified bitumen. These studies were focused on the industrial utilization of graphite, specific fillers, mineral fibers, plastomers, elastomers and rubbers for bitumen modification [4-7]. The most commonly used modifiers are polymers [8]. Polymers are macromolecules, in which the same groups of atoms are repeated for several times [3]. Each repeated group can consist of one or several different molecules (monomer). Styrene-butadiene-styrene (SBS) block copolymers of the elastomer class increase the elasticity of bitumen and are the most suitable and commonly used polymer used in bitumen modification [9,10]. SBS copolymers provide their durability and elasticity due to the physical structure and cross binding of their molecules, which form a three-dimensional network. Polystyrene end-blocks increase the strength while polybutadiene elastic matrix blocks provide the extraordinary viscosity of the material [11]. When SBS is mixed with bitumen, the elastomeric phases of SBS copolymer absorb the oil fractions in bitumen and can swell about nine times of the initial volume [12]. In a suitable SBS concentration, a polymer phase is constantly formed during polymer modified bitumen (PMB) and the properties of pure binder change significantly.

Gilsonite, which is a member of the hydrocarbon class in bitumen additives and a natural bitumen source, contains hydrocarbons, which are 99% pure, and possesses a bitumen content, which varies between 57-70% [13,14]. Because Gilsonite is a substance that contains resin, it is used in various industrial fields [15]. Generally, Gilsonite is a by-product natural crude oil, and it splits from the rocks undergrounds and rises to the ground surface via the cracks in the surface layers. If the natural bitumen reaches ground surface, a bitumen source is formed. Otherwise, it stays underground, and if it stays isolated from the ground surface, it slowly hardens, becoming oxidized and eventually, it forms a solid and hard substance, which is the mineral bitumen. Gilsonite is a black and fragile substance and it can be turned into powder easily [16]. When Gilsonite is mixed with bitumen, its consistency increases. In addition to being mixed into bitumen, Gilsonite can also be added to the mixture [17]. As a result of the studies conducted on America and Iran Gilsonite, it was concluded that these additives improved the elasticity and high-temperature properties of bituminous binders [16, 18, 19, 20]. In another study, it was concluded that although America Gilsonite use increased the high-temperature behavior of bituminous binder, the practice also increased the crack formation possibility at low temperatures [21]. When aggregates are covered with Gilsonite modified bitumen, a notable interface is formed between the aggregate and the bitumen, thus, crack formation can be prevented in pavements [22]. It was also reported that Colombia Gilsonite, just as the Gilsonite from other countries, improved the high-temperature

properties of HMAs [23]. In previous studies, it was reported that Iran Gilsonite was more effective in terms of resistance to fatigue and permanent deformations as compared to America Gilsonite [24,25]. Gilsonite, due to its positive effects on bituminous binders and mixtures, especially on high-temperature resistance, is a considerable alternative material to polymers [26].

In order to obtain the expected performance of HMAs, they should be produced with suitable materials, designed in a suitable way as well as being produced under suitable conditions and in a suitable way. One of the parameters that affect the performance of HMAs is the mixing temperature. In general, a temperature range corresponding to 170 ± 20 cP is chosen for mixing and the range corresponding to 280 ± 30 cP is chosen for compaction [27]. These values are generally determined by rotational viscosimeter test. Although the mixing temperature of aggregate and bitumen is determined during the design process, the required temperature may not be achieved due to conditions, which occasionally result from personnel or equipment insufficiency.

According to data from 2015 in Turkey, the General Directorate of highways, special provincial administrations, municipalities and private firms possess 857 asphalt plants [28]. Although some of these plants go through regular maintenances and checks, some of them have over run their regular maintenance periods. Especially in several cities, it is believed that one of the reasons early deteriorations of the hot mix asphalt urban and village roads result from manufacturing defects.

In this study, the effects of mixing temperature on the performance of HMAs, which were prepared with modified binders, which contained commonly-used additives (SBS and Gilsonite). For this purpose, 5% styrene-butadiene-styrene (SBS) and 18% America Gilsonite (G) were used in the preparation of the modified bitumen. The mixing temperature was determined for pure bitumen and the modified bitumen. HMA samples were prepared at the determined mixing temperature and 10°C, 15°C and 20°C lower temperatures than mixing temperature. The prepared HMA samples were subjected to tests of resistance to moisture-induced damage, Marshall Stability and flow and indirect tensile fatigue. Thus, the effects of mixing temperature on the performance of HMAs were investigated.

2. MATERIALS AND METHODS

In this study, the effects of mixing temperature on the performances of HMAs prepared with pure bitumen and styrene-butadiene-styrene (SBS, obtained from the Shell Chemicals Company) and America Gilsonite (G, obtained from the American Gilsonite Company) modified bitumen. For preparing the modified binders, the pure bitumen and additives were mixed for 60 minutes at a temperature of 180°C in a mixer with a rotation rate of 1,000 rpm. As for the pure bitumen, PG 52-28 grade binder, which was obtained from the TÜPRAŞ refinery in Turkey, was used. The city with the warmest climate in Turkey, Şanlıurfa, was chosen as the city for investigation and the target performance level was chosen as PG 76-16 according to the temperature data. In order to achieve this performance level in previous studies, it was reported that it was necessary to use 5% SBS and 18% Gilsonite [29]. The results of the Superpave tests conducted on the binders were presented in Table 1.

Table 1 - DSR and BBR test results of neat and modified binders [29].

	Temp.(°C)	G*/sinδ (kPa) (specification limit min. 1 kPa)		
		PG 52-28	5% SBS	18% Gilsonite
DSR test results	52	2.021	-	-
	76	-	1.367	1.504
		G*/sin δ (kPa) RTFOT residue (specification limit min. 2.2 kPa)		
	52	8.782	-	-
	76	-	4.673	8.678
		G*.sin δ (kPa) PAV residue (specification limit max. 5000 kPa)		
	16	2023	-	-
	25	-	739	4213
	28	-	556	3186
	31	-	398	2345
BBR test results		m-value (specification limit min. 0.300)		
		PG 52-28	5% SBS	18% Gilsonite
	-6		0.330	0.333
	-12	-	0.291	0.294
	-18	0.562		
	-24	0.451		
		Creep stiffness (Mpa) (specification limit max. 300 MPa)		
	-6	-	43.2918	151.0398
	-12		76.790	283.9786
	-18	165.7		
-24	325.4			
Performance grades (PG)	52-28	76-16	76-16	

Bituminous binders should have viscosity values of 170 ± 20 cP during mixing with the aggregate and 280 ± 30 cP during laying out [30]. For this test, spindle No. 27 was chosen and the spindle speed was set to 20 rpm. Rotational viscometer tests were applied to pure and modified binders under two different temperatures (135 and 165°C). Viscosity-temperature graphs plotted with the obtained results were used to determine aggregate mixing temperatures and compaction temperatures. Findings obtained in the rotational viscometer test were presented in Table 2.

Similar to binder design, mix design was also conducted with the Superpave method as well. For this purpose, dense graded asphalt mixtures with crushed-stone aggregate suitable for

Superpave gradation and with a maximum size of 19 mm were prepared. The limestone type crushed aggregate was supplied from the Karayazı Region of the province of Elazığ. The properties of the aggregate were presented in Table 3. Additionally, the adopted gradation was presented in Figure 1.

Table 2 - Rotational viscosity test results [29].

Properties	Standard	PG 52-28	5% SBS	18% Gilsonite
Viscosity (cP, 135°C)	ASTM D4402	250.0	1513	1113
Viscosity (cP, 165°C)		100	487.5	287.5
Modification index ($\eta_{\text{modifiye}} / \eta_{\text{saf}}$, 135°C)	-	1.00	6.05	4.45
Modification index ($\eta_{\text{modifiye}} / \eta_{\text{saf}}$, 165°C)	-	1.00	4.88	2.88
Mixing temperature range (°C)	-	146.2-153.9	190.1-194.9	174.6-179.9
Compaction temperature range (°C)	-	130.5-137.4	175.8-181.5	163.8-168.5

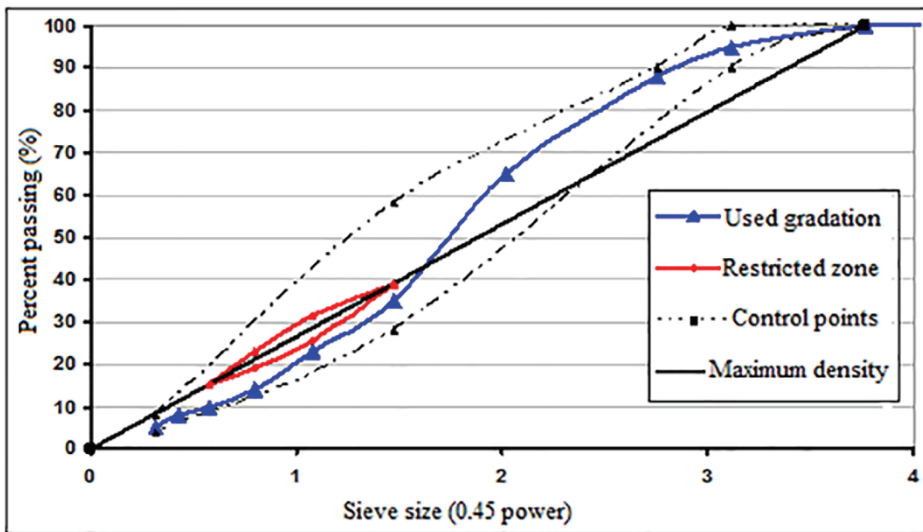


Figure 1 - Combined aggregate gradation.

As shown in Table 1, high-temperature resistance of binders was increased and low temperature resistance was decreased with additive use. The province of Şanlıurfa was

selected as the application area where the high temperature resistance of the binders is more important. Therefore, negativity at low temperature is not taken into account. When the rotational viscosity values given in Table 2 were examined, it was determined that the consistency of the binders increased with the use of additives. Due to the increase in viscosity, the mixtures prepared with modified bitumen required higher mixing and compaction temperatures.

Table 3 - Physical properties of the aggregate [29].

Properties	Standard	Specificati on limits	Coarse	Fine	Filler
Abrasion loss (%) (Los Angeles)	ASTM D 131	Max 30	29.2	-	-
Abrasion loss (%) (Micro deval)	ASTM D 6928	Max 15	17.4	-	-
Frost action (%) (with Na ₂ SO ₄)	ASTM C 88	Max 18	16.7	-	-
Methylene blue (gr/kg)	ASTM C 837	Max 1.5	0.5		
Specific gravity (g/cm ³)	ASTM C127		2.626	-	-
Specific gravity (g/cm ³)	ASTM C128		-	2.661	-
Specific gravity (g/cm ³)	ASTM D854		-	-	2.689

Superpave Gyrotory Compactor (SGC) which imparts a constant vertical pressure of 600kPa to the sample was used for sample compaction. SGC gyrates the sample with an eccentricity of 1.25° from the vertical axis. Design number of gyration was chosen as 100. In the study, the bitumen contents, which provide 4% air voids at determined mixing and compaction temperature, were obtained. In order to evaluate the effect of the decrease in the mixing temperature on the performance of the HMAs, the same bitumen contents were used in the mixtures prepared at different temperatures.

At the determined mixture and compaction temperatures, 4.61% bitumen was used in mixtures prepared with pure binders, 5.05% bitumen in mixtures prepared with 5% SBS modified bitumen, 4.91% bitumen in mixtures prepared with 18% Gilsonite modified bitumen [29]. In the contents of bitumen and 4 different mixing temperatures (at mixing temperature and 10°C, 15°C and 20°C lower than this temperature) mentioned in the study, the mixture samples were prepared. The mixing temperatures used in the study were presented in Table 4.

Marshall stability and flow (EN 12697-34), moisture-induced damage (AASHTO T 283) and indirect tensile fatigue (BS DD ABF) tests were performed on the mixtures prepared at different mixing temperatures. Thus, the effects of the change in mixing temperature on the fatigue, moisture-induced damage and stability of HMAs were evaluated.

Table 4 - Mixing temperatures of mixtures.

	Mixing temperature (°C)	Mixing temperature -10 (°C)	Mixing temperature -15 (°C)	Mixing temperature -20 (°C)
Abbreviations	1MT	MT-10	MT-15	MT-20
PG 52-28	150	140	135	130
5% SBS	193	183	178	172
18% Gilsonite	177	167	162	157

3. RESULTS AND DISCUSSION

In the study, Marshall Stability and flow test, resistance to moisture-induced damage and indirect tensile fatigue tests were conducted on the HMA samples prepared at 4 different mixing temperatures.

3.1. Marshall Stability and Flow Test Results

In this study, a total of 36 samples were prepared using 3 different binders (pure bitumen, 5% SBS and 18% Gilsonite modified bitumen) at 4 different mixing temperatures (MT, MT-10, MT-15 and MT-20) and these samples were subjected to Marshall stability and flow test according to EN 12697-34 standard. The prepared samples were kept in water, at 60°C, for 40 minutes and were cracked at 50.8 mm/min load speed. The final values were determined by multiplying the automatically determined stability values by the correction values, which depended on the height of the samples. The Marshall Stability values of the mixtures were presented in Figure 2 while the flow values were presented in Figure 3 and the Marshall Quotient (MQ) values were presented in Figure 4.

As it can be seen in Figure 2, the stability rates of mixtures prepared with 18% Gilsonite and 5% SBS modified bitumen were higher compared to the mixtures prepared with pure binder. It was determined that an irregular change occurred in the stability values of mixtures prepared with the pure binder with decreased mixing temperature. It was also observed that the differences between the values of the mixtures prepared with pure binder, the difference between the highest and lowest stability values were only 3.4%. Furthermore, it was observed that the values were close to each other in mixtures prepared with 5% SBS, the difference between the highest and lowest stability values were only 1.2% in mixtures prepared with 5% SBS modified bitumen. It was seen that the stability values reduced the most in mixtures prepared with 18% America Gilsonite modified binders by changing the mixing temperature. The highest stability values were obtained from the mixtures prepared at the mixing temperature and 10°C lower than the mixing temperature while the lowest stability values were obtained from the mixtures prepared at 20°C lower than the mixing temperature. It was observed that the difference between the highest and lowest stability values of the mixtures prepared with 18% Gilsonite modified bitumen were 36.6%.

Effects of Mixing Temperature on the Mechanical Properties of Hot Mix Asphalt

HMA wearing courses should have a minimum 900 kg Marshall stability value according to Technical Specifications of the Turkish General Directorate of Highways (TCK). As seen in Figure 2, all mixtures met the specification's requirements.

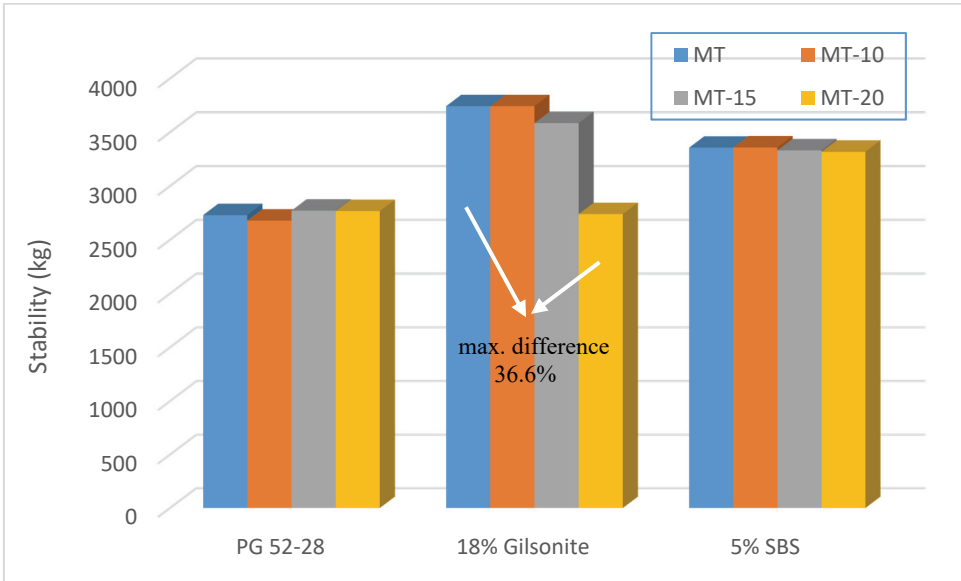


Figure 2 - Marshall stability values of mixtures.

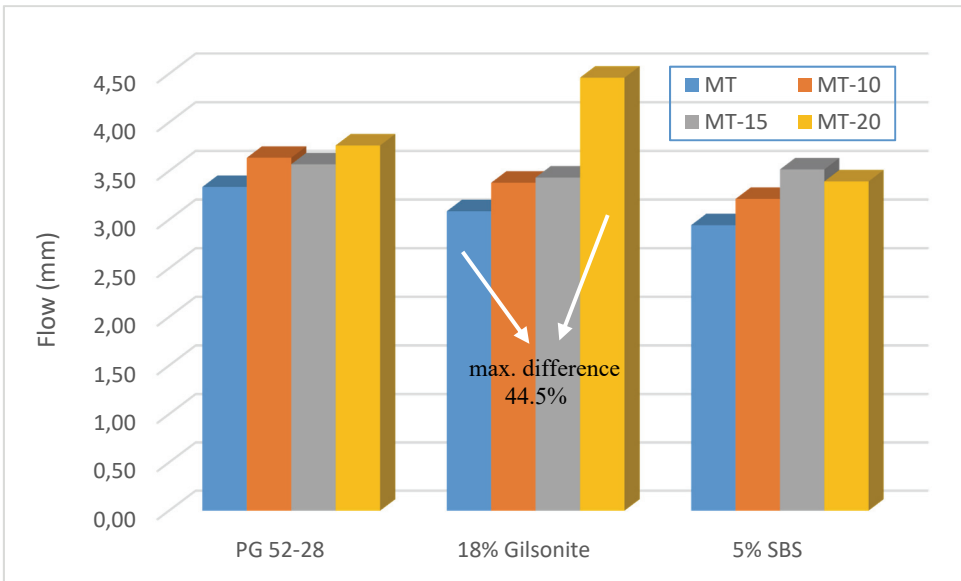


Figure 3 - Flow values of mixtures.

In the examination of the flow results in Figure 3, it was determined that the flow values were generally increased with decreased mixing temperature. It was observed that the flow values of all the mixtures were between 2-4 mm, meeting the criteria of the agreement, except for the mixtures prepared with 18% Gilsonite modified bitumen at 20°C lower than the mixing temperature. It was determined that the mixtures prepared with pure binders and 18% Gilsonite had the lowest flow value at the mixing temperature while the highest flow value was observed in mixtures prepared at 20°C lower than the mixing temperature. It was also seen that there was a 12.8% difference between the highest and the lowest flow values of mixtures prepared with pure binders while the difference was 44.5% in mixtures prepared with 18% Gilsonite. In mixtures prepared with 5% SBS, the lowest flow value was observed in the mixture prepared at the mixing temperature while the highest flow value was observed in the mixture prepared at 15°C lower than the mixing temperature. The difference between the highest and the lowest flow values of mixtures prepared with 5% SBS were 19.5%.

Flow values of HMA wearing courses should be between 2-4 mm according to Technical Specifications of the Turkish General Directorate of Highways. As seen in Figure 3, except mixtures prepared with 18% Gilsonite modified bitumen at 20°C lower than the mixing temperature, all mixtures met the specifications' requirements.

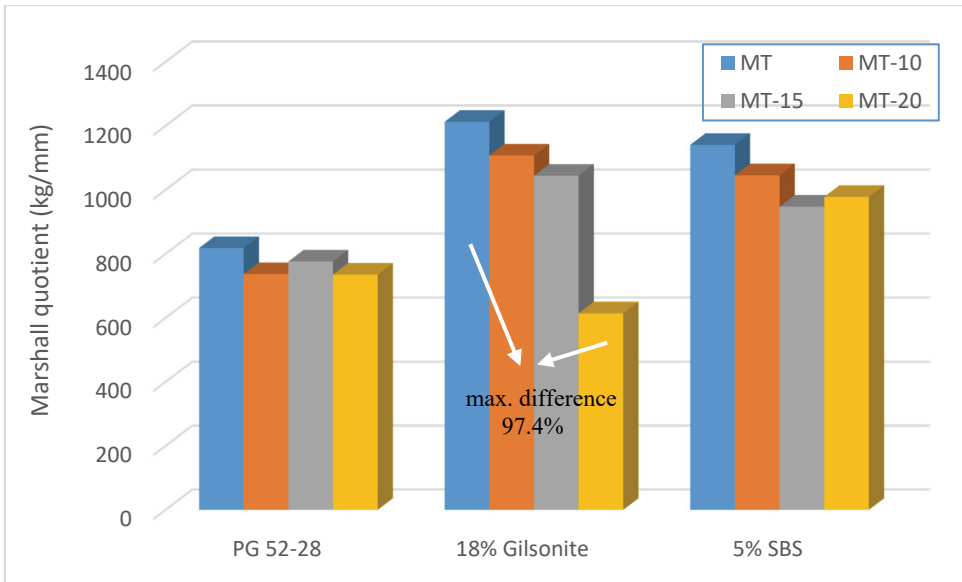


Figure 4 - MQ values of mixtures.

Marshall Quotient (MQ) value, which is the indicator of resistance to permanent deformation in HMAs, was determined by proportioning the stability values with flow values [31]. As it can be seen in Figure 4, with decreased mixing temperature, MQ values were generally decreased. It was maintained that the highest MQ values, thereby the highest resistance to permanent deformation, were obtained from mixtures prepared at the mixing temperature. The lowest MQ value was obtained from the mixtures prepared with pure binder and 18%

Gilsonite modified binders at 20°C lower than the mixing temperature and, for the mixtures prepared with 5% SBS modified bitumen, the lowest value was observed at mixtures prepared at 15°C lower than the mixing temperature. The difference between the highest and the lowest MQ values for mixtures prepared with pure bitumen was 11.3%, while the difference was 97.4% for the mixtures prepared with 18% Gilsonite and 20.4% for the mixtures prepared with 5% SBS modified bitumen.

3.2. Resistance to Moisture-Induced Damage

In order to determine the resistance to moisture-induced damage in the study, the samples were prepared and subjected to tests according to AASHTO T 283 standard. For 6 samples for each type of binder and each mixing temperature, a total of 72 Superpave HMA samples were prepared. In order to determine the moisture damages of the samples more clearly, the samples were prepared at $7\% \pm 0.5$ air voids. Then, the prepared samples were divided into two groups in a way that their specific weights are close to each other. After that, the first group was subjected to vacuuming in a way that their voids were filled with 70-80% water. Following this process, these samples were held at -18°C temperature for 16 hours and then held at 60°C water for 24 hours. While it was suggested to apply 1 cycle in the normal testing procedure, 5 freezing and thawing periods were applied in this study in order to determine the effects of mixing temperatures on the resistance to moisture-induced damage of HMAs. After the 5th period, the samples were kept in 25°C water for 2 hours and were cracked at the diametrical direction by applying a 50.8 mm/min loading rate. The second group of samples was kept in 25°C water for 2 hours and the samples were cracked by applying a 50.8 mm/min loading rate. Based on the maximum level of load at failure, the indirect tensile strength (ITS) in kPa is calculated by the following equation:

$$ITS = 2 * F / \pi * L * D \quad (1)$$

where F is the peak value of the applied vertical load (kN); L is the mean thickness of the test specimen (m); and D is the specimen diameter (m). In the study, the unconditioned samples were labeled as ITS_{uncond} , while the conditioned samples were labeled as ITS_{cond} .

The tensile strength ratio (TSR) value, which is an indicator of the resistance of the mixtures against moisture-induced damage, was determined as per the equation below:

$$TSR = 100 * (ITS_{cond} / ITS_{uncond}) \quad (2)$$

where ITS_{cond} is the indirect tensile strength of the conditioned specimens and ITS_{uncond} denotes the indirect tensile strength of the unconditioned specimens. The ITS_{uncond} values of the samples were presented in Figure 5 while the ITS_{cond} values were presented in Figure 6 and TSR values were presented in Figure 7.

In the examination of the ITS_{uncond} values (Fig. 5), it was observed that the ITS was increased significantly with additive usage. With decreased mixing temperature in pure mixture, a consistent reduction in ITS values was observed. In mixtures prepared with 18% Gilsonite and 5% SBS modified bitumen, with decreased mixing temperature, a consistent change was not observed in ITS values. In the pure mixture, the highest ITS value was observed in the

mixture prepared at the mixing temperature while the lowest value was observed at 20°C lower than the mixing temperature. It was determined that the difference between the highest and the lowest ITS value was 20.1%. In mixtures prepared with 18% Gilsonite modified bitumen, the highest value was observed at mixture prepared at 15°C lower than the mixing temperature while the lowest value was observed at the mixture prepared with at 10°C lower than the mixing temperature. For the mixtures prepared with 18% Gilsonite modified bitumen, the difference between the highest and the lowest ITS values was 6.5%. While the values in mixtures prepared with 5% SBS were rather close to each other, the highest value was observed in mixtures prepared at 10°C lower than the mixing temperature while the lowest value was observed at mixtures prepared at 20°C lower than the mixing temperature. The difference between the highest and the lowest ITS values was only 2.3%.

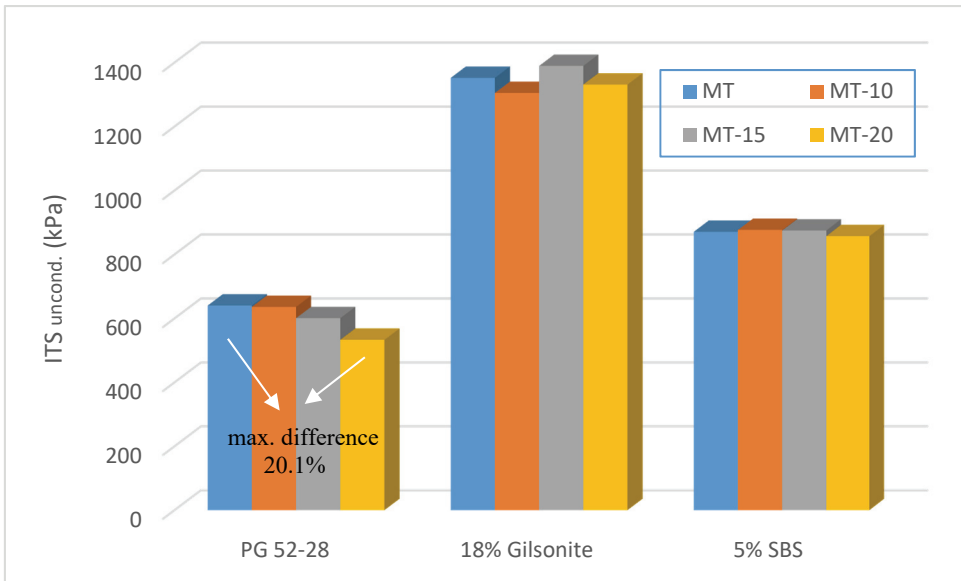


Figure 5 - ITS values of unconditioned mixtures.

In the observation of the ITS_{cond} in Fig. 6, it was observed that the ITS values of mixtures prepared with additives were higher compared to pure mixtures. Following the conditioning, while the ITS values of HMAs prepared with 5% SBS modified bitumen decreased consistently with decreasing mixing temperature, the ITS values of mixtures prepared with other binders (pure and 18% Gilsonite modified bitumen) did not demonstrate a consistent change with decreased mixing temperatures.

In mixtures prepared with pure binders, the highest value following the conditioning was observed in the mixtures prepared at 10°C lower than the mixing temperature while the lowest value was observed in mixtures prepared at 15°C lower than the mixing temperature. The difference between the ITS values of mixtures prepared with pure binders following the conditioning was 24.1%. In mixtures prepared with 18% Gilsonite, following the conditioning, the highest ITS value was observed in mixtures prepared at 15°C lower than

the mixing temperature while the lowest ITS value was observed in mixtures prepared at 10°C lower than the mixing temperature and the difference between the highest and the lowest ITS value was determined to be 22.7%. In mixtures prepared with 5% SBS modified bitumen, following the conditioning, the highest ITS value was observed in mixtures prepared at the mixing temperature and the lowest ITS value was observed in mixtures prepared at 20°C lower than the mixing temperature while the difference between the highest and the lowest ITS value was 7.0%.

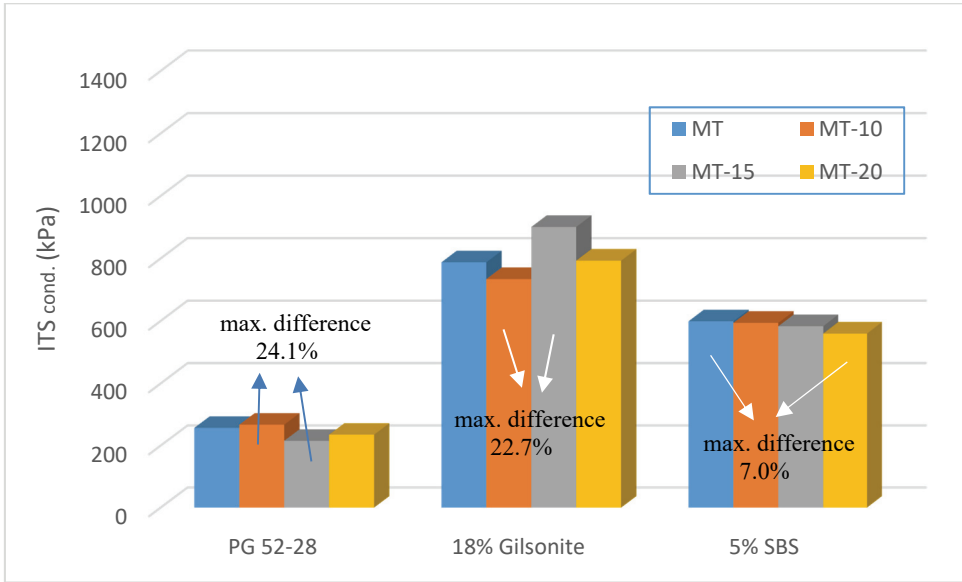


Figure 6 - ITS values of conditioned mixtures.

In the examination of the tensile strength ratio values in Fig. 7, it was determined that none of the mixtures met the criteria of Superpave specification limit (min. 80%) due to conditioning for 5 successive times. However, the fact that even the worst TSR value was around 40% following the 5th freezing and thawing cycle supported the idea that all the mixtures would meet the criteria of the agreement.

In the evaluation of the mixtures, it was observed that the lowest TSR value was of pure mixture while the highest TSR value was of the mixtures prepared with 5% SBS. The TSR value was observed to increase with additive usage. It was determined that SBS is more effective compared to Gilsonite in terms of resistance to moisture-induced damage.

In mixtures prepared with 5% SBS modified binder, with decreased mixing temperature, TSR values were consistently decreased while it was observed that these values did not consistently change in mixtures prepared with other two binders. In mixtures prepared with pure binders, the lowest TSR value was observed in mixtures prepared at 15°C lower than the mixing temperature while the highest value was observed that mixtures prepared at 20°C lower than the mixing temperature and the difference between the highest and the lowest values were 23.0%. In mixtures prepared with 18% Gilsonite modified binders, the highest

TSR rate was observed in mixtures prepared at 15°C lower than the mixing temperature while the lowest rate was observed in mixtures prepared at 10°C lower than the mixing temperature and the difference between the highest and the lowest rate was 15.2%. In the mixtures prepared with 5% modified binder, the highest tensile strength ratio was observed in mixtures prepared at the mixing temperature while the lowest rate was observed in mixtures prepared at 20°C lower than the mixing temperature and the difference between the highest and the lowest temperature was 5.3%.

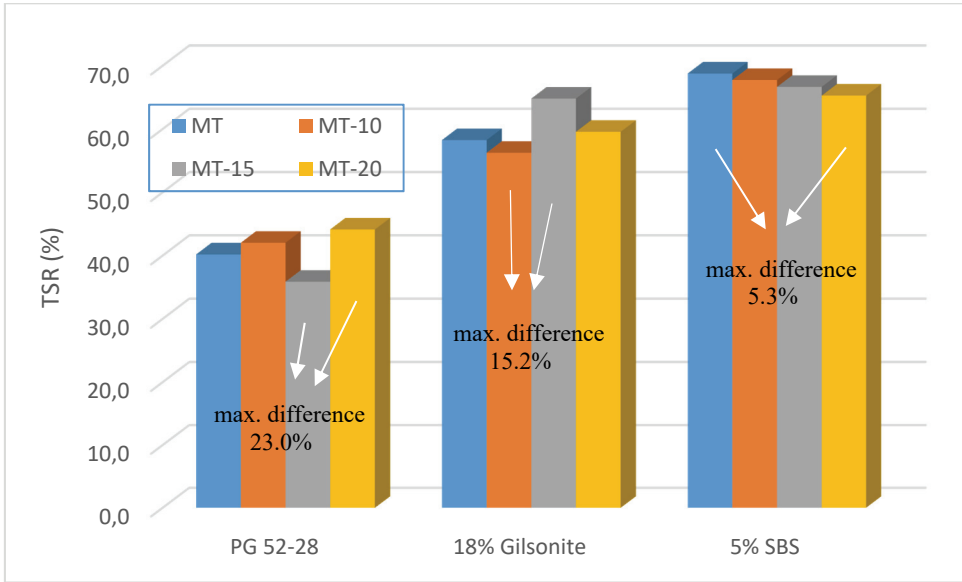


Figure 7 - TSR values of pure and modified binder included mixtures.

3.3. Indirect Tensile Fatigue Test Results

Indirect tensile fatigue tests were conducted on mixtures prepared with pure binders, 18% Gilsonite and 5% SBS modified bitumen at mixing temperatures of 10°C, 15°C and 20°C lower than the mixing temperature. The indirect tensile fatigue tests were performed in a controlled stress mode according to BS DD AFB standard [32]. 3 samples of each type of mixture, a total of 36 samples, were prepared for this test. The prepared samples were conditioned at 40°C for 3 hours. Then, repeated loading was applied by using Universal Test Machine (UTM). Because the main aim of the study is to investigate the effect of mixing temperatures on the performances of HMAs, fatigue tests at various stresses were conducted on each type of binder. In mixtures prepared with pure binders, the fatigue tests were conducted at 200 kPa stress level, in mixtures prepared with 18% Gilsonite modified bitumen, at 350 kPa stress level and in mixtures prepared with pure binders, at 250 kPa stress level.

Indirect tensile fatigue tests were continued until the sample failed. Thus, the deformation values in the maximum load cycle number and maximum load cycle number were obtained

via the software. As a result of the stress-controlled fatigue tests, the representative load repetition number-deformation level graph was plotted, see Fig. 8.

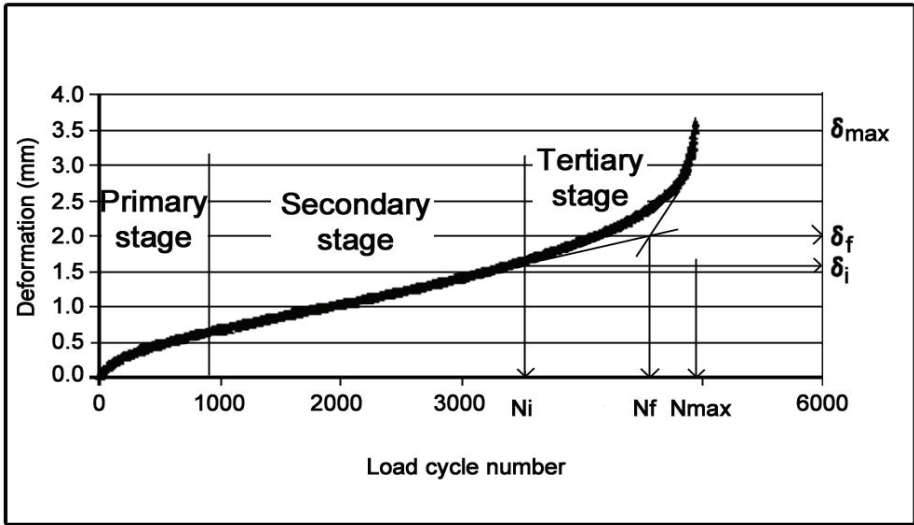


Figure 8 - A representative deformation-load repetition number relationship.

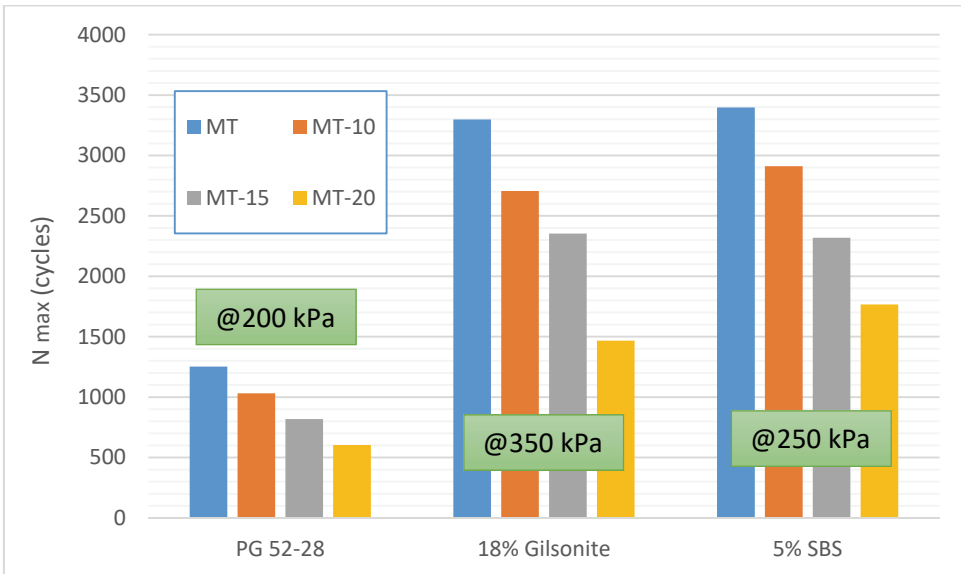


Figure 9 - The variation of N_{max} values of mixtures with the stress level and modifier type.

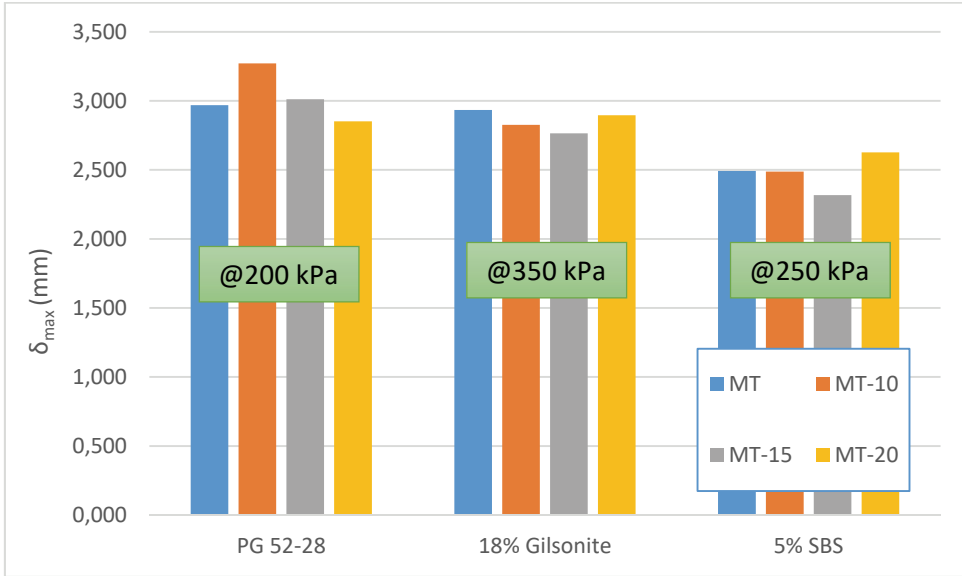


Figure 10 - The variation of δ_{max} values of mixtures with the stress level and modifier type.

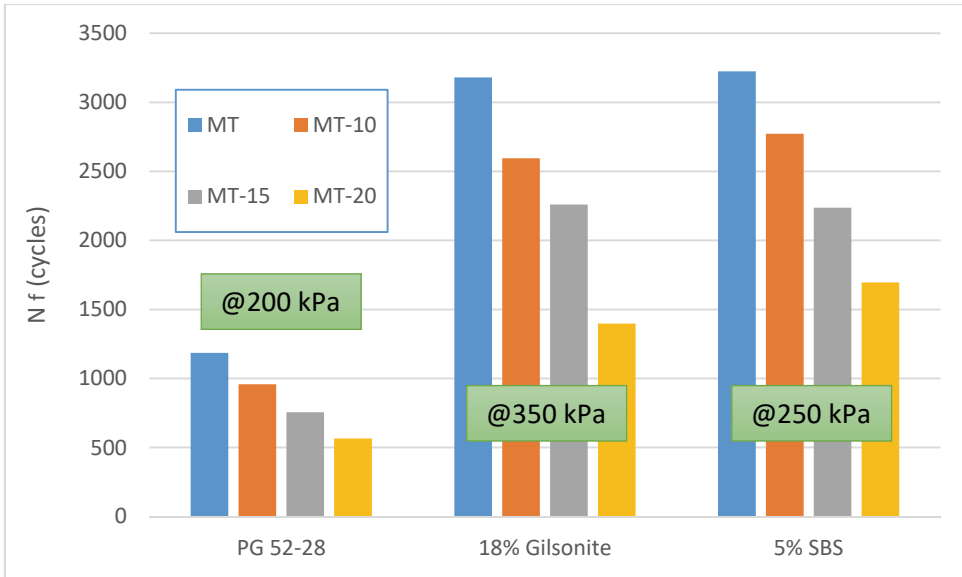


Figure 11 - N_f values of mixtures.

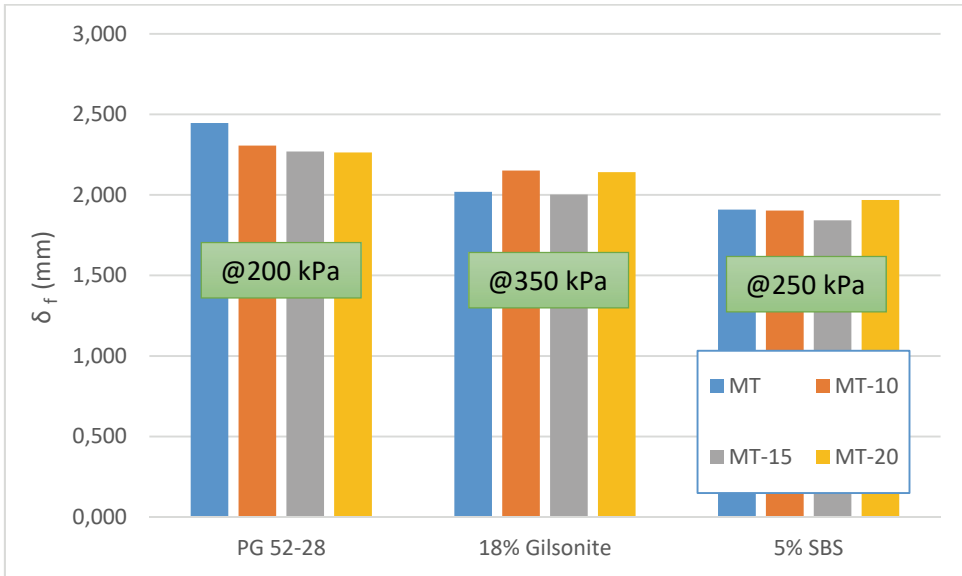


Figure 12 - δ_f values of mixtures.

Then, the results of the tests were transferred to Microsoft Excel and the fatigue lives of mixtures were determined by the junction points of 2nd and 3rd zones [33]. Additionally, maximum load cycle numbers (N_{max}) of mixtures were presented in Figure 9 and the deformation values at maximum load cycle number (δ_{max}) were presented in Figure 10 while the fatigue lives (N_f) were provided in Figure 11, the deformation values at fatigue lives (δ_f) were presented in Figure 12.

In the observation of the maximum load cycle numbers in Figure 9, even though the mixtures prepared with modified bitumen were subjected to higher stresses, it was determined that the maximum load cycle numbers were higher in mixtures prepared with modified bitumen. In the comparison of the type of additive, it was observed that even though mixtures prepared with 18% Gilsonite were subjected to higher stresses, they had similar maximum load cycle number with mixtures prepared with 5% SBS modified bitumen. Thus, the best results of these fatigue tests were obtained from mixtures prepared with 18% Gilsonite modified bitumen. It was also observed that in all of the binders, with decreased mixing temperature, the maximum load cycle number consistently decreased.

In mixtures prepared with pure binder at 10°C lower than the mixing temperature, the maximum load cycle number was decreased by 17.7% while at 15°C lower than the mixing temperature, it was 34.7% and at 20°C lower than the mixing temperature, it was decreased by 51.9%. In mixtures prepared with 18% Gilsonite modified binder, the maximum load cycle number decreased by 18.0%; 28.7% and 55.5% at 10°C, 15°C and 20°C lower than the mixing temperature, respectively. In mixtures prepared with 5% SBS modified binder, the maximum load cycle number decreased by 14.3%; 31.8% and 48.0% at 10°C, 15°C and 20°C lower than the mixing temperature, respectively. According to the obtained results, it was

determined that at 10°C and 20°C lower than the mixing temperature, the highest decrease was in mixtures prepared with 18% Gilsonite and at 15°C lower than the mixing temperature, the highest decrease was in mixtures prepared with pure bitumen. Especially at 20°C lower than the mixing temperature, the fact that the maximum load cycle number was decreased by approximately 50% demonstrated the significance of the mixing temperature in conditions with repeated loads.

In the observation of the deformation values in the maximum load cycle number of the mixtures (Fig. 10), it was determined that the highest deformation value in pure binder was in mixtures prepared at 10°C lower than the mixing temperature while the lowest deformation value was in mixtures prepared at 20°C lower than the mixing temperature. In the observation of mixtures prepared with 18% Gilsonite and 5% SBS, the lowest deformation value was in mixtures prepared at 15°C lower than the mixing temperature. These results indicated that the mixtures would have more brittle fractures in a situation where the mixture prepared with pure binder was prepared at 20°C lower than the mixing temperature and the mixtures prepared with 18% Gilsonite and 5% SBS modified bitumen prepared at 15°C lower than the mixing temperature.

In the observation of the fatigue lives of the mixture, it was determined that the changes were similar to those in the maximum load cycle number (Fig. 11). In mixtures prepared with pure binder, when the mixing temperature is 10°C lower than the mixing temperature, the number of fatigue life load cycle was decreased by 19.2% while at 15°C lower than the mixing temperature, it was decreased by 36.3% and 20°C lower than the mixing temperature, it was decreased by 52.3%. In mixtures prepared with 18% Gilsonite modified bitumen, with 10°C, 15°C and 20°C lower than the mixing temperature, the number of fatigue life load cycle were decreased by 18.4%; 28.9% and 56.0%, respectively. In mixtures prepared with 5% SBS modified bitumen, with 10°C, 15°C and 20°C lower than the mixing temperature, the number of fatigue life load cycle were decreased by 14.0%; 30.6% and 47.4%, respectively. According to the obtained results, it was determined that at 10°C and 15°C lower than the mixing temperature, the mixtures prepared with pure bitumen had the highest decrease in the number of fatigue life load repeated while at 20°C lower than the mixing temperature, the highest decrease was in mixtures prepared with 18% Gilsonite modified bitumen.

In the observation of the deformation values in fatigue lives of the mixtures (Fig. 12), it was observed that the lowest deformation value in mixtures prepared with pure binders was at 20°C lower than the mixing temperature while in mixtures prepared with 18% Gilsonite and 5% SBS modified bitumen, the lowest deformation value was in mixtures prepared at 15°C lower than the mixing temperature. This situation indicated that these mixtures would cause more brittle fractions.

4. SUMMARY AND CONCLUSIONS

In this study, three different types of binders (pure bitumen, 18% Gilsonite and 5% SBS modified bitumen) and limestone type crushed aggregate were used at 4 different mixing temperatures (the mixing temperature, 10°C, 15°C and 20°C lower than the mixing temperature) for the preparation of mixture samples. The values of mixing temperatures were determined by using the viscosity values (the values corresponding to 170 cP). The mixture samples were prepared by using Superpave gyratory compactor. By conducting Marshall

Stability and flow, resistance to moisture-induced damage and indirect tensile fatigue tests on the mixture samples, the effects of mixing temperatures on the performance of HMAs were investigated.

As a result of the Marshall Stability and flow tests, it was determined that the stability values were increased as a result of additive usage. Additionally, with declined mixing temperatures, the stability and MQ values of the mixtures were generally decreased and the flow rates increased. It was also determined that the mixture prepared with 18% Gilsonite was the one affected most by the changes in the mixing temperature.

In the comparison of the moisture-induced damage tests, with additive use both before and after the conditioning, it was determined that tensile strength values were increased. Gilsonite was more effective on tensile strength values compared to SBS. However, SBS was more effective in tensile strength ratio, which is an indicator for resistance to moisture-induced damage, compared to Gilsonite. In the evaluation of the effects of mixing temperature on ITS and TSR, while there was no consistent change, it can be concluded that with decreasing mixing temperatures, tensile strength values were decreased in general.

In the evaluation of the indirect tensile fatigue tests, it was observed that the fatigue lives of mixtures were increased with additive use. The most effective additive on indirect tensile fatigue test results was Gilsonite. With decreased mixing temperature, fatigue life values of all of the mixtures were decreased. This situation indicated that the decrease in the mixing temperature influenced the fatigue performance of the mixture negatively. In the evaluation of the deformation values, it can be concluded that with decreased mixing temperature, there was no consistent change.

When all the tests results were taken into consideration, it was concluded that additive use had positive effect on the performances of HMAs positively. Additionally, in cases where the mixing temperature is lower than what it is supposed to be, the performances of the mixtures would be affected negatively and especially the fatigue life would be affected substantially in a negative way. It was also determined that, in the evaluation of the effects of mixing temperature, dynamic test methods (indirect tensile fatigue) had more precise results compared to static test methods (Marshall stability and flow, indirect tensile strength). It can also be mentioned that in the HMAs produced for the investigation, attention paid to the mixing temperature of bitumen and aggregate in the plant is crucial for the performance of the mixture. In this study, only one type of aggregate and bitumen were used. Studies with materials obtained from different sources would further augment the validity of the results. Additionally, the effects on performance should be investigated in the event that when HMAs are prepared at higher temperatures than the indicated mixing temperature.

Symbols

- G* : Complex shear modulus
- HMA : Hot mix asphalt
- ITS : Indirect tensile strength
- MT : Mixing temperature

MQ	: Marshall quotient
Nf	: Fatigue live
Nmax	: Maximum load cycle number
PG	: Performance grade
SBS	: Styrene-butadiene-styrene
TSR	: Tensile strength ratio
UTM	: Universal Test Machine
δ	: Phase angle
Δf	: Deformation value at fatigue live
δ_{max}	: Deformation value at maximum load cycle number

References

- [1] Kök, B.V., Yılmaz, M., Kuloglu, N., Asfaltitin Bitüm ve Bitümlü Sıcak Karışımların Mekanik Özelliklerine Etkisi, İMO Teknik Dergi, 5813-5826, 2012.
- [2] Benhood, A., Olek, J., Rheological properties of asphalt binders modified with styrene-butadiene-styrene (SBS), ground tire rubber (GTR), or polyphosphoric acid (PPA), Construction and Building Materials, 151: 464–478, 2017.
- [3] Whiteoak, D., Shell Bitumen Handbook, Shell Bitumen UK, Riversdell House, 1990.
- [4] Zhu, J., Birgisson, B., Kiringos, N., Polymer modification of bitumen: advances and challenges, European Polymer Journal, 54: 18–38, 2014.
- [5] Ahmedzade, P., Alataş, T., Geçkil, T., Asfalt Betonunda Siyah Karbonun Filler Olarak Kullanımı, İMO Teknik Dergi, 4493-4507, 2008.
- [6] Kök, B.V., Yılmaz, M., Erkuş, Y., Effect of graphite on mechanical properties of stone mastic asphalt pavement, Journal of Civil Engineering and Management 23 (8): 1013-1020, 2017.
- [7] Topal, A., Evaluation of the properties and microstructure of plastomeric polymer modified bitumens, Fuel Processing Technology, 91 (1): 45-51, 2010.
- [8] Nejad, F.M., Azarhoosh, A.R., Hamed, G.H., Azarhoosh, M.J., Characterization of permanent deformation resistance of precipitated calcium carbonate modified asphalt mixture, Journal of Civil Engineering and Management, 21 (5): 615-622, 2015.
- [9] Şengöz, B., Işıkyakar, G., Analysis of styrene-butadiene-styrene polymer modified bitumen using fluorescent microscopy and conventional test methods, Journal of Hazardous Materials, 150: 424–432, 2008.
- [10] Kumar, K., Singh, A., Maity, S.K., Srivastava, M., Sahai, M., Singh, R.K., Garg, M.O., Rheological studies of performance grade bitumens prepared by blending elastomeric SBS (styrene butadiene styrene) co-polymer in base bitumens, Journal of Industrial and Engineering Chemistry, 44: 112-117, 2016.

- [11] Isacson, U., Lu, X., Testing and appraisal of polymer modified road bitumens: state of the art, *Materials and Structures*, 28: 139–159, 1995.
- [12] Cavaliere, M.G., Diani, E., Dia, M.D., Dynamic mechanical characterization of binder and asphalt concrete, *Proceedings of the Euroasphalt and Eurobitume Congress*, 7-10 May, Strasbourg, France, 1996.
- [13] Brown, S.F., Rowlett, R.D., Boucher, J.L., Asphalt modification, *Proceedings of the conference The United States strategic highway research program*, 29-31 October, London, England, 181–203, 1990.
- [14] Bahia, H.U., Hanson, D.I., Zeng, M., Zhai, H., Khatri M.A., Anderson, R.M., Characterization of modified asphalt binders in Superpave mix design, Project No. 9-10, Washington, DC: Transportation Research Board, 2001.
- [15] Davis N., Tooman, C.E., New laboratory tests evaluate the effectiveness of Gilsonite resin as a borehole stabilizer, *SPE Drilling Engineering*, 4(1): 47–56, 1989.
- [16] Ameri, M., Mansourian, A., Ashani, S.S., Yadollahi, G., Technical study on the Iranian Gilsonite as an additive for modification of asphalt binders used in pavement construction, *Construction and Building Materials*, 25: 1379–1387, 2011.
- [17] Bardesi, A., Brule, B., Corte, J.F., Diani, E., Gerritsen, A., Lefevre, G., Watkins, S., Use of modified bituminous binders, special bitumens and bitumens with additives in pavement applications, *Technical Committee Flexible Roads (C8) World Road Association (PIARC)*, Paris, France, 1999.
- [18] Widyatmoko, I., Elliott, R., Characteristics of elastomeric and plastomeric binders in contact with natural asphalts, *Construction and Building Materials*, 22: 239–249, 2008.
- [19] Babagoli, R., Hasaninia, M., Namazi, N.M., Laboratory evaluation of the effect of Gilsonite on the performance of stone matrix asphalt mixtures, *Road Materials and Pavement Design*, 16 (4): 889-906, 2015.
- [20] Jahanian, H.R., Shafabakhsh, G.H., Divandari, H., Performance evaluation of hot mix asphalt (HMA) containing bitumen modified with Gilsonite, *Construction and Building Materials*, 131: 156–164, 2017.
- [21] Anderson, D.A., Maurer, D., Ramirez, T., Christensen, D.W., Marasteanu, M.O., Mehta, Y., Field performance of modified asphalt binders evaluated with Superpave test methods, *Transportation Research Record*, 1661: 60–68, 1999.
- [22] Huang, B., Li, G., Shu, X., Investigation into three-layered HMA mixtures, *Composites*, 37: 679–690, 2006.
- [23] Quintana, H.A.R., Noguera, J.A.H., Bonells, C.F.U., Behavior of Gilsonite-modified hot mix asphalt by wet and dry processes, *ASCE Journal of Materials in Civil Engineering*, 28 (2): 04015114, 10.1061/(ASCE)MT.1943-5533.0001339, 2015.
- [24] Yilmaz, M., Yalcin, E., The effects of using different bitumen modifiers and hydrated lime together on the properties of hot mix asphalts, *Road Materials and Pavement Design*, 17 (2): 499-511, 2016.

- [25] Yilmaz, M., Çeloğlu, M.E., Effects of SBS and different natural asphalts on the properties of bituminous binders and mixtures, *Construction and Building Materials*, 44: 533-540, 2013.
- [26] Suo, Z., Wong, W.G., Analysis of fatigue crack growth behavior in asphalt concrete material in wearing course, *Construction and Building Materials*, 23: 462–468, 2009.
- [27] Asphalt Institute, Superpave mix designs, Superpave series no: 2, (SP-2), Asphalt Institute, Lexington, KY, USA, 2003.
- [28] Turkish Asphalt Contractors Association (ASMUD) technical datas, date of Access: 10.13.2018, <http://www.asmud.org.tr/asfalt.php?sayfa=25>.
- [29] Yilmaz, M., Yamaç, Ö.E., Evaluation of Gilsonite and styrene-butadiene-styrene composite usage in bitumen modification on the mechanical properties of hot mix asphalts, *ASCE Journal of Materials in Civil Engineering*, 29(9): 10.1061/(ASCE)MT.1943-5533.0001938, 2017.
- [30] Zaniwski, J.P., Pumphrey, M.E., Evaluation of performance graded asphalt binder equipment and testing protocol, Morgantown, WV: Asphalt Technology Program, Department of Civil and Environmental Engineering, 2004.
- [31] Zoorob, S.E., Suparna, L.B., Laboratory design and investigation of the properties of continuously graded asphaltic concrete containing recycled plastics aggregate replacement (plastiphalt), *Cement and Concrete Composites*, 22(4): 233–242, 2000.
- [32] BS DD ABF, Method for determination of the fatigue characteristics of bituminous mixtures using indirect tensile fatigue, Draft for Development, British Standards Institution, London, England, 1997.
- [33] Aragao, F.T.S., Lee, J., Kim, Y.R., Karki, P., Material specific effects of hydrated lime on the properties and performance behaviour of asphalt mixtures and asphaltic pavements, *Construction and Building Materials*, 24 (4): 538-544, 2010.

Examination of the Efficiency of Retrofitting Methods through Fragility Analysis

Murat S. KIRÇIL¹
Erdem Çağlar KOCABEY²

ABSTRACT

Turkey had several devastating earthquakes throughout its history as it is located in a highly seismically active region. Thus, seismic evaluation and retrofitting of the existing structures to decrease the potential damage of the future earthquakes is an essential part of the earthquake relief plans. The aim of this study is to examine the efficiency of widely used two retrofitting methods of existing structures through fragility analysis. Fragility curves are useful tools to show the probability of structural damage due to earthquakes as a function of ground motion indices. Fragility curves of a hypothetical residential building which represents the existing building stock have been generated. Furthermore, fragility curves of two retrofitted building have also been obtained. The first one is a frame with jacketed columns and the second one has shear walls added to the existing frame. Fragility curves have been obtained based on both local and global damage criteria limits in terms of interstory drift ratio. The obtained damage probabilities have shown that the damage criteria either local or global which are used for generation of fragility curves are significantly effective on the results. Differences in damage probability indicate the importance of the damage criteria and corresponding limits used for the determination of damage probability.

Keywords: Fragility curve, damage probability, incremental dynamic analysis.

1. INTRODUCTION

Damage, observed after past earthquakes, has emphasized the need for risk assessment of the existing building stock to estimate the potential damage of future earthquakes. The M_w 7.4 1999 Kocaeli and M_w 7.2 2011 Van earthquakes caused a considerable amount of economic losses, damage and a great number of casualties. This is due to not only the high seismicity but also due to the seismic vulnerability of the existing building stock. Most of the existing RC structures in Turkey are prone to earthquakes. Fragility curves allow estimation of the

Note:

- This paper has been received on March 20, 2018 and accepted for publication by the Editorial Board on December 24, 2018.
- Discussions on this paper will be accepted by September 30, 2019.
- <https://dx.doi.org/10.18400/tekderg.408126>

1 Department of Civil Engineering, Yildiz Technical University, İstanbul, Turkey - kircil@yildiz.edu.tr - <https://orcid.org/0000-0003-4447-9597>

2 Department of Civil Engineering, Yildiz Technical University, İstanbul, Turkey - erdemkocabey@gmail.com - <https://orcid.org/0000-0002-0750-6114>

probability of structural damage due to earthquakes as a function of ground motion indices. Thus, fragility curves of different types of structures have always been a subject of investigations which are performed for vulnerability assessment to estimate the potential damage that may be caused by future earthquakes. Several studies have been carried out all over the world to investigate the potential damage to the existing building stock [1-16]. In this study, the effectiveness of two widely used retrofitting methods has been investigated through fragility curves. Incremental dynamic analyses were performed for considered buildings to determine the threshold of different damage levels in terms of interstory drift ratio and fragility curves have been obtained based on the determined threshold values. Furthermore, threshold of damage levels obtained with different approaches are compared.

2. SAMPLE BUILDINGS

The structural system of a 6-story hypothetical sample building that consists of R/C frames in both two directions has been investigated. Fig.1 shows typical story plan of the sample building. The thickness of the concrete slab is 12 cm at each floor. Story height is 3.10m. Reinforcement type is S220 which has the characteristic yield strength of 220 MPa and mean concrete compressive strength is assumed to be 10 MPa considering the construction practice in Turkey before 2000. Those are realistic values for the buildings which are expected to exhibit poor performance during a severe earthquake.

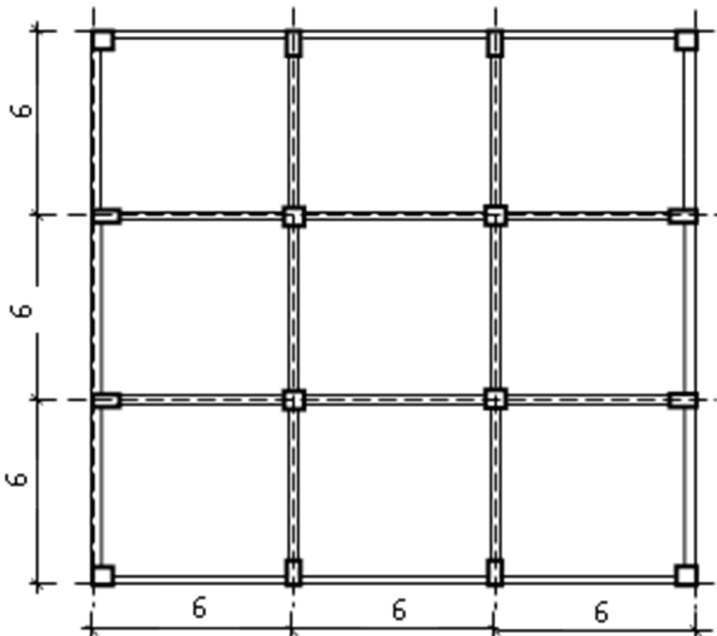


Figure 1 - Typical Story Plan of the Existing Building

Mean reinforcement ratio of columns is approximately 0.008 which is lower than the accepted minimum reinforcement ratio. Beam dimensions are 25x60cm and mean beam reinforcement ratio is approximately 0.0035. Typical deficiencies of such a building are material strength which is lower than the specified design strength and poor ductility of structural elements. The axial load on columns is higher than allowed especially in lower floors. Strong column and weak beam rule is not satisfied and also there is no confinement effect on structural members because of insufficient lateral reinforcement. The first mode period of the existing building, calculated with effective stiffness of structural elements, is 1.46s.

Although the main portion of the existing building stock does not have such a regular structural system, a regular plan building is used within the scope of this study to rationalize the structural behavior; so that, improvement in structural performance provided by each retrofitting method can be easily compared.

The assumed transverse reinforcement spacing is 25cm since the existing buildings do not have adequate shear reinforcement to provide a significant confinement effect. Even 25cm may be thought as low considering the shear reinforcement spacing of the significant portion of the existing building stock; however, it's high enough so that the confinement effect can be neglected. The calculated shear reinforcement spacing for retrofitting jackets is about 8-10cm and shear reinforcement of jackets are taken into account for the calculation of the confinement effect. Figure 2 shows few example sections for beams and columns.

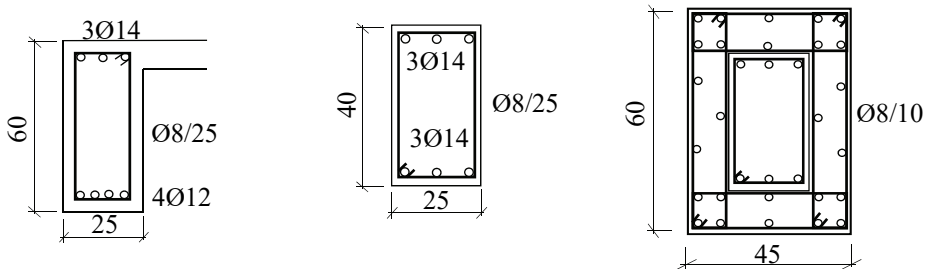


Figure 2 - Sample Sections for Existing Beam, Column and Retrofitted Column

As mentioned earlier, two different options which are widely used for retrofitting of the R/C structures were investigated within the scope of this study. The first one is jacketing columns of the existing structure and the latter is adding shear walls to the existing structural system. Jacketing improves strength of columns and also helps to improve strong column-weak beam behavior. The characteristic concrete strength of the jacket is 30MPa and characteristic yield strength of the reinforcing steel of the additional elements is 420MPa. The floor plan of the structure, retrofitted by jacketing columns, is shown in Fig 3. The jacketing thickness is 10cm and not constant because of the decreasing existing column dimensions through the building height. Thus, thickness of jacket increases up to 20cm especially at upper floors so that a constant column section can be provided. The authors believe that constant dimensions of jacketed columns, along the height of retrofitted building, is an advantage to provide strong

column-weak beam behavior and additional lateral stiffness to the retrofitted structure. The first mode vibration period of the retrofitted building, calculated with effective stiffness of structural elements, is 0.49s.

Another widely used method for strengthening is adding new shear walls to the structural system. This option provides strength and stiffness rather than ductility. New shear walls reduce the shear force and bending moment on the existing columns since they reduce the lateral displacement of the structure. However, ductility and ultimate strength of the existing columns is still low since their rotational capacity and strength can't be increased. Fig. 4 shows the floor plan of the structure with shear walls. The first mode vibration period of this building, calculated with effective stiffness of structural elements, is 0.40s.

The shear and bending reinforcement of all additional structural elements are determined based on the provisions given by TSDC[17] and TS500[18] using the internal actions obtained for the building located in Earthquake Zone 1 and Site Class B. The observed failure type of shear walls is bending. The shear failure for those shear walls are not expected considering that their mean shear capacity ratio is approximately equal to 0.87 in case of collapse and their height/length ratio 3.10.

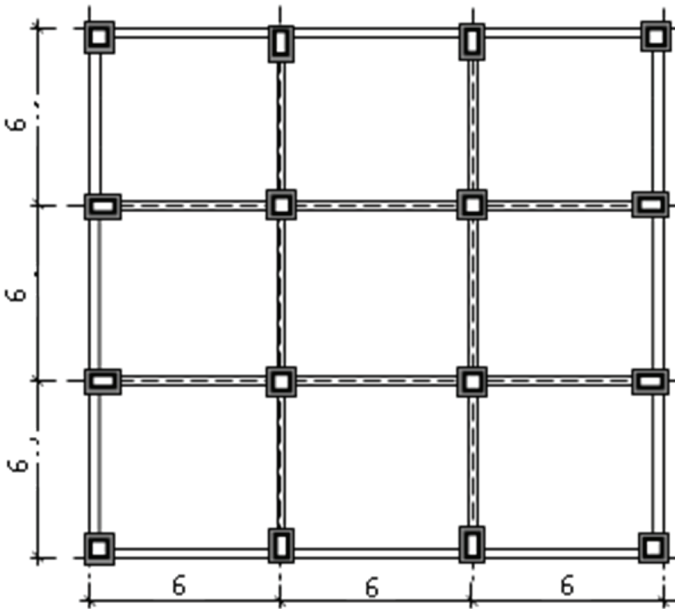


Figure 3 - Typical Floor Plan of the Sample Building (Retrofitted with Column Jacketing)

Although main portion of the existing building stock does not have such a regular structural system, a regular plan building is used within the scope of this study to refine the structural behavior; so that, improvement in structural performance provided by each retrofitting method can be easily compared.

3. GROUND MOTIONS

The random nature of the earthquakes makes the damage estimation problem probabilistic. 13 ground motion record of 8 earthquakes with different magnitude, PGA and source distance have been used in this study to be able to take the random nature of the earthquakes into account. All the considered earthquakes are shown in Table 1. Note that, both X and Y component of Friuli, Colinga, Kocaeli (Eregli) and Kocaeli (Tekirdag) ground motions are used for analysis. All the selected ground motion records were recorded on Site Class B since the sample building is assumed to be constructed on this type of soil. Table 1 shows the considered earthquakes.

Table 1 - Ground Motions

Event	Year	Mag.	R _{RUP} (km)	PGA(g)	Site Class
Kocaeli, Turkey (Eregli)	1999	7.51	58.3	0.06	B
Kocaeli, Turkey (Tekirdag)	1999	7.51	16.4	0.12	B
Coalinga (Perkfield-Cholame)	1983	6.36	42	0.62	B
San Fernando (Upland – San Antonio Dam)	1971	6.61	46.8	0.62	B
Friuli (Barcis)	1976	6.5	49.1	0.25	B
Imperial Valley (Pachute test site)	1977	6.53	50.1	0.11	B
Loma Prieta (Saratoga)	1989	7.58	8.5	0.51	B
Landers (Amboy)	1992	7.28	69.2	0.1	B
Northridge (Castaic)	1994	6.69	20.11	0.46	B

4. DAMAGE LEVELS

For the present study, 3 different approximations have been adopted to determine the threshold of damage levels in terms of inter-story drift ratio. The first one is analytic which is based on the determination of the mean inter-story drift limits obtained from incremental dynamic analyses at different damage states. The considered damage states are Slight, Minimum, Extensive and Collapse, respectively. The inter-story drift ratio limit for slight damage is assumed to be the inter-story drift ratio at first reinforcement yield in either column or beam section. Inter-story drift ratio limits for minimum and extensive damage level have been determined based on the strain limits given by the Turkish Seismic Design Code [17] as shown in Table 2.

The minimum damage limit is assumed as the inter-story drift ratio related to the first minimum section damage of a structural system element. The max. inter-story drift ratio of extensive damage limit is assumed to be reached at first beam section collapse based on the strain limits given in Table 2. The partial collapse limit corresponds to max. inter-story drift ratio at first column section collapse and finally collapse limit is defined as the max. inter-story drift ratio causing frame mechanism.

Table 2 - Strain Limits of Section Damage Levels

Section damage level	Strain limit for concrete	Strain limit for reinforcement
Minimum	0.004 (Unconfined)	0.01
Extensive	$0.004+0.0095(\rho_s / \rho_{sm}) \leq 0.0135$ (confined)	0.04
Collapse	$0.004+0.013(\rho_s/\rho_{sm}) \leq 0.0180$ (confined)	0.06

Note that the approximation given above, which is used for linking the inter-story drift ratio and strain limits given by Turkish Seismic Design Code[17], is subjective. On the other hand, Turkish Seismic Design Code[17] defines structural performance levels based on the rate of the damaged structural elements at each story. However, this approximation is not practical for such a study. Table 3 shows the drift ratio limits obtained following the procedure explained above. Those mean inter-story drift ratio limits will be called local damage criteria in the remaining part of the text since they have been determined using the local damage limits.

Table 3 – Inter-story Drift Limits Corresponding to Local Section Damages

Damage level	Mean interstory drift ratio (%)		
	Existing	Jacketing	Shear wall
Slight	0.2	0.3	0.2
Minimum	1.5	1.8	0.9
Extensive	-	3.7	-
Part. collapse	2.7	6.6	3.3
Collapse	5.4	7.1	5.5

The extensive damage limit is defined as first section collapse of a beam section as mentioned above. As seen from Table 3, the extensive damage limit could not be determined for the existing and the retrofitted building with shear walls, since strain limit of the collapse section damage for columns is reached before strain limit of collapse section damage for beams with a little increase in spectral acceleration. It is believed that the main reason is strong beam-weak column mechanism commonly encountered in such buildings.

The second approximation is based on the global damage levels and corresponding inter-story drift limits proposed by Rosetto and Elnashai [19]. Table 4 shows the aforementioned limits. Finally, the last approximation is the determination of yield and collapse states analytically through the incremental dynamic analysis following the definitions given by Vamvatsikos and Cornell [20]. Results are shown in Table 5. Inter-story drift ratio limits, given in Table 4 and 5, are based on the global structural behavior while those given in Table 3 are based on the local section damage limits.

Table 4 – Inter-story Drift Limits (Global)

Damage level	Interstory drift ratio (%)
Light	0.19
Moderate	0.56
Extensive	1.63
Part. collapse	3.34
Collapse	>4.78

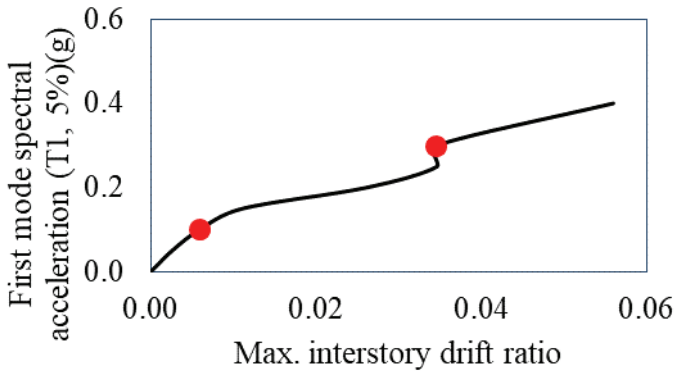
Table 5 - Interstory Drift Limits Obtained With Incremental Dynamic Analysis

Damage level	Mean inter-story drift ratio (%)		
	Existing	Jacketing	Shear wall
Yield	0.8	0.69	0.28
Collapse	3.06	4.39	2.17

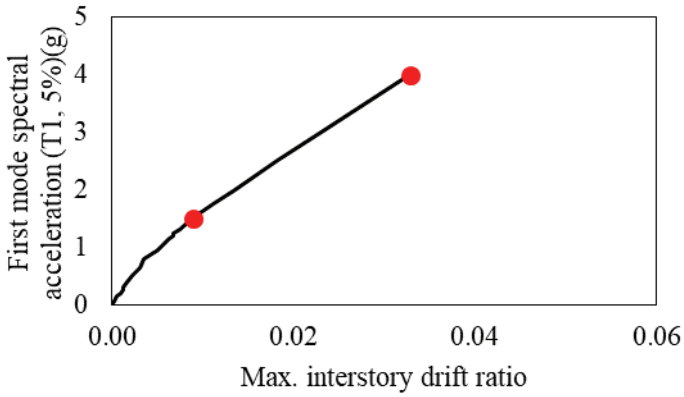
5. INCREMENTAL DYNAMIC ANALYSIS

Incremental dynamic analysis (IDA) has been used to determine the damage thresholds corresponding to aforementioned damage levels. This method was discussed comprehensively by Vamvatsikos and Cornell [20]. IDA is a useful method to produce curves which show the relationship between the selected ground motion intensity measure versus the selected damage indicator. For this study 5% damped elastic spectral acceleration and maximum inter-story drift ratio is selected as intensity and damage measure, respectively. Each ground motion is scaled up monotonically with respect to the individual spectral acceleration based on the corresponding fundamental period of the considered building. Thus, the maximum inter-story drift ratio, obtained for each step of IDA, is the result of a non-linear time history analysis which is carried out for a certain elastic spectral acceleration. Up to the yield point, the relationship between spectral acceleration and the maximum inter-story drift ratio is linear. However, the curve leaves the linear path as soon as a yielding which causes a significant decrease in the slope of the curve –in other word stiffness of the structure- is observed. When the slope of the curve decreases 20% of the initial slope of the IDA curve then the analyzed structure is assumed to have collapsed [20]. If dynamic instability as a result of non-converging run is observed before IDA curve's slope decreases to the limit value mentioned above then spectral acceleration level of the non-converging run is assumed as the collapse capacity. Seismostruct [23] has been used as a structural analyses software tool for IDA. Seismostruct uses the Newmark scheme with automatic time-step adjustment for optimum accuracy for the direct integration of the equations of motion during time history analysis of a 3-dimensional model. The considered hysteretic behavior of reinforcement and concrete are Bilinear and Mander model [17, 21], respectively. The fiber section model has been used which considers strain of each point of the section based on the aforementioned material models. Rigid diaphragm behavior of the slabs is considered during the analyses.

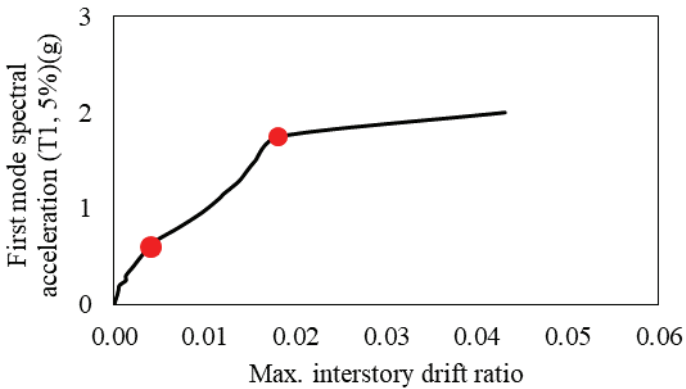
Fig. 5 shows typical IDA curves of the considered buildings obtained for Imperial Valley ground motion. Yield and collapse points are indicated on the figure.



(a) IDA Curve of the Existing Building



(b) IDA Curve of the Retrofitted Building by Jacketing Columns



(c) IDA Curve of the Retrofitted Building by Adding Shear Walls

Figure 5 - IDA Curves Obtained for Imperial Walley Ground Motion

All IDA curves obtained for all the considered building are given in Fig. 6, Fig.7 and Fig. 8 with their yield and collapse point.

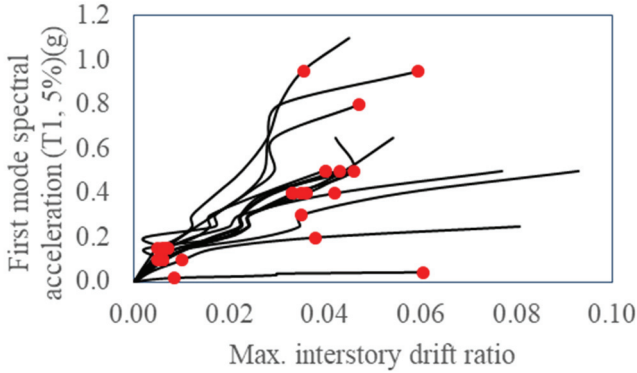


Figure 6 - All IDA Curves Obtained For the Existing Structure

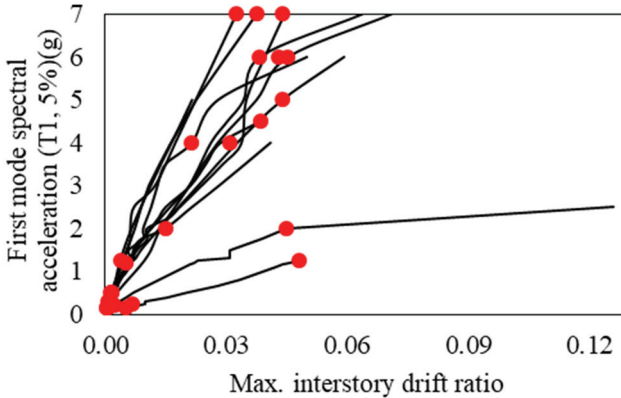


Figure 7 All IDA Curves Obtained For the Retrofitted Building by Jacketing the Columns

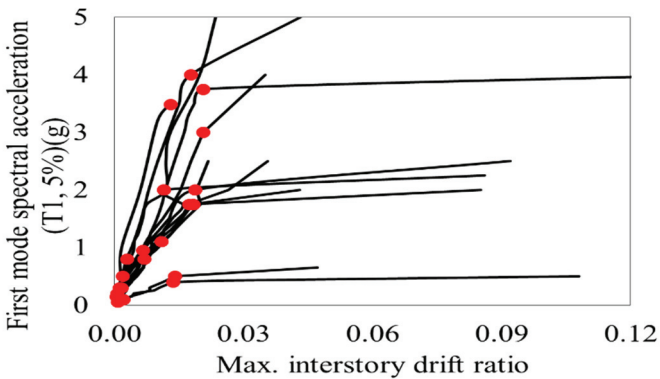


Figure 8 All IDA Curves Obtained For the Retrofitted Building by Adding Shear Walls

6. FRAGILITY CURVES

Fragility curves express the probability of structural damage due to earthquakes as a function of ground motion indices. In the present study, fragility curves are constructed in terms of elastic spectral acceleration as mentioned before. Fragility curves can be expressed in the form of two-parameter lognormal distribution functions. Based on this assumption, the probability of reaching or exceeding a limit state (LS) at a given earthquake intensity can be expressed as follows

$$P(LS) = P(d_{LS} \leq d_{max}) = 1 - \Phi(r) \quad (1)$$

where d_{LS} and d_{max} are limit state capacity and maximum demand, respectively. By assuming a lognormal distribution, the standard normal variant can be expressed as follows

$$r = \frac{\ln d_{LS} - \lambda_D}{\sqrt{\xi_{LS}^2 + \xi_D^2}} \quad (2)$$

where λ_D is mean value with lognormal distribution and it can be expressed in terms of the mean of the maximum response (d_{max}) and its dispersion (ξ_D).

$$\lambda_D = \ln \bar{d}_{max} - \frac{\xi_D^2}{2} \quad (3)$$

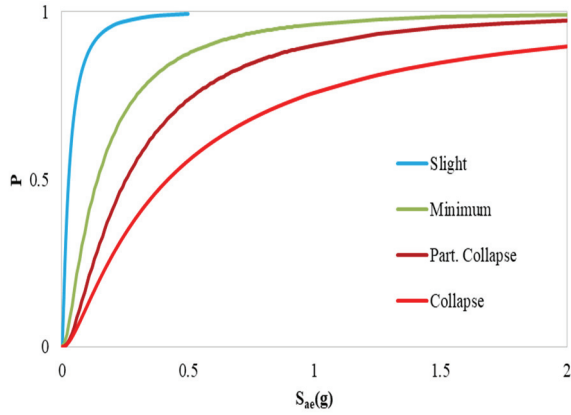
ξ_{LS} is the lognormal standard deviation of a limit state. It is assumed to be 0.3 for the limits given in Table 4 by following the Jeong and Elnashai [22]. Lognormal standard deviation of other limit states, given in Table 3 and 5 were calculated using the results obtained from IDA.

The dispersion of maximum demand ξ_D is obtained as the combination of uncertainties associated with demand estimation as follows

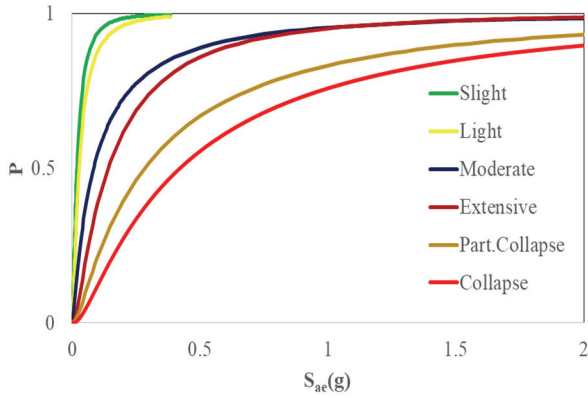
$$\xi_D = \sqrt{\ln \left(1 + \left(\frac{\sigma_r}{\bar{d}_{max}} \right)^2 \right) + \ln \left(1 + \left(\frac{\sigma_c}{\bar{d}_{max}} \right)^2 \right) + \ln \left(1 + \left(\frac{\sigma_D}{\bar{d}_{max}} \right)^2 \right)} \quad (4)$$

where σ_r and σ_c are the standard deviations due to randomness in earthquake records and material properties, respectively. σ_r is considered by using 13 ground motion records. The dispersion in material properties has been considered using the standard deviation of 5 MPa following the Bartlett and MacGregor [23]. σ_D is standard deviation of structural response. Fig.9-11 show the fragility curves obtained for all considered buildings.

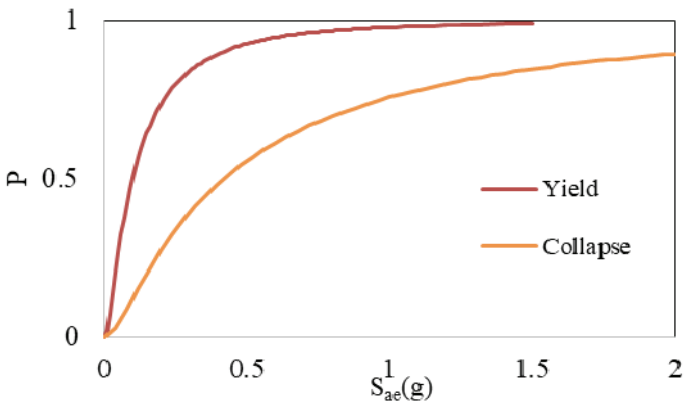
The target performance of earthquake resistant design of a residential buildings is to satisfy the Immediate Occupancy (IO), Life Safety (LS) and Collapse Prevention (CP) performance levels under the effect of earthquakes with probability of exceedance of 50%, 10% and 2%, respectively. Table 6, 7 and 8 show the probability of exceedance of the considered performance levels under the effect of earthquakes given by TSDC[17] for Earthquake Zone 1 and Site Class B with aforementioned probability of exceedance. The slight, extensive and partial collapse damage levels, given in Table 3, are related to IO, LS and CP performance levels, respectively.



(a) Fragility Curves of the Existing Building (Local Damage Criteria)

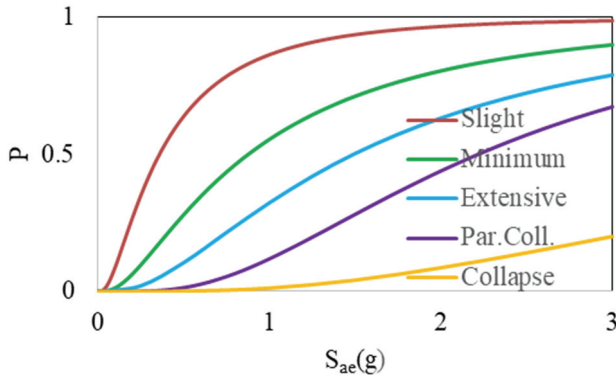


(b) Fragility Curves of the Existing Building (Global Damage Criteria)

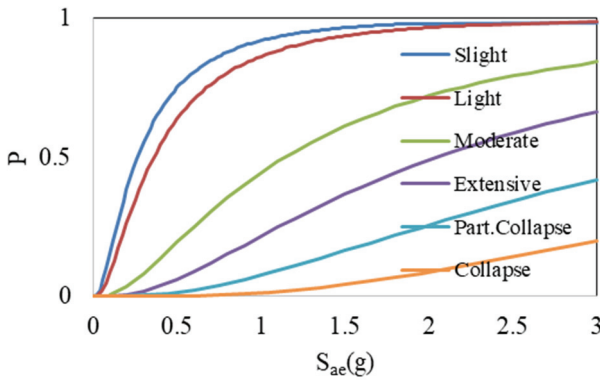


(c) Fragility Curves of the Existing Building (Global Damage Criteria / IDA)

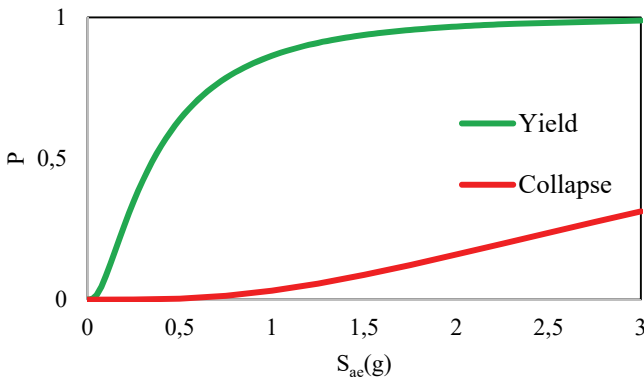
Figure 9 - All IDA Curves Obtained for the Existing Building



(a) Fragility Curves of the Retrofitted Building with Jacketed Columns (Local Damage Criteria)

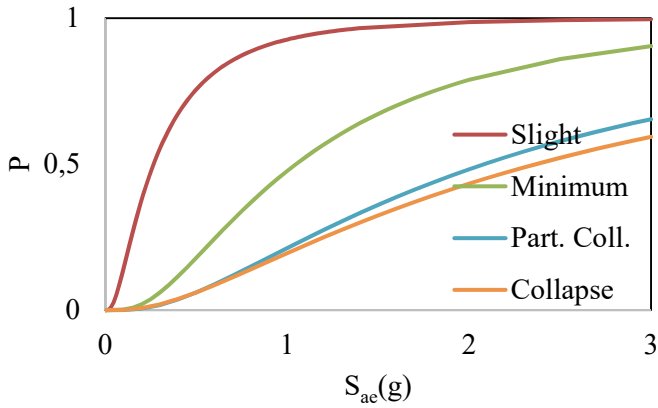


(b) Fragility Curves of the Retrofitted Building with Jacketed Columns (Global Damage Criteria)

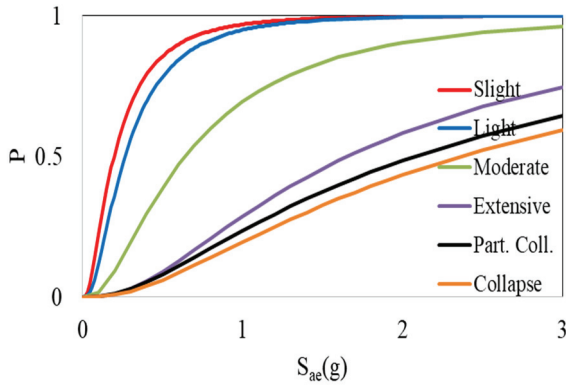


(c) Fragility Curves of Retrofitted Building with Jacketed Columns (Global Damage Criteria / IDA)

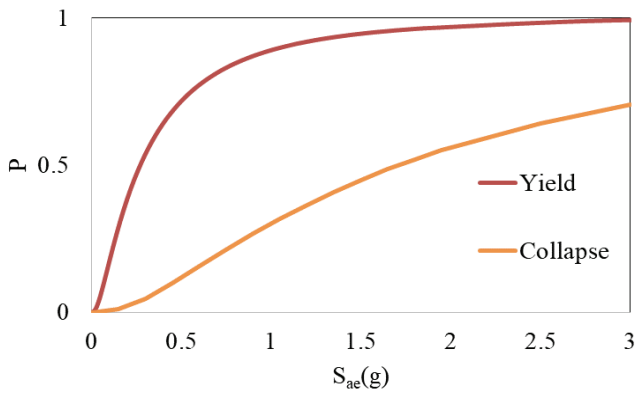
Figure 10 - Fragility Curves of the Retrofitted Building with Jacketed Columns



(a) Fragility Curves of the Retrofitted Building with Shear Walls (Local Damage Criteria)



(b) Fragility Curves of the Retrofitted Building with Shear Walls (Global Damage Criteria)



(c) Fragility Curves of Retrofitted Building with Shear Walls (Global Damage Criteria/IDA)

Figure 11 - Fragility Curves of the Retrofitted Building With Shear Walls

The strain limit of the (partial) collapse section damage for columns. (collapse limit) has been reached before the strain limit of collapse section damage for beams (extensive damage limit) with a little increase in spectral acceleration for both existing and retrofitted (shear wall) structure. Thus, the probability of reaching life safety performance level could not be obtained for those buildings in case of using local damage criteria. Light, Moderate and Partial Collapse damage levels, given in Table 4, are related to IO, LS and CP performance levels, respectively. The performance levels are connected to damage levels based on the definitions of performance and damage levels.

Table 6 - Damage Probability for Target Performance (Local Damage Criteria)

Probability of exceedance in 50 years	Immediate Occupancy	Life Safety	Collapse Prevention
Existing			
%50	98		
%10		-	
%2			74
Jacketing			
%50	58		
%10		55	
%2			39
Shear wall			
%50	76		
%10		-	
%2			34

Table 7 - Damage Probability for Target Performance (Global Damage Criteria)

Probability of exceedance in 50 years	Immediate Occupancy	Life Safety	Collapse Prevention
Existing			
%50	96		
%10		85	
%2			68
Jacketing			
%50	58		
%10		38	
%2			12
Shear wall			
%50	78		
%10		69	
%2			37

Table 8 - Damage Probability for Target Performance (Global Damage Criteria / IDA)

Probability of exceedance in 50 years	Yielding		Collapse
		Existing	
%50	69		
%10		-	
%2			57
		Jacketing	
%50	57		
%10		-	
%2			6
		Shear wall	
%50	70		
%10		-	
%2			45

As it is seen from the Tables 6-8, both retrofitting methods decrease the damage probability significantly. There is almost no difference between the probability of reaching IO Performance Level, obtained with local and global damage criteria (Table 6 and 7).

In case of using the local damage criteria (Table 6), the highest decrease in probability of exceeding the IO performance level is provided by the jacketing, while the highest decrease in probability of CP performance level is provided by shear walls. However; the difference in the probability of exceeding CP performance level of both retrofitting methods is not significant.

Jacketing is the most efficient method to decrease the damage probability in case of using global damage indicators since it provides significant decrease in damage probability at each considered performance level (Table 7) as compared with strengthening with shear walls. The authors believe that the main reason of this significant decrease is strong column-weak beam behavior which is provided by the increase in the strength and deformation capacity of the jacketed columns. This enhancement in strength can be observed from the IDA curves given in Fig.5. Note that improvement in the behavior of the building with jacketing depends on the shear reinforcement of jackets so that the premature shear failure can be prevented. In this study, it is assumed that sufficient amount of transverse reinforcement will be provided in jacketed columns.

7. CONCLUSIONS

Finally, the following conclusions can be drawn from the results of this study in addition to the discussion above:

- It is observed that analytic collapse probability (IDA) of the existing and the retrofitted

buildings by jacketing (%57, %6) are lower than the probability of CP performance level obtained based on either local (%74, %39) or global (%68, %12) damage limits and there is a reasonable margin between probability of reaching analytic collapse state obtained with IDA and that of collapse prevention performance level determined with both global and local criteria.

- However, as it is seen from Tables 6-8, the probability of reaching collapse state determined through IDA for the retrofitted building with shear walls (Table 8) is higher than the probability of reaching CP performance level determined with local and global damage criteria given in Table 6 and 7. This result shows that both local and global criteria for CP performance level, given in codes or proposed by other researchers, are not always consistent with the analytic collapse limit. However, this observation must be verified by examining more sample structures with different amount of shear wall area so that it can be determined whether shear dominated behavior of the structure is effective on this observation or not. Strengthening with shear walls is almost inevitable with increasing building height so that lateral displacements can be limited. In such a case, analytic collapse limit should be determined and used as the upper limit or inter-story drift ratio of collapse instead of the collapse limit given by codes or other similar documents.
- The Immediate Occupancy Performance Level is defined by Turkish Seismic Design Code [19] as “none or negligible damage” in structural system. Furthermore, yielding capacity determined via IDA represents the onset of yielding. Thus, it is expected to have similar probability of reaching the yielding and the IO performance level. The probability of reaching the Immediate Occupancy Performance Level determined with local and global criteria and the probability of yield determined with IDA are similar (%58, %58, %57) only for the retrofitted building with jacketing. However, yielding probability of the existing building (%69) is significantly lower than the probability of reaching the IO Performance Level (98%, 96%). Yielding probability (70%) of the retrofitted building with shear walls is still lower than the probability of reaching IO Performance Level given in Table 6 and 7 (76% and 78%). However; the difference is not as significant as observed for the existing building.

Those differences in damage probability indicate the importance of the damage criteria and corresponding limits used for the determination of damage probability. Damage state or performance level limits -either local or global- must be selected carefully and upper and lower limits (onset of yield and collapse), at least, must be determined analytically so that realistic estimations can be made.

Note that local damages such as shear or axial failure of structural system elements are not considered within the scope of this study; so that, the retrofitting methods can be compared clearly. On the other hand, those failure types can be observed during the evaluation and design process and they may require application of some local strengthening techniques to prevent brittle failure of those elements. However, it is believed that the existence of this type of deficiencies (when they don't change the global structural behavior significantly) does not cause significant changes in the observations which are made within the scope of this study.

A building with a regular plan has been investigated so that the individual effect of considered retrofitting methods can be compared clearly; however, the plan layout of the main portion of the existing building stock is not as regular as such. Therefore, for a building with a highly

irregular plan, the probable strengthening method will be the combination of the considered methods within the scope of this study.

References

- [1] Ay, B. Ö., Erberik, M. A., Vulnerability of Turkish Low-Rise and Mid-Rise Reinforced Concrete Frame Structures. *J. Earthq. Eng.*, 12(S2), 2–11, 2008.
- [2] Kirçil, M. S., Polat, Z., Fragility analysis of mid-rise R/C frame buildings. *Eng. Struct.*, 28(2006), 1335-1345, 2006.
- [3] Borekci, M., Kirçil M.S., Fragility analysis of R/C frame buildings based on different types of hysteretic model. *Struct. Eng. Mech.*, 39(6), 795–812, 2011.
- [4] Martins , L., Silva, V., Marques, M., Crowley, H., Delgado, R., Development and assessment of damage-to-loss models for moment-frame reinforced concrete buildings. *Earthq. Eng.& Struc. Dyn.*, 45(5), 797–817, 2016.
- [5] Akkar, S., Sucuoglu, A. Displacement-Based Fragility Functions for Low- and Mid-rise Ordinary Concrete Buildings. *Earthq. Spect.*, 21(4), 901-927, 2005.
- [6] Langa, K., Bachmann, H. (2004), On the Seismic Vulnerability of Existing Buildings: A Case Study of the City of Basel. *Earthq. Spect.*, 20(1), 43–66, 2004.
- [7] Kazantzi, A.K., Righiniotis, T.D., Chryssanthopoulos, M.K., A Simplified Fragility Methodology for Regular Steel MRFs. *J. of Struct. Eng.*, 15, 390–403, 2011.
- [8] Ji, J., Kuchma, A.D., Elnashai, A.S., Seismic Fragility Relationship of Reinforced Concrete High-Rise Buildings. *The Struc. Des. Tall and Special Buildings*, 18, 259-277, 2009.
- [9] Ellingwood, B.R., Celik, O.C., Kinali, K., Fragility assessment of building structural systems in Mid-America. *Earthq. Eng.& Struc. Dyn.*, 36, 1935–1952, 2007.
- [10] Pasticier, L., Amadio, C., Fragiacomio, M., Non-linear seismic analysis and vulnerability evaluation of a masonry building by means of the SAP2000 V.10 code. *Earthq. Eng.& Struc. Dyn.*, 37, 467-485, 2008.
- [11] Inel, M., Ozmen, H.B., Seismic performance evaluation of school buildings in Turkey. *Struct. Eng. Mech.*, 30(5), 535-558, 2008.
- [12] Senel, S.M., Kayhan, A.H., Fragility based damage assesment in existing precast industrial buildings: A case study for Turkey. *Struct. Eng. Mech.*, 34(1), 39-60, 2010.
- [13] Silva, V., Crowley, H., V., Humberto, Pinho, R., Sousa, L., Investigation of the characteristics of Portuguese regular moment-frame RC buildings and development of a vulnerability model. *Bull. of Earthq. Eng.*, 13(5), 1455-1490, 2015.
- [14] Jeong, S.H., Mwafy, A.M., Elnashai, A.S., Probabilistic seismic performance assessment of code-compliant multi-story RC buildings. *Eng. Struct.*, 34 (2012), 527–537, 2012.

- [15] Casotto, C., Silva, V., Crowley, H., Nascimbene, R., Pinho, R., Seismic fragility of Italian RC precast industrial structures. *Eng. Struct.*, 94 (2015), 122–136, 2015.
- [16] Hueste, M.B.D., Bai, J.W., Seismic retrofit of a reinforced concrete flat-slab structure: Part II-seismic fragility analysis. *Eng. Struct.*, 29 (2007), 1178–1188, 2007.
- [17] Turkish Seismic Design Code, Specifications for buildings to be built in seismic zones, Ankara, Turkey, Ministry of Public Works and Settlement, 2007.
- [18] Requirements for Design and Construction of Reinforced Concrete Structures TS 500, Ankara, Turkey, Turkish Standard Institution, 2000.
- [19] Rosetto, T. and Elnashai, A.E., Derivation of vulnerability functions for European-type RC structures based on observational data. *Eng. Struct.*, 25(10), 1241-1263, 2003.
- [20] Vamvatsikos, D., Cornell, C.A., Incremental Dynamic Analysis. *Earthq. Eng. & Struct. Dyn.*, 31(3), 491-514, 2001.
- [21] Seismostruct, Software for Finite Element Analysis of Structures, Seismosoft Inc., Pavia, Italy, 2014. www.seismosoft.com/seismostruct
- [22] Jeong, S.H., Elnashai, A.S., Probabilistic fragility analysis parameterized by fundamental response quantities. *Eng. Struct.*, 29 (2007), 1238–1251, 2007.
- [23] Bartlett, F.M., MacGregor, J.G., Statistical Analysis of the Compressive Strength of Concrete in Structures. *ACI Materials J*, 93(2), 158-168, 1996.

Timber Floors and Strengthening Techniques (Illustrated With a Numerical Example)

Žiga UNUK¹

Miroslav PREMROV²

Vesna ŽEGARAC LESKOVAR³

ABSTRACT

The trend of renewing old masonry buildings and provision of new housing, public and other areas without using new building blocks is becoming increasingly important to ensure the conformity of the renovated buildings with the current technical regulations. One compliance aspect is the load-bearing function, which to a large degree depends on the floor structures. As old masonry buildings often have timber floors, the purpose of this article is to provide insight into the field of timber floor strengthening. Thus, the evolution of floor structures is briefly presented, and common types of timber floors are provided. Furthermore, the weight of different timber floor fillings is studied in relation to the prescribed imposed loads. Measures for strengthening old timber floors are introduced separately in view of vertical and horizontal strengthening. Additionally, a classic timber floor and a timber-concrete composite floor are analyzed regarding current building standards in the European Union, the Eurocodes.

Keywords: Floor structures, timber floors, strengthening, timber-concrete composite, Eurocodes.

1. INTRODUCTION

A frequent situation in building renewal is the change of the category of use, which can in certain cases lead to the requirement imposing higher incident loads and consequently to necessity for structural improvement of the existing structure. Nonetheless, even a change in a standard can increase the minimum incident load, which can be related to the progress of the housing culture and/or policy changes. In the studied case, special attention must be paid

Note:

- This paper has been received on March 22, 2018 and accepted for publication by the Editorial Board on December 24, 2018.
- Discussions on this paper will be accepted by September 30, 2019.
- <https://dx.doi.org/10.18400/tekderg.408857>

1 University of Maribor, Faculty of Civil Engineering, Transportation Engineering and Architecture, Maribor, Slovenia - ziga.unuk@um.si - <https://orcid.org/0000-0001-6143-2569>

2 University of Maribor, Faculty of Civil Engineering, Transportation Engineering and Architecture, Maribor, Slovenia - miroslav.premrov@um.si - <https://orcid.org/0000-0003-3717-8235>

3 University of Maribor, Faculty of Civil Engineering, Transportation Engineering and Architecture, Maribor, Slovenia - vesna.zegarac@um.si - <https://orcid.org/0000-0002-0774-0920>

to floor structures as a building element which bears the incident loads and transfers them to the adjacent walls. Since timber floors present a significant part of the existing building stock (for example in Slovenia [1]), acquirement of existing timber floor data and strengthening measures is crucial for planning effective building renewal strategies.

Regarding the strengthening problem, timber floors can be arranged into two categories. The first category represents timber floors that have no importance for the cultural heritage and the second category represents timber floors of historical and cultural interest. The strengthening techniques for the first group are controlled only with the owners wish or solely by economic reasons, whereas limitations for the second group regard the reversibility, the compatibility, the minimum level of intervention and fulfillment of internationally accepted requirements regarding historic architecture [2].

The strengthening measures for timber floors can be split into strengthening techniques for vertical (“out of plane”) loads and horizontal (“in-plane”) loads [3]. Especially the timber-concrete composite (TCC) section has gained importance as a new structural element and as a strengthening technique in the past years [4], as it strengthens the “out of plane” and “in-plane” behavior of the timber floor simultaneously. Instead of the concrete part of the TCC section, additional timber elements in the form of cross-laminated timber are often used, which presents a dry technique for forming composite cross sections and is therefore preferred for timber floors of historical or cultural interest ([2, 3, 5, 6]). Other strengthening techniques involve the use of additional tensile or bending elements connected to the existing timber joists.

Beside increased incident loads, time imposed timber damage can be a reason for strengthening measures, although it is often an argument for replacement of the timber floor with a reinforced concrete floor. Floor vibrations are also an essential criterion for evaluating floor structures but are already positively influenced with strengthening measures for ultimate and deflection limit states which are not covered in this article.

Irrespective of the article’s subject being only load-bearing capacity, there are also other important timber floor technical criteria, such as sound insulation, fire safety and thermal conductivity. They must not be ignored when planning timber floor renovation, but they also are not considered in this study.

The first part of this article briefly presents the evolution of floor structures and timber floor types in Central Europe, although the validity of the findings for other territories is not excluded. Attention is also given to timber floor filling weights. In addition, an overview of timber floor strengthening techniques is provided. The second part of this article includes a numerical comparative case study of a classic timber floor and a timber-concrete composite floor. The research focuses especially on the acquirement of existing timber floor geometry; whereas the essential contribution of the numerical study lies in the load-bearing capacity limitations of existing timber floors and TCC floors with existing timber floor joist geometry.

2. THE EVOLUTION OF FLOOR STRUCTURES

According to [7], Central European floor structures until the 19th century can be arranged into three groups:

- Timber floors with joists without spacing (Fig. 1a)

Due to a higher load-carrying capacity, they were often used for the upper floors, because they provided a higher fire safety as they could carry the loads resulting from a demolished roof structure, possibly as a result of a fire. Due to the dense arrangement, they also provided a significant obstacle for fire propagation.

- Classic timber floor with timber joists with spacing (Fig. 1b)

They were used for floors between the ground and upper floor. There are many subtypes which only differ in the sense of different arrangements of floor paneling and filling between joists.

- Vaults (vaults, vaults between iron beams) (Fig. 1c)

Vaults were usually used on lower floors, cellars and over staircases.[7]

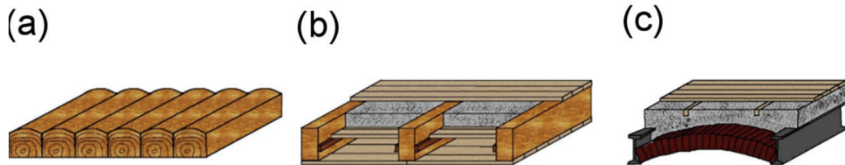


Fig. 1 - Floor structures used until the 19th century: (a) Timber floor with joists without spacing; (b) Classic timber floor with timber joists with spacing; (c) Vaults between iron beams (redrawn from:[7])

In the 20th century reinforced concrete began being used for floors more frequently. Later, many different floor types were invented, which especially lowered the material consumption and consequently diminished the floor weight (prefabricated concrete elements, masonry fillings, etc.). Afterward, the development of composite and prestressed systems followed. Parallel to the structural developments, building physics' demands have risen (sound insulation, thermal conductivity, etc.), which required floors consisting of multiple layers of materials with various properties.[7]

3. TIMBER FLOOR TYPES

In principle, there are two types of old timber floors. The first type is represented by timber floors without joist spacing (Fig. 1 a) and the second type by timber floors with joists with spacing (Fig. 1 b). A newer development is seen in the timber floor panels (Fig. 2 a), which have slender timber joists mechanically or adhesively connected to different wood-based sheeting boards. The latest type of timber floors consist of the cross-laminated timber floor elements (Fig. 2 b). Somewhat less often, glued laminated timber elements are also used for floors (Fig. 2 c). Instead of adhesives also mechanical connectors are used but to a much lesser extent.

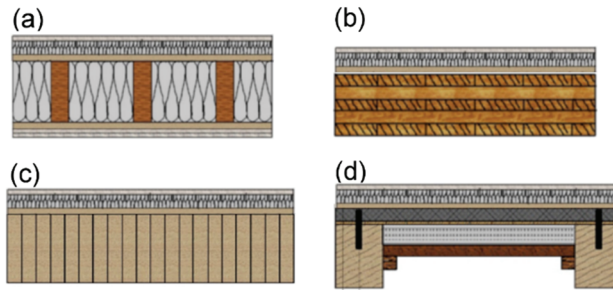


Fig. 2 - Timber floor types: (a) Timber floor panels; (b) Cross-laminated timber floor; (c) Glued laminated timber floor; (d) Timber-concrete composite floor

3.1. Timber-Concrete Composite Floors

The timber-concrete composite floor (Fig. 2 d) is a structural system, which is used for strengthening existing timber floors and for new construction projects. There are also examples of the system used in bridge construction [8]. The main advantages of the system are [7]:

- Rational use of various materials (concrete is in the compressive zone of the cross section and timber is in the tension zone of the cross section)
- Possibility of an undemanding strengthening of existing timber floors
- Relatively high bending stiffness
- Rigid diaphragm behavior
- Positive effect on the vibrational behavior of the floor
- Positive effect on the floor sound insulation properties
- Positive effect on the floor fire safety

The shear forces due to the composite action between timber and concrete are transmitted through mechanical connections. There are also attempts with adhesive layers providing the connection [9]. Different fasteners may be used for mechanical connections: bolts, nails, dowels, toothed plates. The concrete slab is usually reinforced in compliance with minimum reinforcement requirements, splitting forces resulting from mechanical connectors and rheological behavior of concrete (shrinkage) [7].

In addition, attention must also be given to the cultural heritage criteria, for example in Italy the timber-concrete approach for strengthening old timber floors was often rejected by responsible authorities due to claims that the measure is not reversible [6].




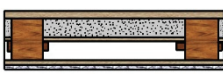



3.2. Timber Floor Filling

An important property of timber floors is the filling material inserted between timber joists. The filling material had the function of sound insulation, fire insulation and reduction of floor vibrations. According to [10] the materials used for timber floor fillings were:

- construction waste (crushed masonry, usually burnt) with a density of about 1400 kg/m³
- slag (without sulfur) with a density of about 850 kg/m³
- black coal ash with a density of about 750 kg/m³
- sand and gravel with a density of about 1400 kg/m³
- clay with a density of about 1800 kg/m³

Many variants of old timber floors with descriptions can be found in [11]. These descriptions were used to determine ratios of filling weight to floor weight. The results for each variant can be found in Table 1. The weight percentages reach from 20 % to 65 %. The filling area weight in all variants is more than 0.5 kN/m². Considering the low weight of new insulation materials, the removal of the filling may considerably influence the imposed load limit of the floor.

Table 1 - Floor weights and filling weight percentages (Figures redrawn from: [11])

Timber floor variant	Floor area weight	Filling	Filling volume per area usage	Filling area weight	Weight percentage of the filling
	$\left[\frac{\text{kN}}{\text{m}^2}\right]$	/	$\left[\frac{\text{m}^3}{\text{m}^2}\right]$	$\left[\frac{\text{kN}}{\text{m}^2}\right]$	[%]
	2.24	slug	0.075	0.64	28.5
	2.07	sand	0.040	0.56	27.1
	2.20	construction waste	0.046	0.64	29.3
	2.20	sand	0.062	0.87	39.5
	2.88	ash	0.078	0.59	20.3
	1.50	slug	0.079	0.67	44.8
	2.20	clay	0.079	1.42	64.6

3.2.1. Building Codes Related to Prescribed Imposed Loads

In Slovenia (a former Yugoslav country), an increase of the prescribed imposed loads occurred when the building standards in the former Yugoslavia have been changed and later when they were replaced with the Eurocodes, the current building standards in the European Union. The old Yugoslav building regulations from 1948, the PTP-2 (“Privremeni tehnicki propisi za opterecenje zgrada”), can be found in [12]. In 1988 the standard with prescribed imposed loads, the JUS U.C7.121, was introduced, which was identical with the standard ISO 2103:1986 [13]. After the entry of Slovenia into the European Union in 2004, the Eurocode 1 [14] had become the adopted standard for the prescribed imposed loads. Table 2 shows the prescribed imposed loads for residential areas, offices and exhibition halls from the mentioned standards. Comparing the differences between the minimum imposed loads with the floor filling weights, one can see that the increase of the minimum imposed loads (due to changing standards) can be partly alleviated or completely balanced out with the removal or replacement of the timber floor filling with a modern insulation material.

Table 2 - Prescribed minimum imposed loads from different standards

	PTP-2 [12]	JUS U.C7.121 (ISO 2103:1986 [13])	Eurocode 1 [14]
Area category	$\left[\frac{\text{kN}}{\text{m}^2}\right]$	$\left[\frac{\text{kN}}{\text{m}^2}\right]$	$\left[\frac{\text{kN}}{\text{m}^2}\right]$
Residential areas	1.25-1.5	1.5	2.0
Offices	2.0	2.0	3.0
Exhibition halls	2.0	2.5	5.0

4. MEASURES FOR STRENGTHENING OLD TIMBER FLOORS

Although old timber floors are often replaced with reinforced concrete floors, numerous measures can be used for strengthening. According to [11] some of these measures are:

- Decreasing the timber joist spacing
- Installation of additional beams under the floor for intermediate support
- Installation of additional joists under locations of concentrated loads
- Joist strengthening with nailed timber elements (Fig. 3 a)
- Forming of box girders by using the original joists, additional joists and sheeting boards (Fig. 3 b)
- Use of tension or bending elements connected to timber joists (Fig. 3 c). Materials such as steel or carbon fiber reinforced polymers are used.
- Use of tension elements and spacer posts, which enlarge the bending height of the cross-section (Fig. 3 d). It is also possible to pre-stress the timber joists with steel elements.

- Forming of a composite cross-section (Fig. 2 d). Usually, concrete elements are added to the timber joists and mechanically connected with various steel fasteners.

Instead of concrete elements also cross-laminated timber elements are known to be used for forming composite cross sections [15].

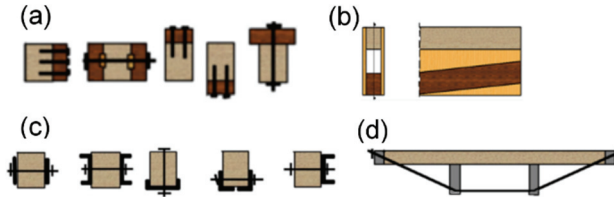


Fig. 3 - Timber floor strengthening methods: (a) Strengthening timber joists with nailed timber elements; (b) Forming of box girders; (c) Tension or bending elements connected to timber joists; (d) Enlarging the bending height with tension elements and spacer posts (redrawn from: [11])

There are also examples of forming a timber-concrete composite cross-section with an additional carbon fiber reinforced polymer strip in the tensile zone [16]. Bending tests (Fig. 4) for this measure can be found in [17].



Fig. 4 - Bending tests of timber-concrete composite sections with additional carbon strips

Another option is the usage of steel collars which surround existing timber floor joists and is presented in [18]. The forces between the steel collars and the timber joists are transmitted through friction, which is ensured due to a rubber layer which is vulcanized, in contact with the steel collar and transversal ringing action due to bolt tightening. The collars are used to connect additional elements (for example concrete slabs) to the timber joists without perforating them and without causing any strength reduction.

4.1. Timber Floor in-Plane Strengthening

Besides the vertical behavior of floor structures, their horizontal behavior is also important, because the horizontal floor stiffness affects the stability or load-bearing capacity of the whole building. It is important to determine whether the floor structure can be considered a

rigid diaphragm (Fig. 5) and if it can redistribute horizontal forces (wind or earthquake forces) to the neighboring elements – walls [19].

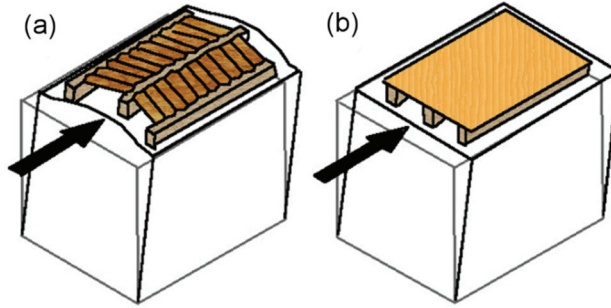


Fig. 5 - Role of the diaphragm preventing the overturning modes of masonry walls: (a) the inadequate in-plane stiffness of the floor causes overturning of the walls perpendicular to the seismic action; (b) a stiff diaphragm allows forces to be transmitted to the walls parallel to the seismic action (redrawn from:[20])

In cases where the timber floors do not behave as rigid diaphragms (or diaphragms at all), different wall collapse or overturning modes are possible (Fig. 6), as walls usually do not have sufficient strength for forces acting perpendicular to the wall plane [19].

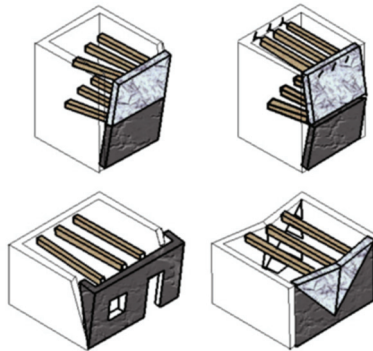


Fig. 6 - Wall overturning modes due to an inadequate stiffness of the floor (redrawn from:[20])

Although there are different ways of stiffening timber floors in the horizontal plane (Fig. 7), it turned out that some of these measures are only conditionally useful. Among them is the replacement of timber floors with reinforced concrete floors and installing reinforced concrete ties into the masonry, as the higher mass and higher stiffness can negatively impact

the building [19]. The problem is the connection of the new reinforced concrete elements with the old masonry walls. As stated in [21], for a successful use of reinforced concrete elements it is necessary to ensure monolithic behavior of the old masonry walls, which are often built as a kind of layered structures, and to prevent the wall layers to separate, which is observed in seismic experiments and during actual earthquakes.

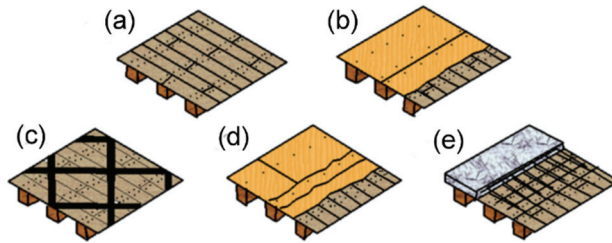


Fig. 7 - Different timber floor in-plane shear strengthening techniques: (a) existing simple layer of wood planks on the timber beams; (b) second layer of wood planks crossly arranged to the existing one and fixed by means of steel studs; (c) diagonal bracing of the existing wood planks by means of light steel plates or FRP laminae; (d) three layers of plywood panels glued on the existing wood planks; (e) a stud-connected reinforced concrete slab (redrawn from: [20])

In [20] installation of a steel curb and a reinforced concrete curb is shown as a measure of horizontal floor stiffening. Furthermore, [22, 23] discuss a timber floor on masonry walls, which were strengthened with prestressed steel ties on both sides and at the floor height, to act as a rigid diaphragm. In [24] the use of gang nails, which present a direct connection between the wooden boards, for horizontal stiffening of timber floors is investigated. In addition, [24] studied the use of carbon fiber-reinforced polymers strips for horizontal stiffening of timber floors. To sum up, there are many different timber floor strengthening techniques, but only a few of them simultaneously strengthen the timber floor “in-plane” and “out of plane” behavior. One of the few is the timber-concrete composite cross-section.

5. NUMERICAL CASE STUDY OF A TIMBER FLOOR AND A TCC FLOOR

Although timber floors can have random geometric properties, for example timber joist cross sections differing from a rectangular cross-section (Fig 8), Brezar [25] writes about the so-called 4-meter syndrome in European buildings, claiming that the most common span of European rooms is 4 meters, which is the consequence of different practical criteria such as easy transport or handleability. Brezar [25] also foresees that the dimension of a classic timber floor joist cross section should be 18 cm x 24 cm. The same timber joist dimension can be found in [10], although for a 5 m span and a timber joist spacing of 0.9 m.



Fig. 8 - Timber joists with an inverted T-cross section from a demolished timber floor

To get an insight into the load-bearing capacity of old timber floors, the following numerical case study deals with the comparison of a classic timber floor for a 5 m span and a timber-concrete composite floor (TCC floor) with regards to their imposed load-bearing capacity. The TCC floor has the same timber joist dimension as the so-called classic timber floor. The numerical case study is conducted to provide an insight into the potential of classic timber floors and strengthening methods in view of complying with the current building standards.

5.1. Timber Floor

The floor section is given in Fig. 9 and the timber joist dimensions are given in Table 3. The wooden flooring is fitted on spacer boards, which were oriented perpendicularly to the timber joists and had an axial distance of about 1 meter. The space between the spacer boards and timber joists was filled with a mixture of sand and gravel. The function of the lower wooden boards was to hold the floor filling in place.

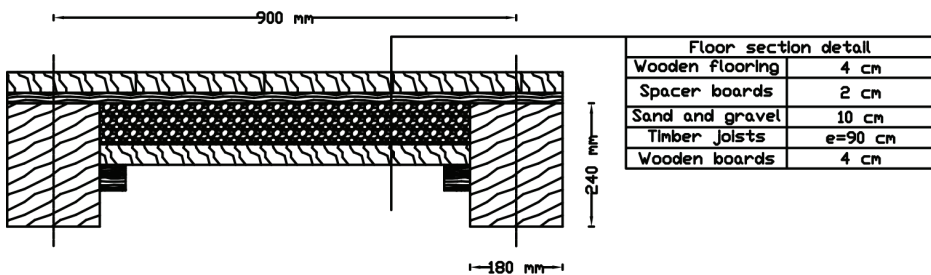


Fig. 9 - Floor section detail

Table 3 - Geometric properties of the timber floor

Timber joist width	b_t	18	[cm]
Timber joist height	h_t	24	[cm]
Span length	l	5	[m]
Joist spacing	e	90	[cm]

5.1.1. Mechanical Properties of the Timber Floor Joists

The timber class of the timber joists was defined as C24 and the serviceability class as S2. The mechanical properties are given in Table 4.

Table 4 - Mechanical properties of timber class C24

Characteristic bending strength	$f_{m,k}$	24.00	[MPa]
Characteristic tensile strength along the grain	$f_{t,0,k}$	14.00	[MPa]
Characteristic shear strength	$f_{v,k}$	2.50	[MPa]
Mean value of modulus of elasticity	E_{mean}	11.00	[GPa]
Mean value of shear modulus	G_{mean}	0.69	[GPa]
Mean density	ρ_m	420.00	$\left[\frac{kg}{m^3}\right]$

5.1.2. Structural Calculation

To assess the load-bearing capacity of the given timber floor an analysis is performed according to Eurocode 5 [26]. The combination factors for area category C3 were used. The area category C3 in Eurocode 1 [14] has a prescribed imposed load of 5 kN/m² and is defined as an area without obstacles for moving people. The input parameters for the structural calculation are given in Table 5.

Although the actual span is 5 meters, calculations of maximum imposed loads (Q) are carried out for different spans, different ultimate and serviceability limit states criteria. Deflections from shear deformations are also considered. The final deflection is calculated taking timber creep into account. The static system is a simply supported beam. The design strengths are used for strength verifications ($X_d = k_{mod} \cdot \frac{X_k}{\gamma_M}$).

Table 5 - Input parameters for the structural calculation

Floor self-weight	G	1.55	$\left[\frac{\text{kN}}{\text{m}^2}\right]$
Filling density	ρ_{fill}	1300	$\left[\frac{\text{kg}}{\text{m}^3}\right]$
Partial factor for permanent actions	γ_G	1.35	/
Partial factor for variable actions	γ_Q	1.50	/
Modification factor for duration of load and moisture content	k_{mod}	0.80	/
Crack factor for shear resistance	k_{cr}	0.67	/
Factor for quasi-permanent value of a variable action	ψ_2	0.60	/
Deformation factor	k_{def}	0.80	/
Partial factor for material properties	γ_M	1.30	/

Considered criteria in the calculation are:

- Ultimate limit state – Bending:

$$\sigma_{m,d} = \frac{M_{Ed}}{I_{t,y}} \cdot \frac{h_t}{2} \leq f_{m,d} \quad (1)$$

- Ultimate limit state – Shear

$$\tau_d = \frac{V_{Ed} \cdot S_y}{I_{t,y} \cdot b_{ef}} \leq f_{v,d} \quad (2)$$

- Serviceability limit state – Instantaneous deflection (deflection limit: span/300)

$$u_{\text{inst}} = \int_0^l \frac{M_{Ed,y0}(x) \cdot M_{Ed,y1}(x)}{E_t \cdot I_{t,y}} + \int_0^l \frac{V_{Ed,z0}(x) \cdot V_{Ed,z1}(x)}{G_t \cdot A_{t,s}} \leq \frac{l}{300} \quad (3)$$

- Serviceability limit state – Final deflection (deflection limit: span/250)

$$u_{\text{fin}} \cong \sum_{i=1}^N u_{\text{inst},i} \cdot (1 + \psi_{2,i} \cdot k_{\text{def}}) \leq \frac{l}{250} \quad (4)$$

where $\sigma_{m,d}$ is the design bending stress, M_{Ed} the design bending moment, E_t the modulus of elasticity of timber, $I_{t,y}$ the timber joist cross section moment of inertia about the y-axis, $f_{m,d}$ the design bending strength, τ_d the design shear stress, V_{Ed} the design shear force, S_y the first moment of area for the half of the timber joist cross-section, b_{ef} the effective width of the timber joist cross-section ($b_{ef} = b_t \cdot k_{cr}$), $f_{v,d}$ the design shear strength, u_{inst} the instantaneous

deflection, $M_{Ed,y0}(x)$ and $V_{Ed,z0}(x)$ the functions of the actual timber joist inner forces, $M_{Ed,y1}(x)$ and $V_{Ed,z1}(x)$ the functions of the timber joist inner forces due to virtual forces in the point and direction of the maximum deflections (middle span point and gravity direction), G_t the shear modulus of timber, $A_{t,s}$ the effective shear area of the timber joist ($A_{t,s} = \frac{A_t}{1.2}$ for rectangular cross-sections), A_t the cross-section area of the timber joist, u_{fin} the final deflection, $u_{inst,i}$ the instantaneous deflection for the individual load (permanent or variable).

The instantaneous deflection is calculated for the characteristic load combination, whereas the final deflection is calculated for the quasi-permanent load combination. The combination of actions for permanent or transient design situations is used for the ultimate limit state checks.

5.1.3. Results

The results for the calculation of maximum imposed loads for the classic timber floor are presented in Fig. 10.

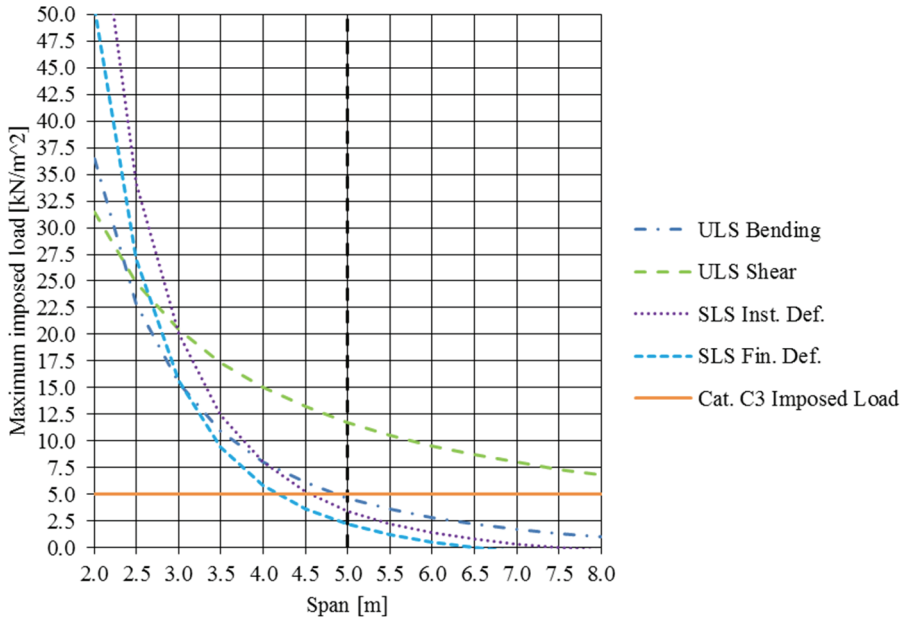


Fig. 10 - The dependence of maximum allowable imposed load on the span length – timber floor (the vertical dashed line labels the actual floor span)

Fig. 10 shows that the final deflection is the most critical criterion. The maximum allowable imposed load for our timber floor is about 2.5 kN/m² as allowed by the serviceability criteria. Considering our chosen area category (C3), the maximum calculated allowable imposed load from the serviceability criteria is too low, the ULS criteria, on the other hand, are met. Moreover, the shear strength seems to be the most uncritical criterion. If the floor is used for

category A (floors), both the ULS and SLS criteria will be met, as the characteristic value for category A the imposed load is 2.0 kN/m^2 . However, considering the high floor filling weight of about 1.0 kN/m^2 , a replacement of the filling material with a modern and light insulation material will result in considerably higher allowable (maximum) imposed loads. To conclude, it can be also seen that the SLS criteria are the most critical for spans longer than 3.0 m, for spans shorter than 3.0 m the ULS criteria are more critical.

5.2. Timber-Concrete Composite Floor

As previously presented, the timber floor does not meet the ULS and SLS criteria for area category C3. Our next analysis includes a contribution of the concrete slab to the load-bearing capacity in a composite floor element with the same timber joist properties as in the investigated timber floor (5.1. Timber Floor). The timber-concrete composite floor section (with all details) is given in Fig. 11 and, in comparison to the timber floor section, presents a modern floor which should also comply with today’s housing culture. The concrete slab segment geometric properties are given in Table 6. The mechanical connectors between the concrete slab and timber joists were steel dowels.

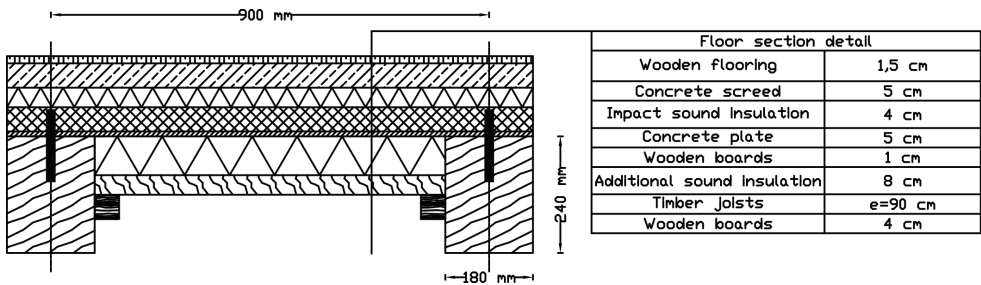


Fig. 11 - Timber-concrete composite section detail

Table 6 - Geometric properties of the concrete slab (segment)

Concrete slab segment width	$b_c(=e)$	90	[cm]
Concrete slab thickness	h_c	5	[cm]
Uncracked concrete slab thickness (initial value for all limit states)	x_c	5	[cm]
Thickness of wooden boards between the timber joist and concrete slab (for considering the gap between the timber joists and concrete slab)	t_{wb}	1	[cm]

5.2.1. Mechanical Properties of the Concrete Slab

The strength class of the concrete slab is defined as C20. The mechanical properties are given in Table 7.

Table 7 - Mechanical properties of concrete class C20

Characteristic compressive cylinder strength of concrete at 28 days	f_{ck}	20	[MPa]
Secant modulus of elasticity	E_{cm}	30	[GPa]
Mean density	$\rho_{c,m}$	2500	$\left[\frac{kg}{m^3}\right]$

5.2.2. Structural Calculation

The calculations are performed in compliance with the so-called “gamma method” from Annex B of Eurocode 5 [26]. The input parameters for the structural calculation are given in Table 8.

The connectors are only used for stiffness requirements and are not structurally checked. During construction, the floor should be fully supported consequently, the floor self-weight and imposed loads are defined as completely resisted by the composite section. The concrete tensile strength is considered to be zero; therefore concrete is understood as to fail under tension. Although minimum reinforcement should be present in the concrete slab, this is not taken into consideration in structural calculation. The uncracked concrete slab thickness is calculated iteratively (if the first step of the calculation shows tensile stresses in the concrete slab). The new thickness or uncracked section thickness, x_c , is used to recalculate the floor bending stiffness of each iteration step, although γ , the coefficient of composite action, is calculated only for the uncracked concrete thickness. The reason for this is the reflection of the global composite beam behavior through the γ coefficient. The static system is a simply supported beam.

Table 8 - Input parameters for the structural calculation

Floor self-weight	G	2.8	$\left[\frac{kN}{m^2}\right]$
Concrete creep coefficient	ϕ_c	3.0	/
Dowel diameter	d_{dow}	20	[mm]
Dowel spacing	s_{dow}	10	[cm]
Modification factor for duration of load and moisture content	k_{mod}	0.8	/
Partial factor for concrete for ultimate limit states	γ_C	1.5	/

Creep of both materials (timber and concrete) is considered in the calculation. The ULS criteria depend only on timber tensile and bending strength, as the concrete compressive strength ($\frac{f_{ck}}{\gamma_c}=13.3$ MPa) is never exceeded. Although the actual span is 5 meters, calculations of maximum imposed loads (Q) for different spans, different ultimate and serviceability limit states criteria are carried out. Deflections from shear deformations are not considered. The whole concrete slab width is considered for calculation, as the determination of the effective flange width (according to Eurocode 2 [27]), b_{eff} , shows that the calculated effective flange width is greater than the actual concrete slab segment width, b_c , for spans longer than approximately 3.4 m. The results for spans shorter than 3.4 m are therefore slightly overestimated.

The effective bending stiffness $((EI)_{ef})$ of the composite floor is defined with:

$$(EI)_{ef} = \sum_{i=1}^N (E_i \cdot I_i + \gamma_i \cdot E_i \cdot A_i \cdot a_i^2) \tag{5}$$

where E_i is the modulus of elasticity of the individual material, A_i the (uncracked) cross-section area of the individual member, a_i the distance between the centers of gravity of the individual cross-section and composite cross-section and I_i the moment of inertia of the individual cross section.

The γ coefficient for timber is equal to 1.0, the γ coefficient for the concrete slab (for the appropriate limit state) is defined with:

$$\gamma = \frac{1}{1 + \frac{(\pi^2 \cdot E_c \cdot h_c \cdot b_c \cdot s_{dow})}{K_i \cdot I^2}} \tag{6}$$

where K_i is the slip modulus for the considered limit state. The instantaneous slip modulus for serviceability limit states is defined with:

$$K_{ser} = \frac{2 \cdot \left(\frac{\rho_m}{\rho_{kg}}\right)^{1.5} \cdot \frac{d_{dow}}{mm}}{m^3} \cdot \frac{N}{mm} \tag{7}$$

The instantaneous slip modulus for ultimate limit states is defined with:

$$K_u = \frac{2}{3} \cdot K_{ser} \tag{8}$$

The final slip modulus for ultimate limit states is defined with:

$$K_{u,fin} = \frac{K_u}{1 + \frac{(k_{def} \cdot \psi_2 \cdot \phi_c)}{2}} \tag{9}$$

The final slip modulus for serviceability limit states is defined with:

$$K_{\text{ser,fin}} = \frac{K_{\text{ser}}}{1 + \frac{(k_{\text{def}} + \phi_c)}{2}} \quad (10)$$

For the instantaneous design checks the mean values of moduli of elasticity ($E_c = E_{\text{cm}}$ and $E_t = E_{\text{mean}}$) are used, whereas modified values are used for the final design checks (due to creep).

The timber final modulus of elasticity for ultimate limit states is defined with:

$$E_{t,u} = \frac{E_{\text{mean}}}{1 + k_{\text{def}} \psi_2} \quad (11)$$

The timber final modulus of elasticity for serviceability limit states is defined with:

$$E_{t,\text{ser}} = \frac{E_{\text{mean}}}{1 + k_{\text{def}}} \quad (12)$$

The concrete final modulus of elasticity for the ultimate and serviceability limit states is defined with:

$$E_c = \frac{E_{\text{cm}}}{1 + \phi_c} \quad (13)$$

The axial force (due to composite action) stress component of the individual cross section is defined with:

$$\sigma_{N,i} = \frac{\gamma_i \cdot E_i \cdot a_i \cdot M_{\text{Ed}}}{(EI)_{\text{ef}}} \quad (14)$$

The bending moment stress component of the individual cross section is defined with:

$$\sigma_{M,i} = \frac{0.5 \cdot E_i \cdot h_i \cdot M_{\text{Ed}}}{(EI)_{\text{ef}}} \quad (15)$$

where h_i is the uncracked height (in case of the concrete slab x_c).

The total normal stress of the individual cross section is defined with:

$$\sigma_i = \sigma_{N,i} + \sigma_{M,i} \quad (16)$$

In the calculation considered criteria are:

- Serviceability limit state – Instantaneous deflection (deflection limit: span/300)

The characteristic load combination is used for checking instantaneous deflection.

$$u_{\text{inst}} = \int_0^l \frac{M_{\text{Ed},y0}(x) \cdot M_{\text{Ed},y1}(x)}{(EI)_{\text{ef}}} dx \leq \frac{l}{300} \quad (17)$$

- Serviceability limit state – Final deflection (deflection limit: span/250)

The quasi-permanent load combination is used for checking the final deflection. This limit state considers creep of both materials (timber and concrete).

$$u_{fin} = \int_0^l \frac{M_{Ed,y0}(x) \cdot M_{Ed,y1}(x)}{(EI)_{ef}} \leq \frac{1}{250} \tag{18}$$

- Ultimate limit state – Bending Instantaneous

$$\frac{\sigma_{N,t}}{f_{t,0,d}} + \frac{\sigma_{M,t}}{f_{m,d}} \leq 1 \tag{19}$$

- Ultimate limit state – Bending Final

This limit state considers creep of both materials (timber and concrete). The equation (19) is applied with appropriate input parameters.

- Ultimate limit state – Shear

Only the shear capacity of the timber joists is used, which means that the results for the maximum imposed load from the ULS – Shear criterion are conservative. The equation (2) is applied.

5.2.3. Results

The results for the calculation of maximum imposed loads for the timber-concrete composite floor are given in Fig. 12.

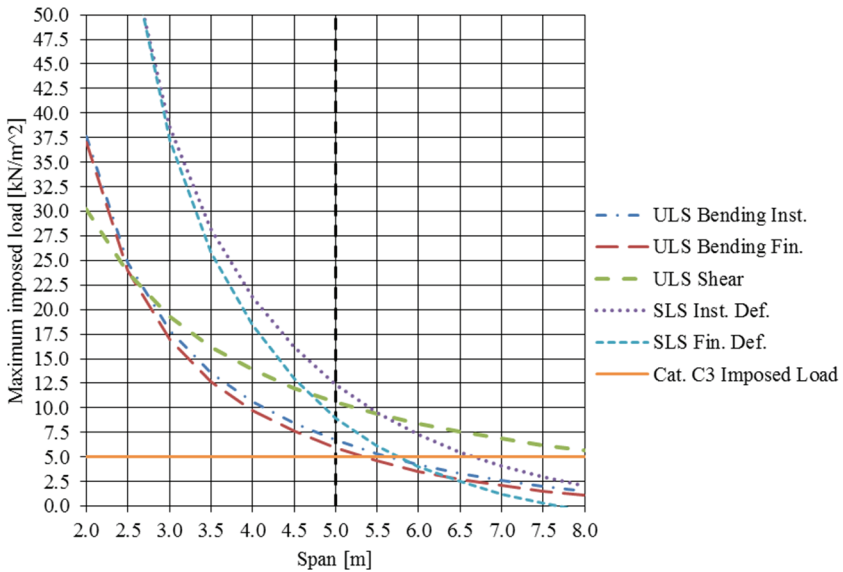


Fig. 12 - Dependence of the maximum allowable imposed load on the span length – timber-concrete composite floor (the vertical dashed line labels the actual floor span)

It can be seen from Fig. 12 that the most critical criterion for the composite floor of 5 m span is the ULS Bending criteria. The maximum allowable imposed load regarding the SLS – Fin. Def. criterion for the timber-concrete composite floor is about 9.0 kN/m², whereas for the ULS – Bending Final criterion the maximum allowable imposed load is about 5.9 kN/m².

The ULS – Bending criteria are the decisive criteria for spans shorter than 6.5 m, for longer spans the SLS Fin. Def. maximum imposed load is the decisive criterion. The ULS – Shear criterion is mostly uncritical, even after the shear load is (computationally) completely resisted by the timber joists.

According to our chosen category of use and span length, the calculated maximum allowable imposed loads from the serviceability and ultimate criteria are high enough for the category C3.

Detailed results for each criterion and span length ($\sigma_{c,top}$ is the concrete slab top stress and $\sigma_{c,bot}$ is the uncracked concrete slab bottom stress):

- Ultimate limit state – Bending Instantaneous (results are given in Table 9)

Table 9 - Results for »Ultimate limit state – Bending Instantaneous«

l	Q	$\sigma_{c,top}$	$\sigma_{c,bot}$	x_c	$(EI)_{ef}$	K	γ
[m]	$\left[\frac{kN}{m^2}\right]$	[MPa]	[MPa]	[cm]	$[GN \cdot cm^2]$	$\left[\frac{kN}{cm}\right]$	/
2.0	37.60	-3.23	0.00	1.00	25.20	99.80	0.03
2.5	24.75	-4.58	0.00	1.49	28.04	99.80	0.04
3.0	17.85	-5.78	0.00	2.00	32.20	99.80	0.06
3.5	13.59	-6.71	0.00	2.51	37.44	99.80	0.08
4.0	10.63	-7.36	0.00	2.99	43.32	99.80	0.11
4.5	8.43	-7.78	0.00	3.42	49.39	99.80	0.13
5.0	6.72	-8.04	0.00	3.79	55.29	99.80	0.16
5.5	5.36	-8.19	0.00	4.11	60.80	99.80	0.18
6.0	4.26	-8.27	0.00	4.39	65.81	99.80	0.21
6.5	3.36	-8.31	0.00	4.62	70.30	99.80	0.24
7.0	2.63	-8.33	0.00	4.82	74.28	99.80	0.27
7.5	2.01	-8.33	0.00	4.99	77.78	99.80	0.30
8.0	1.49	-8.33	-0.19	5.00	80.34	99.80	0.32

- Ultimate limit state – Bending Final (results are given in Table 10)

Table 10 - Results for »Ultimate limit state – Bending Final«

l	Q	$\sigma_{c,top}$	$\sigma_{c,bot}$	x_c	$(EI)_{ef}$	K	γ
[m]	$\left[\frac{kN}{m^2}\right]$	[MPa]	[MPa]	[cm]	$[GN \cdot cm^2]$	$\left[\frac{kN}{cm}\right]$	/
2.0	37.02	-1.72	0.00	1.43	16.62	36.42	0.04
2.5	23.96	-2.45	0.00	2.11	18.01	36.42	0.06
3.0	16.93	-3.13	0.00	2.82	20.00	36.42	0.09
3.5	12.63	-3.69	0.00	3.53	22.48	36.42	0.12
4.0	9.71	-4.12	0.00	4.19	25.24	36.42	0.15
4.5	7.59	-4.42	0.00	4.79	28.09	36.42	0.18
5.0	5.91	-4.60	-0.19	5.00	30.32	36.42	0.21
5.5	4.59	-4.73	-0.47	5.00	32.09	36.42	0.25
6.0	3.57	-4.84	-0.72	5.00	33.77	36.42	0.28
6.5	2.75	-4.94	-0.94	5.00	35.35	36.42	0.32
7.0	2.08	-5.03	-1.13	5.00	36.81	36.42	0.35
7.5	1.53	-5.11	-1.30	5.00	38.17	36.42	0.38
8.0	1.08	-5.18	-1.45	5.00	39.41	36.42	0.41

- Ultimate limit state – Shear (results are given in Table 11)

Table 11 - Results for »Ultimate limit state – Shear«

l	[m]	2.0	2.5	3.0	3.5	4.0	4.5	5.0	5.5	6.0	6.5	7.0	7.5	8.0
Q	$\left[\frac{kN}{m^2}\right]$	30.28	23.71	19.34	16.21	13.87	12.04	10.58	9.39	8.40	7.56	6.83	6.21	5.66

- Serviceability limit state – Instantaneous deflection (deflection limit: span/300) (results are given in Table 12)

Table 12 - Results for »Serviceability limit state – Instantaneous deflection«

l	Q	$\sigma_{c,top}$	$\sigma_{c,bot}$	x_c	$(EI)_{ef}$	K	γ
[m]	$\left[\frac{kN}{m^2}\right]$	[MPa]	[MPa]	[cm]	$[GN \cdot cm^2]$	$\left[\frac{kN}{cm}\right]$	/
2.0	95.62	-6.89	0.00	1.44	27.69	149.69	0.04
2.5	56.88	-7.94	0.00	2.07	32.80	149.69	0.07
3.0	38.72	-8.59	0.00	2.68	39.44	149.69	0.09
3.5	28.22	-8.89	0.00	3.24	46.80	149.69	0.12
4.0	21.23	-8.93	0.00	3.72	54.12	149.69	0.15
4.5	16.19	-8.79	0.00	4.12	60.92	149.69	0.19
5.0	12.41	-8.54	0.00	4.45	66.97	149.69	0.22
5.5	9.52	-8.24	0.00	4.72	72.24	149.69	0.25
6.0	7.28	-7.91	0.00	4.94	76.77	149.69	0.29
6.5	5.48	-7.54	-0.16	5.00	80.15	149.69	0.32
7.0	4.05	-7.19	-0.33	5.00	82.95	149.69	0.36
7.5	2.93	-6.86	-0.46	5.00	85.43	149.69	0.39
8.0	2.04	-6.56	-0.56	5.00	87.62	149.69	0.42

The results for bending and deflection limits states (Table 9, Table 10, Table 12 and Table 13) show that creep has a negative impact on the load-bearing capacity and it also affects the distribution of stresses. Although the concrete slab compressive stresses are averagely higher before creep, the concrete slab is more likely to be uncracked after creep (for longer spans). It is also noticed that the coefficient of composite behavior, γ , is higher after creep. A deeper look into this fact reveals that timber creep decreases the γ coefficient, concrete creep, on the other hand, increases the γ coefficient. As the chosen value for the concrete creep coefficient, ϕ_c , was higher than the timber creep (k_{def} for serviceability limit state or $k_{def} \cdot \psi_2$ for the ultimate limit state), this results in a higher γ coefficient. Moreover, if the creep values for concrete and timber are equal, the creep will have no effect on the γ coefficient. Furthermore, observations reveal that the maximum imposed loads for the serviceability limit state after creep (Table 13) for spans shorter than 3 m are higher than the maximum imposed loads for the serviceability limit state before creep (Table 12). This is also a consequence of the γ coefficients being higher after creep and of the fact that the percentage difference between the γ coefficients (between the before and after creep values) is higher for shorter spans.

The concrete stresses are for all limit states considerably lower than the design concrete compressive strength ($\frac{f_{ck}}{\gamma_c}=13.3$ MPa), which insinuates that using a higher concrete strength class would not give better results (higher maximum imposed loads) considering the rather small differences in the moduli of elasticity for different concrete strength classes.

- Serviceability limit state – Final deflection (deflection limit: span/250) (results are given in Table 13)

Table 13 - Results for »Serviceability limit state – Final deflection«

l	Q	$\sigma_{c,top}$	$\sigma_{c,bot}$	x_c	$(EI)_{ef}$	K	γ
[m]	$\left[\frac{kN}{m^2}\right]$	[MPa]	[MPa]	[cm]	$[GN \cdot cm^2]$	$\left[\frac{kN}{cm}\right]$	/
2.0	100.96	-2.78	0.00	1.93	14.86	51.62	0.06
2.5	57.44	-3.18	0.00	2.76	17.07	51.62	0.09
3.0	37.23	-3.43	0.00	3.57	19.90	51.62	0.12
3.5	25.83	-3.54	0.00	4.30	23.02	51.62	0.16
4.0	18.50	-3.55	0.00	4.93	26.11	51.62	0.20
4.5	12.90	-3.42	-0.22	5.00	28.21	51.62	0.24
5.0	8.97	-3.28	-0.40	5.00	30.06	51.62	0.28
5.5	6.15	-3.15	-0.53	5.00	31.75	51.62	0.32
6.0	4.06	-3.03	-0.63	5.00	33.29	51.62	0.36
6.5	2.47	-2.91	-0.70	5.00	34.68	51.62	0.40
7.0	1.25	-2.80	-0.75	5.00	35.93	51.62	0.43
7.5	0.28	-2.70	-0.78	5.00	37.05	51.62	0.47
8.0	-0.48	-2.60	-0.80	5.00	38.05	51.62	0.50

5.2.4. Impact of Concrete Slab Thickness on the Maximum Imposed Load

In addition to the span length, the concrete slab thickness is also varied. The results for the maximum imposed load regarding the »Ultimate limit state – Bending Final« criterion can be seen in Fig. 13. The criterion is chosen because it is the most critical criterion in the previously presented example.

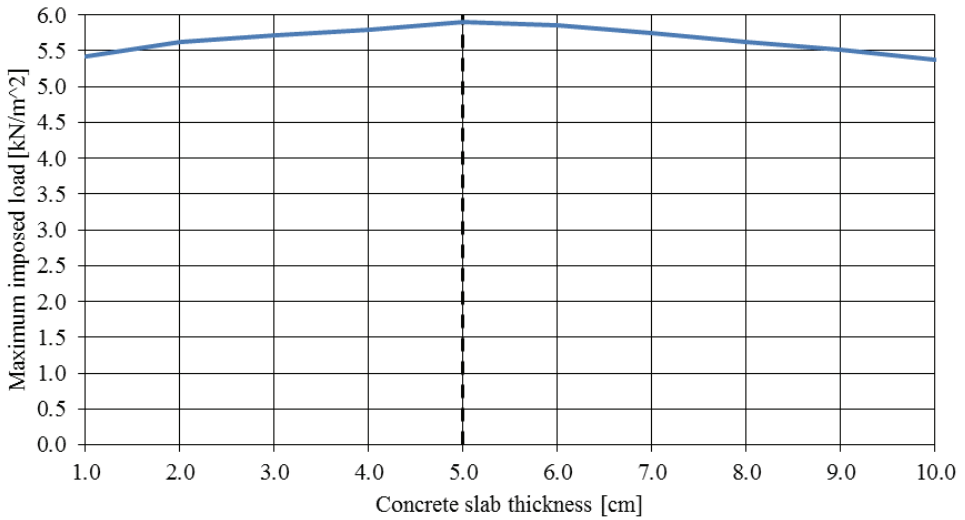


Fig. 13 - Dependence of the timber-concrete composite floor maximum allowable imposed load on the concrete slab thickness – »Ultimate limit state – Bending Final« criterion (the dashed line labels the chosen concrete slab thickness)

The results clearly show that increasing the concrete slab thickness does not result in a higher load-bearing capacity (maximum imposed load) of the TCC floor. The load-bearing capacity of the composite floor is limited by the timber strength, as the concrete compressive strength ($f_{ck} = 13.3 \text{ MPa}$) is not even nearly exceeded. This is a consequence of the concrete slab only strengthening the compressive zone of the composite section. Detailed results can be extracted from Table 14.

Table 14 shows that increasing the concrete slab thickness decreases the concrete slab compressive stresses. Furthermore, it can be seen that the highest imposed load is achieved with the concrete slab thickness of 5 cm, for which the whole concrete slab thickness is still under compression. With higher concrete slab thicknesses there is no increase in the load-bearing capacity anymore. The effective bending stiffness stagnates and starts to decrease with thicknesses higher than 5 cm because the concrete is defined to fail under tension. The coefficient of composite action, γ , is calculated only for the uncracked concrete slab thickness and decreases with higher concrete slab thicknesses. With increasing concrete slab thickness, the design bending moment is counterbalanced with inner bending moments rather than inner forces of the partial cross sections (timber joist cross-section and concrete slab cross-section). The increasing inner bending moments in the concrete slab results in concrete slab tensile cracking as concrete is considered to fail under tension. Another reason for the higher concrete slab thicknesses not resulting in higher maximum imposed loads is also the increasing self-weight of the floor.

Table 14 - Results for »Ultimate limit state - Bending Final« and varying concrete slab thickness

h_c	Q	$\sigma_{c,top}$	$\sigma_{c,bot}$	x_c	$(EI)_{ef}$	K	γ	G
[cm]	$\left[\frac{kN}{m^2}\right]$	[MPa]	[MPa]	[cm]	$[GN \cdot cm^2]$	$\left[\frac{kN}{cm^2}\right]$	/	$\left[\frac{kg}{m^2}\right]$
1.0	5.42	-7.66	-6.63	1.00	21.75	36.42	0.58	182.66
2.0	5.62	-5.63	-3.71	2.00	24.63	36.42	0.41	207.66
3.0	5.72	-4.90	-2.12	3.00	26.69	36.42	0.31	232.66
4.0	5.80	-4.64	-1.03	4.00	28.51	36.42	0.25	257.66
5.0	5.91	-4.60	-0.19	5.00	30.32	36.42	0.21	282.66
6.0	5.86	-4.55	0.00	5.09	30.56	36.42	0.19	307.66
7.0	5.75	-4.48	0.00	4.91	30.33	36.42	0.16	332.66
8.0	5.63	-4.40	0.00	4.75	30.17	36.42	0.15	357.66
9.0	5.51	-4.34	0.00	4.61	30.06	36.42	0.13	382.66
10.0	5.38	-4.28	0.00	4.48	30.00	36.42	0.12	407.66

5.3. Comparison of the Classic Timber Floor and the Timber-Concrete Composite Floor

For easier comparison, we took the lowest maximum imposed loads of both floors (5.1. Timber Floor and 5.2. Timber-Concrete Composite Floor) and compared them in one diagram (Fig. 14).

The difference between the lowest maximum imposed loads of the two floors is higher for greater spans. The TCC floor proved its structural superiority compared to the timber floor, as its lowest maximum imposed load (load-bearing capacity) is higher for almost all spans. For the 2 m span, the timber floor has a higher load-bearing capacity, but this is a consequence of the fact that only the timber joists are used for the shear resistance of the TCC floor. If the concrete slab was also considered for the shear resistance, the results for the 2 m span would also be in favor of the TCC floor.

For the 5 m span the difference between the lowest maximum imposed loads is $\left(5.9 \frac{kN}{m^2} - 2.2 \frac{kN}{m^2}\right) = 3.7 \frac{kN}{m^2}$. Even if the floor filling of the timber floor (with an area weight of $1.0 \frac{kN}{m^2}$) was removed, the difference would still be $2.7 \frac{kN}{m^2}$. Interestingly, the most critical criteria for the timber floor are the serviceability criteria and on the other hand, ultimate criteria are most critical for the TCC floor. This is probably the consequence of the concrete slab contributing to the effective bending stiffness more than to the bending strength.

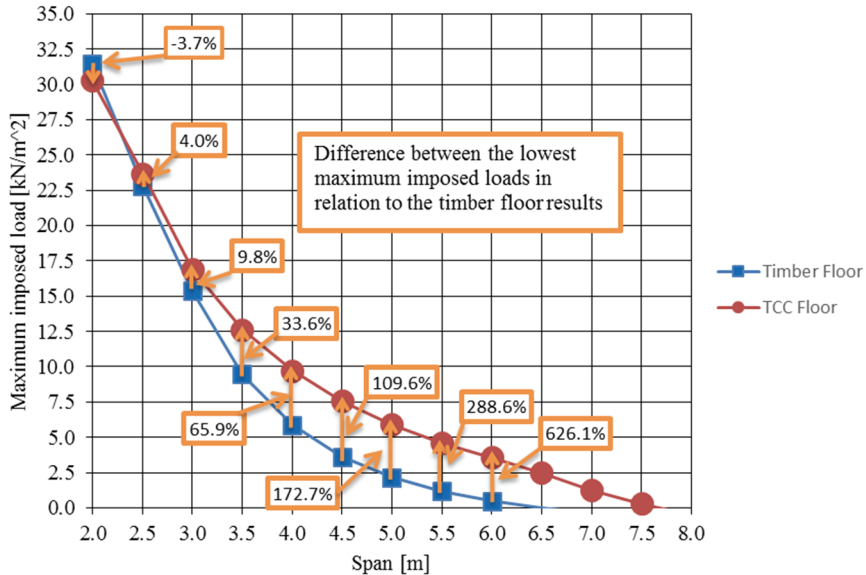


Fig. 14 - Comparison of the lowest maximum imposed load for the timber and TCC floor (the basis for the percent changes is the load-bearing capacity of the timber floor)

6. CONCLUSION

Firstly, floor structure evolution and timber floor types in Central Europe were briefly presented. The study showed that the timber floor filling presents a large part of the whole floor weight, which can be of high importance when reconstructing old timber floors. Moreover, the example from Slovenia explains how changes of building standards can cause that a floor is not in compliance with the valid building standards anymore. Although the filling removal may considerably lower the floor self-weight, the influence on other criteria should not be forgotten or disregarded. Especially the impact on the sound insulation should be controlled in the case of filling removal.

Further, timber floor strengthening techniques were presented, leading to the conclusion that numerous techniques differ only in the “strengthening target”. They can strengthen the timber joists’ compressive or tensile zone, moreover, they can also act as additional bending elements. Since it rarely happens (as in the case of apartment buildings) that the timber floor covers more rooms of one owner, the strengthening techniques should also be arranged regarding the preferable or required access side for the measure to be executed.

Despite many variants of old timber floors, the studied timber floor was declared as a classic timber floor and presented the basis of the numerical example, which showed that the load-bearing capacity of timber floors is usually limited with their serviceability criteria.

Thus, the standard timber floor, refurbished with a concrete slab, resulted in a timber-concrete composite floor and could meet the current building standard requirements. The calculations for the composite section showed the limitation of the load-bearing capacity (considering the

ultimate bending criteria) with the timber tensile and bending strength. In addition, a calculation of the load-bearing capacity (considering the final ultimate bending criteria) for different concrete slab thicknesses was performed. It showed that a higher concrete slab thickness did not necessarily result in a higher load-bearing capacity. To increase the load bearing capacity further, strengthening of the timber joist tensile zone (or side) is needed. An example of this measure is the use of CFRP strips [28]. However, as CFRP strips negatively impact the timber floor appearance, more “transparent” strengthening techniques are favorable.

The findings of this article should encourage responsible authorities to preserve the originality of old timber floors or to re-build old timber floors in a modified way, similar to the timber-concrete composite section. Furthermore, other technical criteria, such as sound insulation, fire safety and thermal conductivity should be taken into account when planning timber floor renovation. Considering the results regarding structural calculation for the timber-concrete composite floor and the literature review it seems that this floor system has the potential to fulfill all relevant criteria.

Conflict of Interest

The authors declare that they have no conflict of interest.

Acknowledgment:

The authors acknowledge the financial support from the Slovenian Research Agency (research core funding No. P2-0129).

References

- [1] Arnuga I (2010) Mehanska odpornost lesno-betonskega sovprežnega stropu [Mechanical resistance of a timber-concrete composite deck]. Univerza v Mariboru, Fakulteta za gradbeništvo
- [2] Riggio M, Tomasi R, Piazza M (2014) Refurbishment of a traditional timber floor with a reversible technique: Importance of the investigation campaign for design and control of the intervention. *International Journal of Architectural Heritage* 8:74–93
- [3] Gubana A (2015) State-of-the-Art Report on high reversible timber to timber strengthening interventions on wooden floors. *Construction and Building Materials* 97:25–33
- [4] Yeoh D, Fragiaco M, De Franceschi M, Heng Boon K (2010) State of the art on timber-concrete composite structures: Literature review. *Journal of structural engineering* 137:1085–1095
- [5] Soriano FM, Pericot NG, Sierra EM (2016) Comparative analysis of the reinforcement of a traditional wood floor in collective housing. In depth development with cross laminated timber and concrete. *Case Studies in Construction Materials* 4:125–145

- [6] Branco JM, Descamps T, Tsakanika E (2018) Repair and Strengthening of Traditional Timber Roof and Floor Structures. In: Strengthening and Retrofitting of Existing Structures. Springer, pp 113–138
- [7] Pech A, Kolbitsch A, Zach F (2007) Decken. Springer Science & Business
- [8] Graf IJ Integrale Holz-Beton-Verbundbrücken für die Landesgartenschau 2014 in Schwäbisch Gmünd
- [9] Brunner M, Romer M, Schnüriger M (2007) Timber-concrete-composite with an adhesive connector (wet on wet process). *Materials and structures* 40:119–126
- [10] Kolbitsch A (1989) Altbaukonstruktionen: Charakteristika Rechenwerte Sanierungsansätze. Springer Vienna
- [11] Lißner K, Rug W (2013) Holzbausanierung: Grundlagen und Praxis der sicheren Ausführung. Springer-Verlag
- [12] Furundžić B (1965) Zbirka tehničkih propisa u građevinarstvu [Collection of technical regulations in civil engineering]. Građevinska Knjiga, Beograd
- [13] International Organization for Standardization (1986) ISO 2103:1986 – Loads due to use and occupancy in residential and public buildings
- [14] European Committee for Standardization. (2002) EN 1991-1-1: Eurocode 1: Actions on structures - Part 1-1: General actions - Densities, self-weight, imposed loads for buildings. CEN, Brussels
- [15] Branco JM, Kekeliak M, Lourenço PB (2014) In-plane stiffness of traditional timber floors strengthened with CLT. In: *Materials and Joints in Timber Structures*. Springer, pp 725–737
- [16] Tajnik M, Premrov M, Dobrila P, Bedenik B (2011) Parametric study of composite T-beam. *Proceedings of the Institution of Civil Engineers-Structures and Buildings* 164:345–353
- [17] Premrov M, Dobrila P (2012) Experimental analysis of timber–concrete composite beam strengthened with carbon fibres. *Construction and Building Materials* 37:499–506
- [18] Faggiano B, Marzo A, Formisano A, Mazzolani FM (2009) Innovative steel connections for the retrofit of timber floors in ancient buildings: a numerical investigation. *Computers & Structures* 87:1–13. <https://doi.org/10/d5xs3b>
- [19] Costa A, Guedes JM, Varum H (2013) Structural rehabilitation of old buildings. Springer
- [20] Piazza M, Baldessari C, Tomasi R, Acler E (2008) Behaviour of refurbished timber floors characterized by different in-plane stiffness. *Structural Analysis of Historic Construction – D’Ayala & Fodde (eds)*
- [21] Tomazevic M (2009) Stavbe kulturne dediscine in potresna odpornost: kaj smo se naučili? = Heritage masonry buildings and seismic resistance: what did we learn? *Gradbeni vestnik* 2009

- [22] Tomaževič M, Weiss P, Velechovsky T (1991) the influence of rigidity of floors on the seismic behaviour of old stone-masonry buildings
- [23] Tomaževič M, Lutman M, Velechovsky T (1993) Aseismic strengthening of old stone-masonry buildings: is the replacement of wooden floors with RC slabs always necessary?
- [24] Gattesco N, Macorini L (2014) In-plane stiffening techniques with nail plates or CFRP strips for timber floors in historical masonry buildings. *Construction and Building Materials* 58:64–76
- [25] Brezar V (2011) Pragmatično graditeljstvo ali sindrom 4 metrov/Pragmatic construction or a 4-meter syndrome. *Arhitektura, Raziskave* 2011:85
- [26] European Committee for Standardization. (2004) EN 1995-1-1: Eurocode 5: Design of timber structures - Part 1-1: General - Common rules and rules for buildings. CEN, Brussels
- [27] European Committee for Standardization. (2004) EN 1992-1-1: Eurocode 2: Design of concrete structures - Part 1-1: General rules and rules for buildings
- [28] Tajnik M, Dobrila P, Premrov M (2007) Analysis of composite T beam composed of timber, concrete and carbon strip. In: *Proceedings of the 9th WSEAS international conference on Mathematical and computational methods in science and engineering*. World Scientific and Engineering Academy and Society (WSEAS), pp 223–229

Rotary Inertia and Higher Modes Effect on the Dynamic Response of Timoshenko Beams on Two-Parameter Elastic Foundation

Çağlayan HIZAL¹

Hikmet Hüseyin ÇATAL²

ABSTRACT

This study investigates the effects of rotary inertia and higher modes on the dynamic response of the axially loaded Timoshenko beams on two-parameter foundation with generalized elastic end conditions. A simplified modal analysis procedure is presented by using the conventional separation of variables method. The effect of rotary inertia on the solution of free vibration differential equation is discussed. A numerical example is presented to investigate the coupled effect of rotary inertia and higher modes on the bending moment and shear force responses.

Keywords: Rotary inertia, higher modes effect, separation of variables method, two parameter-foundation.

1. INTRODUCTION

The dynamic behavior of axially loaded beams on elastic foundation has gained the attention of many researchers. The Winkler type foundation, which is the best known of the elastic soil models, has been widely used for the estimation of soil-structure interaction. A great number of studies exist in the literature regarding the dynamic response of Euler or Timoshenko beams on Winkler type foundations [1-2]. Çatal [3, 4] obtained the fourth order differential equations by using the separation of variables method for the beams partially resting on Winkler foundation with the axial force and rotary inertia effects. A particular case, in which the free vibration equation of motion has five different solutions depending on the subgrade modulus was highlighted. Yeşilce and Çatal [5] investigated the free vibration of the Timoshenko beams on Winkler foundation with different subgrade reactions. Differential transform method (DTM) was adopted by Çatal [6] to the free vibration equations of the

Note:

- This paper has been received on March 23, 2018 and accepted for publication by the Editorial Board on November 12, 2018.
- Discussions on this paper will be accepted by September 30, 2019.

• <https://dx.doi.org/10.18400/tekderg.408772>

1 Izmir Institute of Technology, Dep. of Civil Engineering, İzmir, Turkey - caglayanhizal@iyte.edu.tr - <https://orcid.org/0000-0002-9783-6511>

2 Dokuz Eylül University, Department of Civil Engineering, İzmir, Turkey - huseyin.catal@deu.edu.tr

Timoshenko beams resting on Winkler type foundation and verified by the analytical results. Yeşilce et al. used the DTM for the free vibration analysis of axially loaded Reddy-Bickford beams [7-8]. Sapountzakis and Kampitsis [9] investigated the nonlinear behavior of the beams partially supported by tensionless Winkler foundation. Çatal [10] obtained the displacement response of forced Euler-Bernoulli beams on Winkler foundation by using the DTM. Öztürk and Coskun [11] obtained the analytical solution for the free vibration of beams on Winkler foundation with different support conditions.

In the Winkler model, the elastic soil is represented by independent linear springs within an infinitesimal part of the beam. More realistic approaches such as the two-parameter elastic foundation approach was proposed by Pasternak [12], and Vlasov and Leont'ev [13], respectively. These type of foundation models suppose that an interaction is constituted between Winkler springs by the transverse displacement [12-13]. This interaction is defined by a second parameter which represents the shear coefficient of an incompressible shear layer on the soil surface. In Pasternak model, the influence of the soil to both sides of the foundation beam is ignored as opposed to the Vlasov Model. Despite this difference, the second parameter can be taken equal for both models by considering the soil layer as a semi-infinite elastic medium [14]. Various researchers studied the behavior of the beams on two parameter foundations. Yokoyama [15] obtained the stiffness and mass matrices for the free vibration of Timoshenko beam-columns on two-parameter foundation with the effect of rotary inertia. Arboleda-Monsalve et al. [16] analyzed axially Timoshenko beam-columns with generalized end conditions on two parameter elastic foundation with rotary inertia by using the dynamic stiffness approach. Balkaya et al. [17] analyzed the dynamic response of the beams on Winkler and Pasternak foundation by using DTM. Celep et al. [18] calculated the response of a completely free beam on a tensionless Pasternak foundation subjected to dynamic loading. Malekzadeh and Karami [19] analyzed the free vibration of thick beams on two-parameter elastic foundations by using the differential quadrature and finite element method. Morfidis [20] obtained the exact finite element formulation for the dynamic analysis of beams on two and three-parameter foundations. Calio and Greco [21] investigated the exact free vibrations of Timoshenko beams and compared their results by Yokoyama [15]. Hassan and Nassar [22] obtained the dynamic displacement response of the axially loaded Timoshenko beams on two-parameter foundation.

Most previous studies investigate the dynamic response considering a few modes (commonly 3 or 5 modes). The effect of higher modes on the vibration is generally omitted. Although, the contribution of first 3-5 modes generally yield the exact results for displacement response, the bending moment and shear force response might be affected ultimately by the higher modes. Hızal and Çatal [23] mentioned that case and gave a small illustrative example. However, their study focused on the comparison of dynamic response of the Euler and Timoshenko beams on modified Vlasov foundation. In addition to the mentioned problems, the solution of the differential equation of free vibration might be affected by the rotary inertia in higher modes. For this reason, the required number of modes should be investigated considering the coupled effect of rotary inertia and higher modes.

In this study, a general solution for the dynamic behavior of axially loaded Timoshenko beams on two-parameter foundation with generalized end condition is presented. To the knowledge of the authors, the effect of higher modes on the dynamic response incorporated with the rotary inertia effect is not investigated in the literature. Different from the previous

researches, a comprehensive study is presented to show the coupled effect of higher modes and rotary inertia on the dynamic response. The effect of the rotary inertia on the solution procedure is discussed. Modal variations in the bending moment and shear force responses of Euler and Timoshenko beams with respect to the foundation type, axial force and rotary inertia are presented.

2. GOVERNING EQUATIONS

In Fig. (1), the free body diagram of an infinitesimal part of an axially loaded Timoshenko beam element is presented. Here, the transverse force and moment equilibrium of the given infinitesimal part can be written as below according to the non-dimensional coordinate, $z=x/L$.

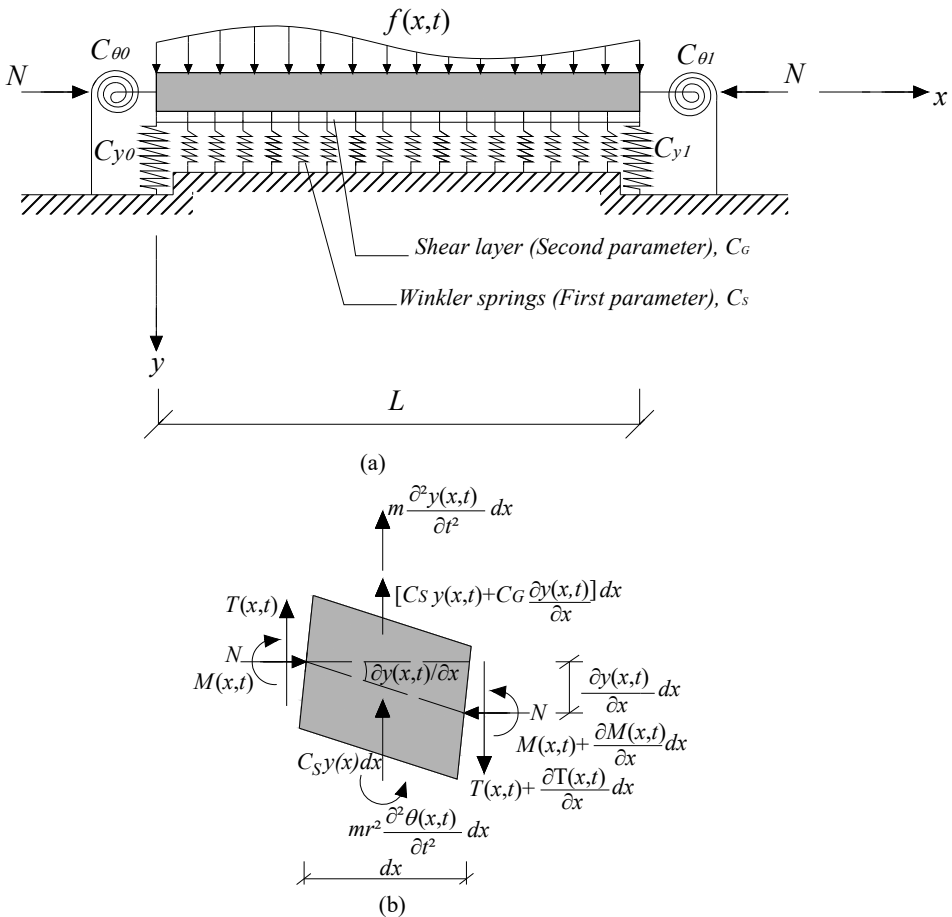


Figure 1 - (a) Timoshenko beam resting on two-parameter elastic foundation (b) Free body-diagram of infinitesimal element obtained from the beam

$$\frac{1}{L} \frac{\partial T(z,t)}{\partial z} = m \frac{\partial^2 y(z,t)}{\partial t^2} + C_s y(z,t) - C_G \frac{1}{L^2} \frac{\partial^2 y(z,t)}{\partial x^2} - f(z,t) \tag{1}$$

$$\frac{1}{L} \frac{\partial M(z,t)}{\partial z} = \frac{1}{L} N \frac{\partial y(z,t)}{\partial z} - mr^2 \frac{\partial^2 \theta(z,t)}{\partial t^2} + T(z,t) \tag{2}$$

In the equations above, $y(z,t)$, $\theta(z,t)$, $M(z,t)$, $T(z,t)$, and $f(z,t)$ denote the transverse displacement, angle of rotation, bending moment and shear force functions, and the dynamic external load, respectively. Further, N , m , r and L are the axial compressive load, distributed mass, radius of gyration and length of the beam element. In addition, the coefficients of C_s and C_G represent the elastic spring coefficients of the soil. According to the Timoshenko beam theory, with the effect of axial deformation, the first and fourth order derivatives of transverse displacement with respect to z are written as below [16];

$$\left(1 - \frac{N}{\kappa AG}\right) \frac{1}{L} \frac{\partial y(z,t)}{\partial z} = \theta(z,t) + \frac{T(z,t)}{\kappa AG} \tag{3}$$

$$\left(1 - \frac{N}{\kappa AG}\right) \frac{1}{L^4} \frac{\partial^4 y(z,t)}{\partial z^4} = -\frac{1}{L^2} \frac{1}{EI} \frac{\partial^2 M(z,t)}{\partial z^2} + \frac{1}{L^3} \frac{1}{\kappa AG} \frac{\partial^3 T(z,t)}{\partial z^3} \tag{4}$$

where E , I , G , κ and A denote the modulus of elasticity, second moment of inertia, shear modulus of the beam material, shear correction factor and area of the beam cross section, respectively. In addition, EI and κAG denote the bending and shear rigidity of the beam cross section. Substituting Eq. (3) into Eq. (2) and taking the first order derivative with respect to z leads to

$$\frac{1}{L^2} \frac{\partial^2 M(z,t)}{\partial z^2} = \frac{\partial T(z,t)}{\partial z} + \frac{1}{L^2} N \frac{\partial^2 y(z,t)}{\partial z^2} - mr^2 \left(\left[1 - \frac{N}{\kappa AG}\right] \frac{1}{L^2} \frac{\partial^4 y(z,t)}{\partial t^2 \partial z^2} - \frac{1}{\kappa AG} \frac{\partial^3 T(z,t)}{\partial t^2 \partial z} \right) \tag{5}$$

Substituting Eq. (5) into Eq. (4) gives

$$\left[\left[1 - \frac{N}{\kappa AG}\right] \frac{\partial^4 y(z,t)}{\partial z^4} + \frac{L^2}{EI} \left[\frac{\partial T(z,t)}{\partial z} + \frac{1}{L^2} N \frac{\partial^2 y(z,t)}{\partial z^2} - mr^2 \left(\left[1 - \frac{N}{\kappa AG}\right] \frac{1}{L^2} \frac{\partial^4 y(z,t)}{\partial t^2 \partial z^2} - \frac{1}{\kappa AG} \frac{\partial^3 T(z,t)}{\partial t^2 \partial z} \right) \right] - \frac{L}{\kappa AG} \frac{\partial^3 T(z,t)}{\partial z^3} \right] = 0 \tag{6}$$

Finally, the equation of motion can be written as below by substituting Eq. (1) into (6),

$$\begin{aligned}
 & \left[1 - \frac{N}{\kappa AG} \right] \frac{\partial^4 y(z,t)}{\partial z^4} + \frac{1}{EI} \left[mL^2 \frac{\partial^2 y(z,t)}{\partial t^2} + C_s L^2 y(z,t) - C_G \frac{\partial^2 y(z,t)}{\partial z^2} - mr^2 \left(1 - \frac{N}{\kappa AG} \right) \frac{\partial^4 y(z,t)}{\partial t^2 \partial z^2} \right. \\
 & \left. + N \frac{\partial^2 y(z,t)}{\partial z^2} \right] - \frac{1}{\kappa AG} \left[mL^2 \frac{\partial^4 y(z,t)}{\partial t^2 \partial z^2} + C_s L^2 \frac{\partial^2 y(z,t)}{\partial z^2} - C_G \frac{\partial^4 y(z,t)}{\partial z^4} \right] + \frac{mr^2 L^4}{EI \kappa AG} \left[m \frac{\partial^4 y(z,t)}{\partial t^4} \right. \\
 & \left. + C_s \frac{\partial^2 y(z,t)}{\partial t^2} - \frac{C_G}{L^2} \frac{\partial^4 y(z,t)}{\partial z^2 \partial t^2} \right] = \frac{L}{\kappa AG} \frac{\partial^2 f(z,t)}{\partial z^2} + \frac{L^2 f(z,t)}{EI} + \frac{Lmr^2}{\kappa AGEI} \frac{\partial^2 f(z,t)}{\partial t^2}
 \end{aligned} \quad (7)$$

3. MODAL ANALYSIS PROCEDURE

3.1. Free Vibration Analysis

In Eqs. (1-7), deformations and internal forces of the beam element are defined as depending on the location and time variables. These parameters can be divided into two parts with the implementation of the method of the separation of variables as follows;

$$y(z,t) = \sum_{i=1}^{\infty} Y_i(z) q_i(t) \quad (8)$$

$$\theta(z,t) = \sum_{i=1}^{\infty} \Theta_i(z) q_i(t) \quad (9)$$

$$M(z,t) = \sum_{i=1}^{\infty} \bar{M}_i(z) q_i(t) \quad (10)$$

$$T(z,t) = \sum_{i=1}^{\infty} \bar{T}_i(z) q_i(t) \quad (11)$$

where i denotes the mode number and $Y_i(z)$, $\Theta_i(z)$, $\bar{M}_i(z)$, $\bar{T}_i(z)$ and $q_i(t)$ are the displacement, angle of rotation, bending moment, shear force shape functions and the normal coordinate function, respectively. In the free vibration case (for $f(z,t)=0$), the normal coordinate function can be taken as $q_i(t)=\sin(\omega_i t + \varphi)$. Thus, the Eq. (7) can be written in the following form.

$$\begin{aligned}
 & Y_i^{IV}(z) + L^2 \left(\frac{\kappa AG}{\kappa AG - N + C_G} \right) \left[\frac{m\omega_i^2 - C_s}{\kappa AG} + \frac{(m\omega_i^2 r^2 + N - C_G)}{EI} + \frac{m\omega_i^2 r^2 (C_G - N)}{EI \kappa AG} \right] Y_i''(z) \\
 & + L^4 \left(\frac{\kappa AG}{\kappa AG - N + C_G} \right) \left[\frac{mr^2}{EI \kappa AG} (m\omega_i^4 - C_s \omega_i^2) - \frac{(m\omega_i^2 - C_s)}{EI} \right] Y_i(z) = 0
 \end{aligned} \quad (12)$$

where ω_i and φ denote the natural angular frequency of i^{th} mode and the phase angle. Then, the shape functions of the bending moment, shear force and angle of rotation are obtained as [23].

$$\begin{aligned} \bar{M}_i(z) &= EI \left[\left(\frac{C_s - m\omega_i^2}{\kappa AG} \right) Y_i(z) - \left(\frac{C_G - N}{\kappa AG} + 1 \right) \frac{Y_i''(z)}{L^2} \right] \\ \bar{T}_i(\xi) &= \frac{M_i'(z) - (m\omega_i^2 r^2 + N) Y_i'(z)}{\left(1 - \frac{m\omega_i^2 r^2}{\kappa AG} \right) L} \\ \Theta_i(z) &= \left(1 - \frac{N}{\kappa AG} \right) \frac{Y_i'(z)}{L} - \frac{\bar{T}_i(z)}{\kappa AG} \end{aligned} \tag{13}$$

In Eq. (13), it is seen that the displacement shape function is required to obtain $\bar{M}_i(z)$, $\bar{T}_i(z)$ and $\Theta_i(z)$. For this reason, the displacement shape function should be obtained at first. For this purpose, Eq. (12) can be written as;

$$Y_i^{IV}(z) + a_i Y_i''(z) + b_i Y_i(z) = 0 \tag{14}$$

where

$$a_i = \left(\frac{L^2 \kappa AG}{\kappa AG + C_G} \right) \left[\frac{m\omega_i^2 - C_s}{\kappa AG} + \frac{(m\omega_i^2 r^2 + N - C_G)}{EI} + \frac{m\omega_i^2 r^2 (C_G - N)}{EI \kappa AG} \right] \tag{15}$$

$$b_i = \left(\frac{mr^2 \omega_i^2}{\kappa AG} - 1 \right) \left[\frac{L^4 \kappa AG (m\omega_i^2 - C_s)}{(\kappa AG + C_G - N) EI} \right] \tag{16}$$

The roots of the differential equation given in Eq. (14) are obtained as;

$$\lambda_1^2 = \frac{-a_i - \sqrt{a_i^2 - 4b_i}}{2} \quad \lambda_2^2 = \frac{-a_i + \sqrt{a_i^2 - 4b_i}}{2} \tag{17}$$

Although the differential equation given in Eq. (14) involves six different solutions depending on the sign of λ_1^2 and λ_2^2 , only three of them, Case-I: $\lambda_1^2 < 0$ and $\lambda_2^2 > 0$, Case-II: $\lambda_1^2 < 0$ and $\lambda_2^2 = 0$, and Case-III: $\lambda_1^2 < 0$ and $\lambda_2^2 < 0$ are physically possible. If the beam rests on a uniform elastic soil and the rotary inertia is considered, the lower modes satisfy Case-I for $\omega_i^2 < \kappa AG / (mr^2)$. However, this case is violated for higher modes and case-II and III is satisfied for $\omega_i^2 = \kappa AG / (mr^2)$ and $\omega_i^2 > \kappa AG / (mr^2)$, respectively. In the case that the rotary inertia is neglected, the Case-I will satisfy all modes since the $\kappa AG / (mr^2)$ will be infinite. Thus, the shape functions are obtained for Case-I, Case-II and Case-III as follows.

For Case-I: $\lambda_1^2 < 0$ and $\lambda_2^2 > 0$;

$$Y_i(z) = C_1 \cos \lambda_1 z + C_2 \sin \lambda_1 z + C_3 \cosh \lambda_2 z + C_4 \sinh \lambda_2 z \tag{18}$$

$$\Theta_i(z) = C_1 K_5 \sin \lambda_1 z + C_2 K_6 \cos \lambda_1 z + C_3 K_7 \sinh \lambda_2 z + C_4 K_7 \cosh \lambda_2 z \tag{19}$$

$$\bar{M}_i(z) = C_1 K_1 \cos \lambda_1 z + C_2 K_1 \sin \lambda_1 z + C_3 K_2 \cosh \lambda_2 z + C_4 K_2 \sinh \lambda_2 z \tag{20}$$

$$\bar{T}_i(z) = C_1 K_3 \sin \lambda_1 z - C_2 K_3 \cos \lambda_1 z + C_3 K_4 \sinh \lambda_2 z + C_4 K_4 \cosh \lambda_2 z \tag{21}$$

where

$$\lambda_1 = \sqrt{\frac{a_i + \sqrt{a_i^2 - 4b_i}}{2}} \quad \lambda_2 = \sqrt{\frac{-a_i + \sqrt{a_i^2 - 4b_i}}{2}} \tag{22}$$

and

$$K_1 = \left(\frac{EI(C_s - m\omega_i^2)}{\kappa AG} \right) + \left(\frac{C_G - N}{\kappa AG} + 1 \right) \frac{EI\lambda_1^2}{L^2} ,$$

$$K_2 = \left(\frac{EI(C_s - m\omega_i^2)}{\kappa AG} \right) - \left(\frac{C_G - N}{\kappa AG} + 1 \right) \frac{EI\lambda_2^2}{L^2} \tag{23}$$

$$K_3 = \frac{\lambda_1(-K_1 + (m\omega_i^2 r^2 + N))}{L(-m\omega_i^2 r^2 / \kappa AG + 1)} , \quad K_4 = \frac{\lambda_2(K_2 - (m\omega_i^2 r^2 + N))}{L(-m\omega_i^2 r^2 / \kappa AG + 1)} , \quad K_5 = \left(\frac{-\lambda_1}{L} - \frac{K_3}{\kappa AG} \right)$$

$$K_6 = \frac{\lambda_1}{L} \left(1 - \frac{N}{\kappa AG} \right) - \frac{K_3}{\kappa AG} , \quad K_7 = \frac{\lambda_2}{L} \left(1 - \frac{N}{\kappa AG} \right) - \frac{K_4}{\kappa AG}$$

For Case-II: $\lambda_1^2 < 0$ and $\lambda_2^2 = 0$;

$$Y_i(z) = C_1 \cos \lambda_1 z + C_2 \cos \lambda_1 z + C_3 z + C_4 \tag{24}$$

$$\Theta_i(z) = C_1 K_5 \sin \lambda_1 z - C_2 K_6 \sin \lambda_1 z + C_3 K_7 \tag{25}$$

$$\bar{M}_i(z) = C_1 K_1 \cos \lambda_1 z + C_2 K_1 \cos \lambda_1 z + C_3 K_2 z + C_4 K_2 \tag{26}$$

$$\bar{T}_i(z) = C_1 K_3 \sin \lambda_1 z - C_2 K_3 \sin \lambda_1 z + C_3 K_4 \tag{27}$$

and

$$\begin{aligned}
 K_1 &= \left(\frac{EI(C_s - m\omega_i^2)}{\kappa AG} \right) + \left(\frac{C_G - N}{\kappa AG} + 1 \right) \frac{EI\lambda_1^2}{L^2}, \quad K_2 = \left(\frac{EI(C_s - m\omega_i^2)}{\kappa AG} \right) \\
 K_3 &= \frac{\lambda_1(-K_1 + (m\omega_i^2 r^2 + N))}{L(-m\omega_i^2 r^2 / \kappa AG + 1)}, \quad K_4 = \frac{\lambda_2(-K_2 + (m\omega_i^2 r^2 + N))}{L(-m\omega_i^2 r^2 / \kappa AG + 1)}, \quad K_5 = \left(-\frac{\lambda_1}{L} - \frac{K_3}{\kappa AG} \right) \\
 K_6 &= \frac{\lambda_1}{L} \left(1 - \frac{N}{\kappa AG} \right) - \frac{K_3}{\kappa AG}, \quad K_7 = -\frac{1}{L} \left(1 - \frac{N}{\kappa AG} \right) - \frac{K_4}{\kappa AG}
 \end{aligned} \tag{28}$$

For Case-III: $\lambda_1^2 < 0$ and $\lambda_2^2 < 0$;

$$Y_i(z) = C_1 \cos \lambda_1 z + C_2 \sin \lambda_1 z + C_3 \cos \lambda_2 z + C_4 \sin \lambda_2 z \tag{29}$$

$$\theta_i(z) = C_1 K_5 \sin \lambda_1 z + C_2 K_6 \cos \lambda_1 z + C_3 K_7 \sin \lambda_2 z + C_4 K_8 \cos \lambda_2 z \tag{30}$$

$$\bar{M}_i(z) = C_1 K_1 \cos \lambda_1 z + C_2 K_1 \sin \lambda_1 z + C_3 K_2 \cos \lambda_2 z + C_4 K_2 \sin \lambda_2 z \tag{31}$$

$$\bar{T}_i(z) = C_1 K_3 \sin \lambda_1 z - C_2 K_3 \cos \lambda_1 z + C_3 K_4 \sin \lambda_2 z - C_4 K_4 \cos \lambda_2 z \tag{32}$$

where

$$\lambda_1 = \sqrt{\frac{a_i + \sqrt{a_i^2 - 4b_i}}{2}}, \quad \lambda_2 = \sqrt{\frac{a_i - \sqrt{a_i^2 - 4b_i}}{2}} \tag{33}$$

and

$$\begin{aligned}
 K_1 &= \left(\frac{EI(C_s - m\omega_i^2)}{\kappa AG} \right) + \left(\frac{C_G - N}{\kappa AG} + 1 \right) \frac{EI\lambda_1^2}{L^2}, \quad K_2 = \left(\frac{EI(C_s - m\omega_i^2)}{\kappa AG} \right) + \left(\frac{C_G - N}{\kappa AG} + 1 \right) \frac{EI\lambda_2^2}{L^2} \\
 K_3 &= \frac{\lambda_1(-K_1 + (m\omega_i^2 r^2 + N))}{L(-m\omega_i^2 r^2 / \kappa AG + 1)}, \quad K_4 = \frac{\lambda_2(-K_2 + (m\omega_i^2 r^2 + N))}{L(-m\omega_i^2 r^2 / \kappa AG + 1)}, \quad K_5 = \left(-\frac{\lambda_1}{L} - \frac{K_3}{\kappa AG} \right) \\
 K_6 &= \frac{\lambda_1}{L} \left(1 - \frac{N}{\kappa AG} \right) - \frac{K_3}{\kappa AG}, \quad K_7 = -\frac{\lambda_2}{L} \left(1 - \frac{N}{\kappa AG} \right) - \frac{K_4}{\kappa AG}, \quad K_8 = \frac{\lambda_2}{L} \left(1 - \frac{N}{\kappa AG} \right) + \frac{K_4}{\kappa AG}
 \end{aligned} \tag{34}$$

An iterative computer program that determines the natural angular frequencies and mode shapes for the beam on an elastic foundation has been prepared by the authors. This program obtains the natural angular frequencies, and mode shapes for generalized end conditions. Here, the end conditions are defined by elastic supports with the coefficients of C_{y0} , $C_{\theta0}$, C_{y1} , $C_{\theta1}$ as below;

$$\begin{aligned}
 C_{y0}y(z=0) + T(z=0) &= 0 \\
 C_{\theta0}\theta(z=0) + M(z=0) &= 0 \\
 C_{y1}y(z=1) + T(z=1) &= 0 \\
 C_{\theta1}\theta(z=1) + M(z=1) &= 0
 \end{aligned}
 \tag{35}$$

Then, the coefficient matrix is obtained as follows;

for Case-I;

$$\Delta = \begin{pmatrix} C_{y0} & -K_3 & C_{y0} & -K_4 \\ K_1 & K_6 C_{\theta0} & K_2 & K_7 C_{\theta0} \\ (C_{y1} \cos \lambda_1 + K_3 \sin \lambda_1) & (C_{y1} \sin \lambda_1 - K_3 \cosh \lambda_1) & (C_{y1} \cosh \lambda_2 + K_2 \sinh \lambda_1) & (C_{y1} \sinh \lambda_2 + K_4 \cosh \lambda_2) \\ (C_{\theta1} K_5 \sin \lambda_1 + K_1 \cos \lambda_1) & (C_{\theta1} K_6 \cos \lambda_1 + K_1 \sin \lambda_1) & (C_{\theta1} K_7 \sinh \lambda_2 + K_1 \cosh \lambda_2) & (C_{\theta1} K_6 \cosh \lambda_2 + K_2 \sinh \lambda_2) \end{pmatrix}
 \tag{36}$$

for Case-II;

$$\Delta = \begin{pmatrix} C_{y0} & -K_3 & C_{y0} & 0 \\ K_1 & K_6 C_{\theta0} & K_2 & 0 \\ (C_{y1} \cos \lambda_1 + K_3 \sin \lambda_1) & (C_{y1} \sin \lambda_1 - K_3 \cos \lambda_1) & (C_{y1} \cos \lambda_2 + K_3) & (C_{y1} \sin \lambda_2) \\ (C_{\theta1} K_5 \sin \lambda_1 + K_1 \cos \lambda_1) & (C_{\theta1} K_6 \cos \lambda_1 + K_1 \sin \lambda_1) & (C_{\theta1} K_7 \sin \lambda_2 + K_1) & 0 \end{pmatrix}
 \tag{37}$$

for Case-III;

$$\Delta = \begin{pmatrix} C_{y0} & -K_3 & C_{y0} & -K_4 \\ K_1 & K_6 C_{\theta0} & K_2 & K_7 C_{\theta0} \\ (C_{y1} \cos \lambda_1 + K_3 \sin \lambda_1) & (C_{y1} \sin \lambda_1 - K_3 \cos \lambda_1) & (C_{y1} \cos \lambda_2 + K_3 \sin \lambda_1) & (C_{y1} \sin \lambda_2 - K_4 \cos \lambda_2) \\ (C_{\theta1} K_5 \sin \lambda_1 + K_1 \cos \lambda_1) & (C_{\theta1} K_6 \cos \lambda_1 + K_1 \sin \lambda_1) & (C_{\theta1} K_7 \sin \lambda_2 + K_1 \cos \lambda_{21}) & (C_{\theta1} K_8 \cos \lambda_2 + K_2 \sin \lambda_2) \end{pmatrix}
 \tag{38}$$

The coefficients of C_2 , C_3 and C_4 can be obtained as below by setting, $C_1 = 1$.

$$\begin{pmatrix} C_2 \\ C_3 \\ C_4 \end{pmatrix} = \begin{pmatrix} \Delta_{22} & \Delta_{23} & \Delta_{24} \\ \Delta_{32} & \Delta_{33} & \Delta_{34} \\ \Delta_{42} & \Delta_{43} & \Delta_{44} \end{pmatrix}^{-1} \times \begin{pmatrix} -\Delta_{21} \\ -\Delta_{31} \\ -\Delta_{41} \end{pmatrix}
 \tag{39}$$

Once, C_2 , C_3 and C_4 are obtained, $Y_i(z)$ can be normalized so that its maximum value will be equal to 1.

3.2. Forced Vibration Analysis

Once the natural angular frequencies and free vibration mode shapes are obtained, the rest of the problem can be easily solved numerically. The forced vibration case can be handled as a set of linear algebraic equations by deriving the uncoupled equations of motion. Finally, a

linear dynamic analysis can be performed. For this propose, the separation of variables method can be applied to the Eqs. (1) and (2).

$$\sum_{i=1}^{\infty} \left[mY_i(\xi)\ddot{q}_i(t) + \left(C_s Y_i(z) - \frac{1}{L^2} C_G Y_i''(\xi) - \frac{1}{L} \bar{T}_i'(z) \right) q_i(t) \right] = f(z,t) \tag{40}$$

$$\sum_{i=1}^{\infty} \left[mr^2 \Theta_i(z)\ddot{q}_i(t) + \left(\frac{1}{L} \bar{M}_i'(z) - \frac{1}{L} NY_i'(z) - \bar{T}_i(z) \right) q_i(t) \right] = 0 \tag{41}$$

Multiplying the both sides of Eq. (40) by $Y_j(z)$, and Eq. (41) by $\Theta_j(z)$, and integrating them along the beam length, the following equation is obtained according to the rule of the orthogonality of modes.

$$\int_0^1 mL Y_j^2(z) \ddot{q}_j(t) dz + \int_0^1 Y_j(z) \left(LC_s Y_j(z) - \frac{C_G Y_j''(z)}{L} - \bar{T}_j(z) \right) q_j(t) dz = \int_0^1 mL Y_j(z) \ddot{q}_j(t) dz \tag{42}$$

$$\int_0^1 mL \Theta_j^2(z) \ddot{q}_j(t) dz + \int_0^1 \Theta_j(z) \left(\bar{M}'(z) - NY_j'(z) - L\bar{T}_j(z) \right) q_j(t) dz = 0 \tag{43}$$

Assembling Eqs. (42) and (43) yields,

$$M_j \ddot{q}_j(t) + K_j q_j(t) = F_j(t) \tag{44}$$

where M_j , K_j , and $F_j(t)$ denote the generalized mass, stiffness, and load at the j^{th} mode, respectively.

$$\begin{aligned} M_j &= mL \int_0^1 \left[Y_j^2(z) + r^2 \Theta_j^2(z) \right] dz \\ K_j &= \int_0^1 \left\{ Y_j(z) \left(LC_s Y_j(z) - \frac{C_G Y_j''(z)}{L} - \bar{T}_j(z) \right) + \Theta_j(z) \left(\bar{M}'(z) - NY_j'(z) - L\bar{T}_j(z) \right) \right\} dz \\ F_j(t) &= L \int_0^1 Y_j(z) f(z,t) dz \end{aligned} \tag{45}$$

Substituting $K_j=M_j\omega_j^2$ into Eq. (44) leads to the following equation

$$\ddot{q}_j(t) + \omega_j^2 q_j(t) = \frac{F_j(t)}{M_j} \tag{46}$$

Thus, the normal coordinate function can be obtained by the solution of Eq. (46).

4. CALCULATION OF SOIL PARAMETERS

The first parameter of the elastic soil which represents the modulus of transverse deformation can be evaluated by using the formulas given for the Winkler foundation model. On the other hand, the calculation of the second parameter is directly related to the type of the two-parameter elastic soil model. Vlasov and Leont'ev [13] proposed a formula for the calculation of the first and second parameters for rectangular beams on an elastic soil layer. These formulas were simplified by Zhaohua and Cook [24] for a semi-infinite elastic medium as given below.

$$C_s = \frac{E_o \bar{b}}{2(1-\nu_o^2)} \frac{\bar{\gamma}}{l} \quad C_G = \frac{E_o \bar{b}}{4(1+\nu_o)} \frac{l}{\bar{\gamma}} \tag{47}$$

where, \bar{b} denotes the width of the beam. The parameter of $\bar{\gamma}$ is defined by Vlasov and Leont'ev as a coefficient that characterizes the decrease of deflections with depth and commonly taken as $\bar{\gamma} = 1$. Parameters of l, E_o, ν_o are given in the following equation.

$$l = \sqrt[3]{\frac{2EI(1-\nu_o^2)}{(1-\nu^2)E_o \bar{b}}} \tag{48}$$

$$E_o = \frac{E_s}{1-\nu_s^2} \quad \nu_o = \frac{\nu_s}{1-\nu_s} \tag{49}$$

where E_s, ν_s and ν denotes the modulus of elasticity and Poisson's ratio of the soil and the beam, respectively.

5. NUMERICAL RESULTS AND DISCUSSIONS

5.1. Verification Example

A numerical example which was previously studied by Yokoyama [15], and Calio and Greco [21] is presented to verify the presented solution procedure. The free vibration of the axially loaded hinged-hinged and fixed-hinged beam on Winkler and Pasternak foundation is investigated and analysis results are compared with those of the Yokoyama [15], and Calio and Greco [21]. The beam and soil properties are calculated according to the non-dimensional parameters below [25].

$$\bar{n} = \frac{NL^2}{\pi^2 EI} \tag{50}$$

$$\bar{c}_s = \frac{C_s L^2}{EI} \tag{51}$$

$$\bar{c}_g = \frac{C_G L^2}{\pi^2 EI} \tag{52}$$

Where \bar{n} , \bar{c}_s and \bar{c}_g denotes the dimensionless axial force, the first and second parameters of the elastic soil. The dimensionless frequency parameters, $\Omega_i = EI / (L^4 \omega_i^2 m)$ of the first three modes obtained for the hinged-hinged and fixed-hinged beam are presented in Table-1 and 2, respectively. In Table-1, the frequency parameter obtained by the present study is found to be very close to the results presented by Yokoyama [15]. A small difference is obtained in second and third mode due to the fact that Yokoyama [15] presents a finite element solution by using 16 bar elements. Note that the difference with the Yokoyama solution [15] decreases for Vlasov type foundation as given in Table-2. In addition, a good agreement is obtained with the exact analytical results presented by Calio and Greco [21].

Table 1 - Frequency parameters obtained for $\bar{n}=0.6$, $\bar{c}_s=0.6\pi^4$ and $\bar{c}_g=0$ ($\kappa=2/3$ and $L/r=10.0$)

Mode Number	Hinged-Hinged		Fixed-Hinged	
	Present Study	Yokoyama [15]	Present Study	Yokoyama [15]
1	8.22	8.22	10.46	10.49
2	20.59	20.67	22.20	22.30
3	35.86	36.25	36.50	36.90

Table 2 - Frequency parameters obtained for $\bar{n}=0.6$, $\bar{c}_s=0.6\pi^4$ and $\bar{c}_g=1$ ($\kappa=2/3$ and $L/r=10.0$)

Mode Number	Hinged-Hinged			Fixed-Hinged	
	Present Study	Yokoyama [15]	Calio and Greco [21]	Present Study	Yokoyama [15]
1	12.64	12.64	12.64	14.42	14.42
2	28.03	28.10	28.02	29.30	29.34
3	45.92	46.34	45.92	46.70	46.74

The variation of dimensionless eigenvalues $\mu_1 = \lambda_1^2 EI / (L^4 \omega_1^2 m)$ and $\mu_2 = \lambda_2^2 EI / (L^4 \omega_1^2 m)$ for the hinged-hinged and fixed-hinged support conditions are given in Figures 3-4, respectively. When the rotary inertia is neglected, Case-I is satisfied for all modes. For the hinged-hinged beam, when the rotary inertia is considered, Case-I is violated starting from the 4th and 5th modes, for the Winkler and Vlasov foundations, respectively. However, the higher modes satisfy Case-III. For the fixed-hinged beam, Case-I is satisfied up to the 3rd mode.

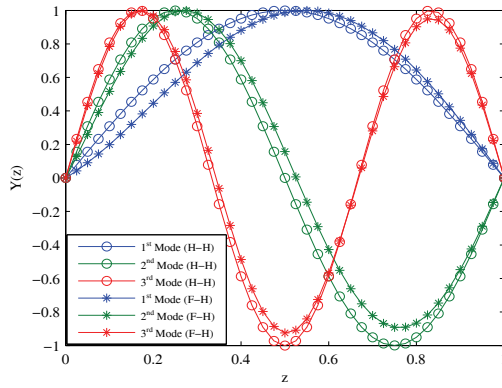


Figure 2 - Normalized mode shape functions obtained for first three modes

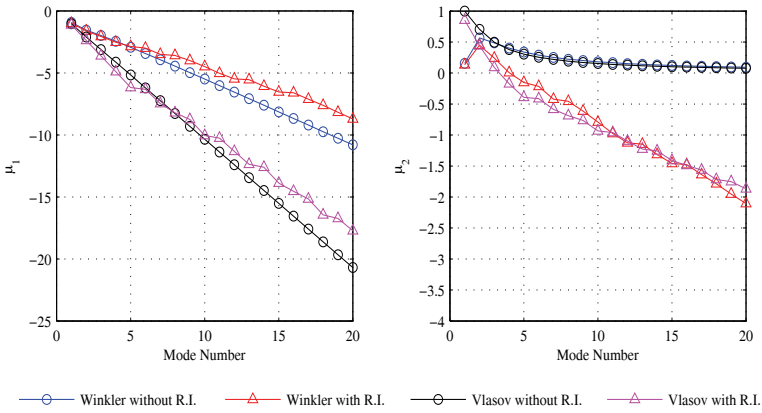


Figure 3 - Normalized eigenvalues for the hinged-hinged beam

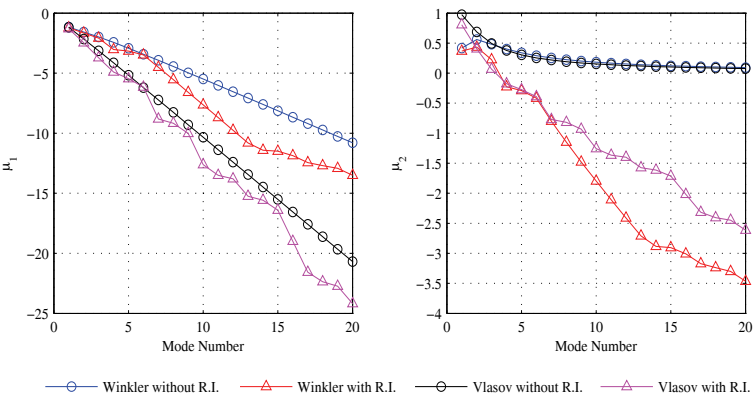


Figure 4 - Normalized eigenvalues for the fixed-hinged beam

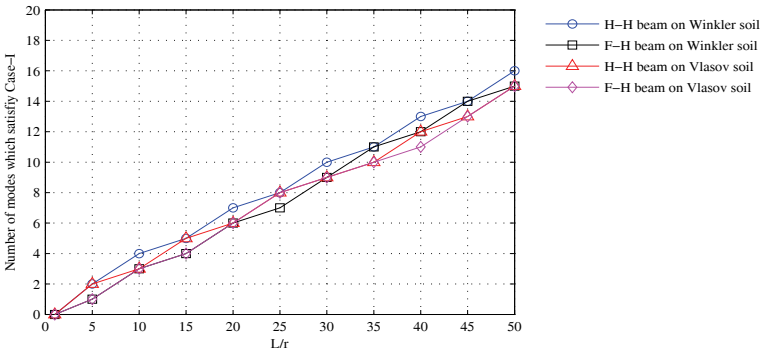


Figure 5 - Variation of the number of modes satisfying Case-I versus slenderness ratio

Figure 5 shows the variation of the number of modes that satisfy Case-I versus the slenderness ratio, L/r . It is seen that the number of modes that satisfy the Case-I is proportional to the slenderness ratio while some differences are observed according to the boundary conditions and soil model.

5.2. Comprehensive Example

In this numerical analysis, the dynamic response of an axially loaded $1^m \times 1^m$ square beam on Vlasov foundation is investigated. The beam has distributed mass and elasticity, and it is subjected to a concentrated dynamic load $f(z,t) = \delta(z-1/2)F(t)$. The material properties of the beam: $E = 28,000 \text{ MPa}$, $G = 11,666.67 \text{ MPa}$, $m = 2.548 \text{ kN}\cdot\text{s}^2/\text{m}$, $r = 0.2887\text{m}$ and $\kappa = 2/3$. Elastic soil properties are calculated as $C_S = 17,470 \text{ kN/m}^2$ and $C_G = 68,688 \text{ kN}$ (for sand and gravel, $E_s = 100,000 \text{ MPa}$, $\nu_s = 0.25$). In the analysis, four different boundary conditions; free-free ($C_{y0} = C_{\theta0} = C_{y1} = C_{\theta1} = 0$), hinged-hinged ($C_{y0} = C_{y1} \approx \infty$ and $C_{\theta1} = C_{\theta0} = 0$), fixed-hinged ($C_{y0} = C_{\theta0} = C_{y1} \approx \infty$ and $C_{\theta1} = 0$), and fixed-fixed ($C_{y0} = C_{\theta0} = C_{y1} = C_{\theta1} \approx \infty$) are considered. Axial compressive load of the beam is calculated by Euler critical buckling load formula, $N_b = \pi^2 EI/L_b^2$, for all boundary conditions (see Table-3).

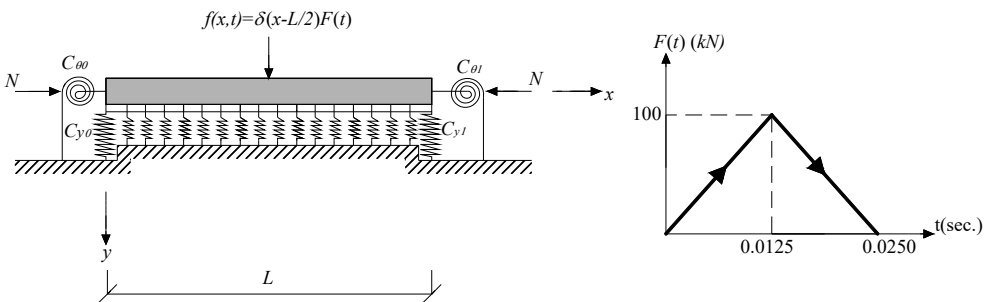


Figure 6 - Timoshenko beam on Vlasov foundation and time dependent load function

Table 3 - Effective length and critical buckling loads according to the end conditions

End Conditions	Effective Length, L_b	Buckling Load, N_b (kN)
Free-Free	L	23029
Hinged-Hinged	L	23029
Fixed-Hinged	$0.7L$	46998
Fixed-Fixed	$0.5L$	92116

In Figures 7-8, the variation of the maximum bending moment at $z \approx 0.5$ versus the number of considered modes is presented. 95 % convergence to the exact value is observed by the contribution of first 5-6 for all boundary conditions. In addition, it is observed that the maximum bending moment is less affected by the rotary inertia when the axial compressive force effect is omitted. An increase about 4%, however, is observed for hinged-hinged beam on Winkler foundation with the rotary inertia effect. In addition, the bending moment response for the Winkler foundation is observed to be larger than Vlasov type foundation about 15, 8 and 7.5 % for hinged-hinged, fixed-hinged and fixed-fixed cases, respectively. In the case where the axial compressive load is considered, the convergence speed of the bending moment response does not change significantly except for the free-free and hinged-hinged beam on the Vlasov foundation. For this case, the exact response can be obtained by the first mode only. However, an increase 125, 312, 324% in the bending moment response is observed for the free-free, hinged-hinged and fixed-hinged beam on Vlasov and Winkler foundations, while no difference is detected for the fixed-fixed beam.

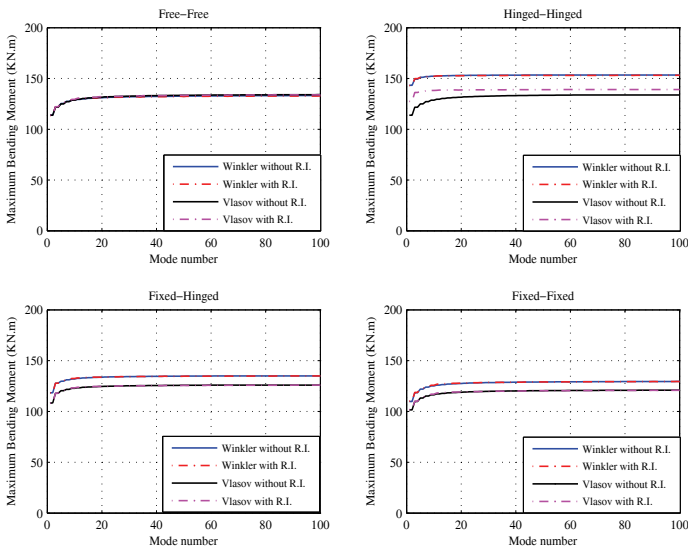


Figure 7 - Variation of maximum bending moment at $z = 0.5$ versus considered number of modes for $N = 0$

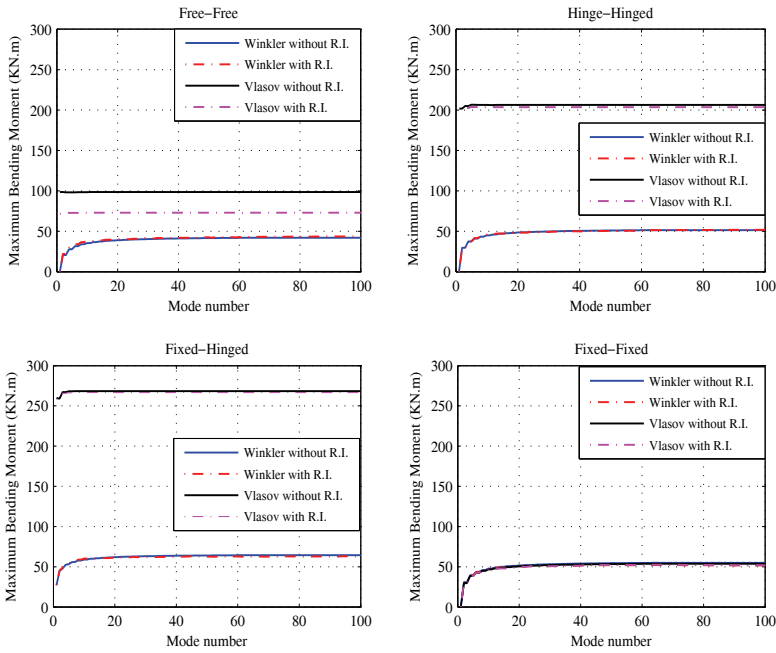


Figure 8 - Variation of maximum bending moment at $z = 0.5$ versus considered number of modes for $N = N_b$

In Figures 9-10, the variation of the maximum shear force at $z \approx 0.5$ versus considered mode number is presented. At first, it appears that the shear force responses with and without the rotary inertia are the same in lower modes for both Winkler and Vlasov foundations. However, a difference is observed with the contribution of higher modes. The exact shear force responses have similar values for Winkler and Vlasov foundations. The convergence to the exact value is obtained with less number of modes without the effect of rotary inertia. For the free-free and hinged-hinged beam, it is observed that taking of first 25-30 modes into account gives 90-95% convergence to the exact value without the rotary inertia effect. This convergence value, however, is satisfied by taking 40-45 modes into account if the rotary inertia is considered. For the fixed-hinged and fixed-fixed beam, this convergence is obtained by 15-20 and 25-30 modes without and with the rotary inertia effect, respectively. On the other hand, in the case that the axial compressive load is considered, these convergence ratios are obtained for free-free and hinged-hinged beam without rotary inertia by the contribution of 35-40 modes and 55-60 modes with rotary inertia. For the fixed-hinged and fixed-fixed beam, 90-95% convergence is obtained by the contribution of 40-50 modes except the fixed-fixed beam on Vlasov type foundation. If the axial compressive load is neglected, a small decrease occurs in the maximum shear force response for Winkler and Vlasov type foundations with rotary inertia.

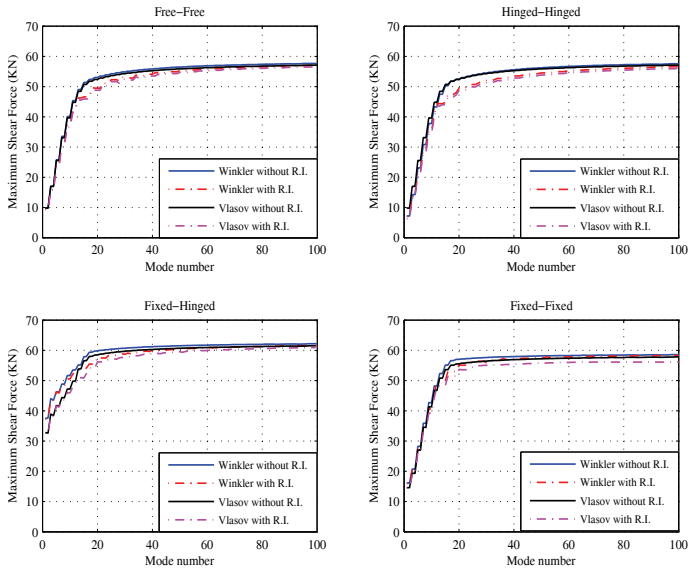


Figure 9 - Variation of maximum shear force at $z \approx 0.5$ versus considered number of modes for $N=0$

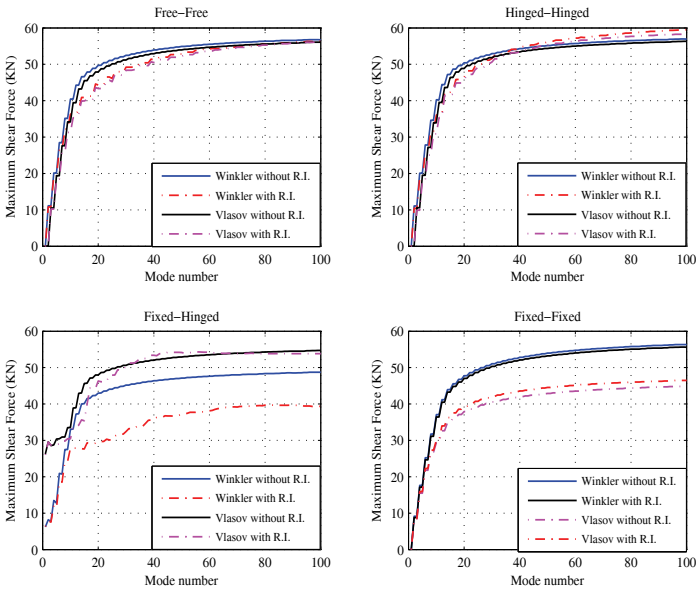


Figure 10 - Variation of maximum shear force at $z \approx 0.5$ versus considered number of modes for $N= N_b$

In the case when the axial compressive load contribution is considered, an increase about 4.50%, 20.50% for Winkler, and 3.50%, 28% for Vlasov foundation is observed by the effect of rotary inertia for the hinged-hinged and fixed-fixed beams, respectively. In addition, a decrease is observed about 19.25% for the fixed-hinged beam on Winkler foundation. Vlasov type foundation causes an increase about 11% and 38% in the shear force response for fixed-hinged beam with and without the rotary inertia, respectively. On the other hand, a negligible difference is observed for free-free, hinged-hinged and fixed-fixed beams.

6. CONCLUSIONS

In this study, a comprehensive analysis on the effect of rotary inertia and higher modes on the dynamic response of Timoshenko beams on two-parameter foundation with generalized end condition is presented. The results are summarized below.

- In case of the consideration of rotary inertia, the solution of the differential equation for the free vibration case may change depending on the slenderness ratio, L/r . Here, three different cases (Case- I, II and III) are possible due to the slenderness ratio. In most researches in the literature, only the Case-I is considered as the solution. When the higher modes are considered, however, Case-II and/or III may arise.
- According to the numerical results, it is seen that the number of modes which satisfy Case-I increases with the slenderness ratio. In addition, it is seen that the number of modes that satisfy Case-I not only depends on the slenderness ratio but are also affected by the boundary conditions and elastic soil model.
- Numerical results indicate that the required number of modes increases by the effect of rotary inertia. On the other hand, the exact solution may be obtained by the contribution of less number of modes as depending on the number of constrained degrees of freedom at the ends.
- For the fixed-hinged beam on Winkler foundation and fixed-fixed beam on Winkler and Vlasov foundations, the axial compressive load causes a significant difference in the shear force response of the beam by the rotary inertia. In addition, the axial force increases the required number of modes for the shear force response except the fixed-fixed beam with rotary inertia.

References

- [1] Doyle, P.F. and Pavlovic, M., Vibration of beams on partial elastic foundations. *Earthquake Engineering and Structural Dynamics*, 10(5), 663–674, 1982.
- [2] West, H. H. and Mafi, M., Eigenvalues for beam-columns on elastic supports. *Journal of Structural Engineering*, 110(6), 1305–1320, 1984.
- [3] Çatal, H. H., Free vibration of partially supported piles with the effects of bending moment, axial and shear force. *Engineering Structures*, 24(12), 1615-1622, 2002.

- [4] Çatal, H. H., Free vibration of semi-rigid connected and partially embedded piles with the effects of the bending moment, axial and shear force. *Engineering Structures*, 28(14), 1911-1918, 2006.
- [5] Yeşilce, Y. and Çatal, H. H., Free vibration of piles embedded in soil having different modulus of subgrade reaction. *Applied Mathematical Modelling*, 32(5), 889-900.
- [6] Çatal, S., Solution of free vibration equations of beam on elastic soil by using differential transform method. *Applied Mathematical Modelling*, 32(9), 1744-1757, 2008.
- [7] Yeşilce, Y. and Çatal, S., Free vibration of axially loaded Reddy-Bickford beam on elastic soil using the differential transform method, *Struct. Eng. Mech.* 31(4), 453-475, 2009.
- [8] Yeşilce, Y. and Çatal, H. H., Solution of free vibration equations of semi-rigid connected Reddy-Bickford beams resting on elastic soil using the differential transform method. *Archive of Applied Mechanics*, 81(2), 199-213, 2011.
- [9] Sapountzakis, E. J. and Kampitsis, A. E., Nonlinear dynamic analysis of Timoshenko beam-columns partially supported on tensionless Winkler foundation, *Computers and Structures*, 88(21-22), 1206-1219, 2010.
- [10] Çatal, S., Response of forced Euler-Bernoulli beams using differential transform method. *Struct. Eng. Mech.* 42(1), 95-119, 2012.
- [11] Öztürk, B. and Coşkun, S. B., Analytical solution for free vibration analysis of beam on elastic foundation with different support conditions. *Mathematical Problems in Engineering*, 2013, 1-7, 2013.
- [12] Pasternak P.L., On a new method of analysis on elastic foundation by means of two constants. *Gosudarstvennoe Izdatel'stvo Literaturi po Stroitel'stvu i Arkhitekture*, 1954.
- [13] Vlasov, V.Z. and Leont'ev, U.N., *Beams, plates and shells on elastic foundations*. Israel Program for Scientific Translations, Jerusalem, 1966.
- [14] Morfidis, K. and Avramidis, I. E., Formulation of a generalized beam element on a two-parameter elastic foundation with semi-rigid connections and rigid offsets. *Computers and Structures*, 80(25), 1919-1934, 2002.
- [15] Yokoyama, T., Vibration analysis of Timoshenko beam-columns on two-parameter elastic foundation. *Computers and Structures*, 61(6), 995-1007, 1996.
- [16] Arboleda-Monsalve, L. G., Zapata-Medina, D. G. and Aristizabal-Ochoa, J. D., Timoshenko beam-column with generalized end conditions on elastic foundation. Dynamic-stiffness matrix and load vector. *Journal of Sound and Vibration*, 310(4-5), 1057-1079, 2008.
- [17] Balkaya, M., Kaya, M. O. and Sağlamer, A., Analysis of the vibration of an elastic beam supported on elastic soil using the differential transform method. *Arch. Appl. Mech.* 79(2), 135-146, 2009.

- [18] Celep, Z., Güler, K. and Demir, F., Response of a completely free beam on a tensionless Pasternak foundation subjected to dynamic load. *Structural Engineering and Mechanics*, 37(1), 61-77, 2011.
- [19] Malekzadeh, P. and Karami, G., A mixed differential quadrature and finite element free vibration and buckling analysis of thick beams on two-parameter elastic foundations. *Applied Mathematical Modelling* 32(7), 1381-1394, 2008.
- [20] Morfidis, K., Vibration of Timoshenko beams on three-parameter elastic foundation. *Computers and Structures*, 88(5-6), 294-308, 2010.
- [21] Calio, I. and Greco, A., Free vibrations of Timoshenko beam-columns on Pasternak foundations. *Journal of Vibration and Control*. 19(5), 686-696, 2012.
- [22] Hassan, M. T. and Nassar, M., Analysis of stressed Timoshenko beams on two parameter foundations. *KSCE Journal of Civil Engineering*, 19(1), 173-179, 2015.
- [23] Hızal, Ç. and Çatal, H. H., Comparative dynamic analysis of axially loaded beams on modified Vlasov foundation. *Structural Engineering and Mechanics*, 57(6), 969-988, 2016.
- [24] Zhaohua, F. and Cook, R.D., Beam elements on two-parameter elastic foundations. *Journal of Engineering Mechanics*, 109(6), 1390-402 (1983)
- [25] De Rosa, M. A., Free Vibrations of Timoshenko Beams on Two Parameter Elastic Foundation. *Computers and Structures*, 57(1), 151-156, 1995.

Roughness Coefficient of a Highly Calcinated Penstock

Kutay ÇELEBİOĞLU¹

ABSTRACT

When highly calcinated water is transferred through the penstock of a hydropower plant it leaves a residue on the pipe surface. Accumulated residue over time causes a change in the roughness of the pipe surface thus leads to friction losses in the system. The effect is a change in head and discharge relation for the turbines. A multimethodology is proposed for determining the apparent surface roughness value (ϵ) by means of friction factor f and measuring arithmetic mean deviation of the roughness profile (R_a), root mean square roughness (R_q) and peak and valley roughness (R_z). It is found that a surface roughness value (ϵ) of 0.3mm can be used for calcinated surfaces which is much higher than steel surfaces but smaller than a concrete surface.

Keywords: Friction factor, surface roughness, calcination.

1. INTRODUCTION

Energy output of hydropower plants (HPP) depends on the net head and flow rate supplied to the turbines. Water is conveyed from a reservoir or a head pond to the power house by means of water conduits called penstocks. Systems are designed such that the energy output is maximized while minimizing the cost [1]. Part of the available energy is lost due to pipe friction and other local losses. Available energy conveyed to the turbines, hence the amount of energy produced, depends on the amount left after these losses.

When highly calcinated water is transferred through the penstock of a hydropower plant it leaves a residue on the pipe surface. Such residues accumulate over time forming a thick layer on the surfaces in contact with water. There are two important aspects of this calcination, one is the change in the surface roughness coefficient the other is the change in the actual flow diameter. While the effect of the first one is not known a priori, the second one causes a decrease in flow diameter and an increase in the average velocity, increasing losses in the penstock system.

Note:

- This paper has been received on July 24, 2018 and accepted for publication by the Editorial Board on November 23, 2018.
- Discussions on this paper will be accepted by September 30, 2019.

• <https://dx.doi.org/10.18400/tekderg.447265>

¹ TOBB University of Economics and Technology, Hydro Energy Research Center, Ankara, Turkey - tkcelebioglu@etu.edu.tr - <https://orcid.org/0000-0001-8845-4928>

Recently, a rehabilitation project for an old powerhouse (KEPEZ 1 HPP), located in the province of Antalya, was started. The Hydropower plant is equipped with three Francis type turbines with an installed capacity of 26.4 MW. It is the sixth largest power house in the region. The power house had been in operation for more than 30 years. The net head of the turbines is 162 m with a discharge of 6.1 m³/s. The aim of the rehabilitation project is to increase efficiency and output of the old turbines in the HPP by replacing them with new ones while renewing all auxiliary systems up to state-of-the-art requirements.

The hydro power plant consists of a head pond and an intake structure and diverts the flow through a pressurized concrete pipe followed by a surge tank and a long steel pipe. A problem concerning quality of water exists in the region, causing heavy calcination of pipes. Operating records of the power house suggests a calcination period that is as short as six months and a calcination thicknesses of up to 30 mm were observed in the penstock. Continuous cleaning of the water conduit is very costly and interrupts energy production because it requires emptying the penstock and hard scrubbing of the full conduit system. Thus, a new turbine to be installed on the old calcinated pipeline system will operate at different head than its design head and at different discharge conditions than its initial design. Therefore, the new turbine design should account for calcination and change in the friction losses in the system for varying flowrates.

Initial design net head and discharge through the turbines are determined using the design drawings. They are calculated from the well-established Darcy-Weisbach relation. When designing a new system, the equivalent roughness values of steel ($\epsilon=0.02 - 0.05\text{mm}$) and concrete pipes ($\epsilon=0.5\text{mm}$) are easily obtained from various engineering tables and the net head available to the turbine can easily be calculated [2]. Roughness coefficients of selected residue materials are also available in the literature [3]. But no information is available in literature for the apparent surface roughness value (ϵ) of a highly calcinated pipe surface. For this reason, a multimethodology is proposed that includes:

- 1.) A one-dimensional numerical model of the existing system which is built to calculate the steady state head and discharge relation for varying apparent surface roughness values (ϵ)
- 2.) Determination of combined friction coefficient based on site measurements of flow rate and turbine inlet pressure and head water level variations
- 3.) Determination of apparent surface roughness using laboratory measurements of surface profile and waviness of a sample calcinated block obtained from the site.

The numerical model is used to observe the variation in the combined friction coefficient of the system by changing the surface roughness values (ϵ) of individual pipes. Then, site measurements are used to calculate the friction coefficient of the system. This coefficient is compared with the surface roughness values (ϵ) of the numerical model to estimate how a calcinated pipe surface behaves for the heavily calcinated penstock so that the turbine operating range can be determined. Lastly, during the dismantling of the old turbines, the penstock is emptied and became accessible to receive samples from the penstock surface. Surface roughness of the sample is measured in the laboratory to confirm the friction slopes, apparent surface roughness values (ϵ), and measured roughness profiles that point to the same result.

2. NUMERICAL MODEL

A convenient form of the Energy Equation for a steady, incompressible flow with uniformly distributed velocity profiles can be written between the two sections in a straight pipe as:

$$\frac{P_1}{\rho g} + \frac{V_1^2}{2g} + Z_1 = \frac{P_2}{\rho g} + \frac{V_2^2}{2g} + Z_2 + H_L \quad (1)$$

where, P is the pressure, V is the average velocity, Z is the elevation of the pipe axis, ρ is the density of the fluid, g is the gravitational acceleration, and H_L is the frictional head loss between these two sections, given that there are no minor losses. In 1845, Julius Weisbach [4] proposed an equation that predicts the losses due to fluid friction on the pipe wall as;

$$H_L = f \frac{L V^2}{D 2g} \quad (2)$$

$$f = func \left(\frac{\varepsilon}{D}, Re \right) \quad (3)$$

where L is the pipe length, D is the pipe diameter, f is a friction factor, Re is the Reynolds number and is defined by $Re=VD/\nu$ and ν is the kinematic viscosity of the fluid. This equation set the standard for all following engineering text books [2]. With Darcy's estimates of the friction factor [5] and additional work by Colebrook and White [6] on non-uniform roughness, estimates of the friction factor f can be made as functions of Reynold number (Re) and relative roughness (ε/D). Later Moody [7] published the famous Moody's chart and Swamee and Jain [8] expanded the form to the explicit equations for pipe diameter, head loss and the discharge through a pipe, based on the Colebrook-White equation [6].

For long penstock systems, friction in each pipe segment can be calculated separately. Pipe diameters, lengths and corresponding Reynolds numbers are different in each pipe segment. Minor losses due to bends, expansions, contractions etc. can be calculated separately as a function of discharge and all of these losses can be added to obtain the system loss. In order to generalize the equation of losses, the Darcy-Weisbach equation can be written such that the head loss due to friction becomes a function of discharge:

$$H_L = (8fL/g\pi^2 D^5)Q^2 = k_{Friction}Q^2 \quad (4)$$

Minor (local) losses such as those due to bends, expansions contractions etc. can also be formulated as a function of discharge;

$$H_{Local} = k_{Local}Q^2 \quad (5)$$

Then the total loss in the system can be calculated by adding all friction and local losses.

$$H_{LossSystem} = \sum k_{Local}Q^2 + \sum k_{Friction}Q^2 = k_{Local}Q^2 + k_{Friction}Q^2 = kQ^2 \quad (6)$$

Where k is a combined friction coefficient for the entire system. A numerical one-dimensional model is designed for the existing system as shown in Figure 1, where the head

Roughness Coefficient of a Highly Calcinated Penstock

pond is modeled as reservoir 1 (R1). Water is conveyed through a concrete pipe (E1) and a series of steel pipes (P1-P9, B1, S1) to turbine and then to the Tailrace Channel (T1). The model is set up with one turbine in operation in order to compare the results with the measurements.

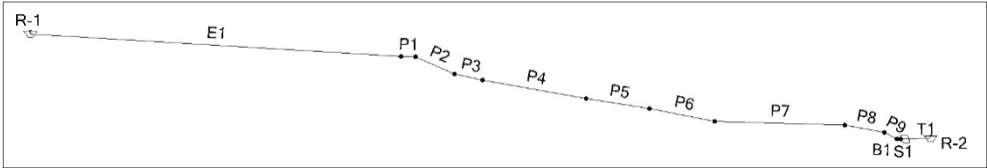


Figure 1 - Layout of the Kepez 1 HPP

Basic parameters including minor loss coefficients of the pipe system are given in Table 1.

Table 1 - System parameters

Label	Material	Diameter (cm)	Minor Loss Coefficient	Length (m)
P2	Steel	240	0.040	62.16
P4	Steel	240	0.000	164.60
P6	Steel	210	0.110	103.87
P3	Steel	240	0.006	44.33
P5	Steel	240	0.000	100.50
P1	Steel	240	0.062	23.01
T1	Concrete	500	0.000	5.00
P7	Steel	210	0.019	206.66
P8	Steel	210	0.060	62.88
E1	Concrete	250	0.346	589.00
B1	Steel	130	0.052	1.00
S1	Steel	90	0.169	3.60
P9	Steel	210	0.096	19.97

The head pond and tailrace levels are set to constant values for each simulation and the corresponding friction and minor losses are calculated. The discharge passing through the system is controlled by the guide vanes of the Francis turbine. The model is set such that the simulated discharge range covers the operation of the installed Francis turbine. A head discharge curve is used for each guide vane opening for the Francis Turbine. A total of 12 simulations are performed for three discharge sets (Table 2) and four roughness values (Table 3). Simulations are iterated until the discharge values are seen to converge with the preset values.

Table 2 - Simulated flowrates

	Q ₁ (m ³ /s)	Q ₂ (m ³ /s)	Q ₃ (m ³ /s)
Case	3.0344	5.3758	6.1471

Table 3 - Apparent surface roughness values

	ε ₁ (mm)	ε ₂ (mm)	ε ₃ (mm)	ε ₄ (mm)
Case	0.5	0.3	0.05	0.02

There are various engineering tables that present the apparent roughness values (ϵ) of different materials [2]. The values of interest in this study are for smooth and rough steel pipes (0.02 mm and 0.05 mm) and concrete (0.3~3 mm). A representative value of 0.5 mm is selected for smooth concrete. A comparative study is performed to observe how the roughness of calcinated surface changes with respect to steel and concrete. So, simulated values for the calcinated pipes included these values in addition to an intermediate value of 0.3mm. Since calcination occurs both in concrete and steel surfaces, roughness values are kept constant for all simulations throughout the system. During measurements, sensor taps were drilled on the steel pipe to install acoustic flow meters. The drilled hole and calcinated layer are shown in Figure 2. The thickness of the calcinated layers can be seen through these holes and found to vary between 11 mm and 15 mm. Although the effect of change in the flow diameter due to this accumulation is small, it is considered in all of the simulations and all pipe diameters presented in Table 1 is reduced by 30mm.



Figure 2 - Calcination in the pipe seen from a sensor tap

Friction and minor losses are calculated for each pipe segment and tabulated for each simulation. These values are summed up to calculate the total loss in each simulation. A sample computation for the flow rate of 6.147 m³/s, head pond elevation of 278.2 m, tailwater elevation of 110.04 m and an apparent roughness values (ϵ) of 0.3 mm is given in Table 4.

Table 4 - Solution values for a case

Label	Material	Velocity (m/s)	Headloss (m)	Headloss (Friction) (m)	Headloss (Minor) (m)
P2	Steel	1.39	0.038	0.034	0.004
P4	Steel	1.39	0.090	0.090	0.000
P6	Steel	1.77	0.123	0.105	0.018
P3	Steel	1.39	0.025	0.024	0.001
P5	Steel	1.39	0.055	0.055	0.000
P1	Steel	1.39	0.019	0.013	0.006
T1	Concrete	0.31	0.000	0.000	0.000
P7	Steel	1.77	0.213	0.210	0.003
P8	Steel	1.77	0.073	0.064	0.010
E1	Concrete	1.28	0.289	0.260	0.029
B1	Steel	4.85	0.076	0.014	0.063
S1	Steel	9.77	1.122	0.301	0.821
P9	Steel	1.77	0.036	0.020	0.015
Sum			2.157	1.188	0.969

In order to calculate the combined system friction constant k for each apparent roughness value (ϵ), total head loss in each simulation is calculated and tabulated against flowrate and square of the flowrate. Results of all simulations are summarized in Table 5.

Table 5 - Head loss values in meters for 12 cases

	ϵ_1 (mm)	ϵ_2 (mm)	ϵ_3 (mm)	ϵ_4 (mm)
Q (m ³ /s)	0.5	0.3	0.05	0.02
6.1471	2.275	2.157	1.898	1.835
5.3758	1.742	1.653	1.459	1.413
3.0344	0.559	0.532	0.477	0.465

As the head loss changes linearly with Q^2 value according to Darcy-Weisbach equation, results are plotted and a line is fitted to obtain friction head loss slope coefficient as shown in Figure 3. Coefficient values of 0.0488, 0.0504, 0.0572 and 0.0603 are obtained for roughness values of 0.02 mm, 0.05mm, 0.3mm and 0.5mm respectively.

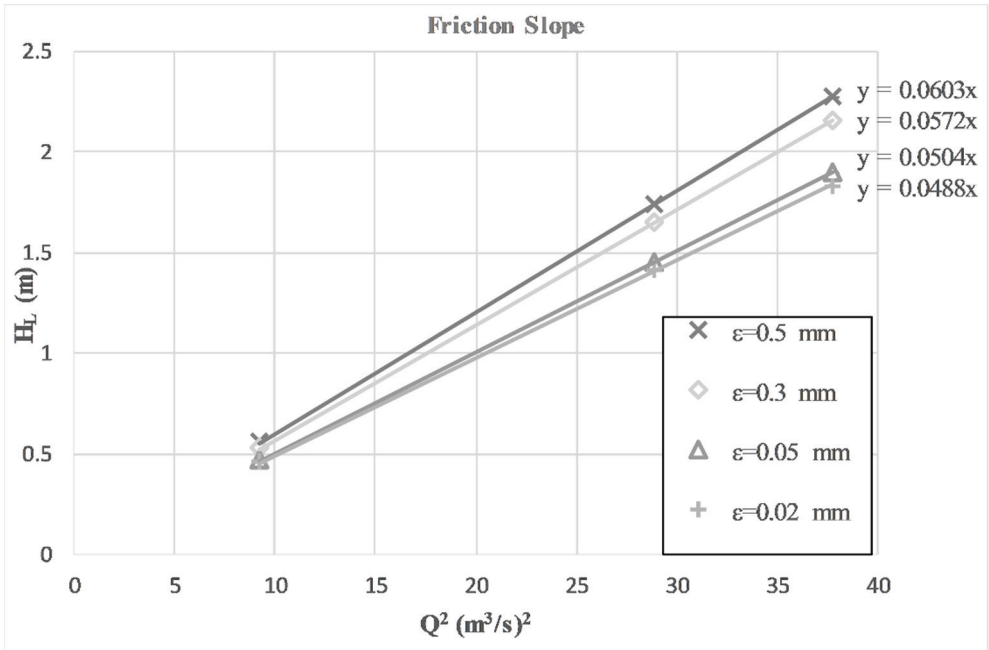


Figure 3 - Calculation of friction head loss slope for different roughness coefficients

3. CALCULATION OF FRICTION COEFFICIENT BASED ON SITE MEASUREMENT

Kepez HPP has been in operation for more than 30 years. During this period significant improvement in turbine design was achieved with the help of computational fluid dynamics (CFD)[9]. Efficiency and cavitation characteristics of runner is investigated and characteristics over operating region of the old Kepez turbine is determined by means of CFD [10][12]. Design of the new turbine is significantly improved to better characterize the current operating regime [13]. The new turbine efficiency is obtained by means of both CFD [13] and model tests [14] performed at ETU HYDRO Turbine Design and Test Center. Although these works give significant insight on the turbine performance, project requirements dictate comparison of efficiencies with in-situ site measurements. For this reason, an efficiency measurement setup is installed at site as part of the project[15]. Using this setup, hydraulic efficiency of the turbine is measured at different operating points [15]. Available hydraulic energy to the turbine and power output of the generator are required to calculate efficiency of the turbine generator set. To obtain the available hydraulic energy, the turbine net head and flowrate must be known. Pressure measurement taps are installed for measuring the inlet and outlet pressures before and after the turbine. An ultrasonic flow measurement system is installed for measuring the flow rate. For efficiency calculations, the mechanical power out of the turbine must also be determined. Power output of the generator can be measured through the current and voltage transformers. Energy analyzers were installed at outputs of generator current and voltage transformers to obtain the electrical output of the generator. With known generator efficiency curve and output of the generator, shaft power can be

Roughness Coefficient of a Highly Calcinated Penstock

calculated. So, hydraulic efficiency of the turbine can be calculated from available hydraulic energy and mechanical power. Using this methodology efficiency of the old turbine is measured [15]. Via these pressure taps and ultrasonic flow meters, the pressure at the turbine inlet as well as the discharge passing through the system is readily available and given in Table 6.

Table 6 - Flowrate, Pressure and Change in Head pond levels

Q [m ³ /s]	P (kPa)	ΔH_{HPL} (m)
6.1471	1619.67	0.65
6.0696	1619.90	0.77
5.7974	1622.51	0.77
5.6236	1626.25	0.20
5.5628	1626.44	0.69
5.3758	1627.50	0.77
5.1572	1629.19	0.12
4.8804	1630.61	0.00
4.2254	1636.40	0.65
3.0344	1642.69	0.74

Table 7 - System curve calculations

Q [m ³ /s]		$V^2/2g$ (m)	P/γ (m)	H_{inlet} (m)	$H_{inlet} - \Delta H_{HPL}$ (m)
6.1471		1.094	165.296	166.390	165.740
6.0696		1.067	165.319	166.386	165.616
5.7974		0.973	165.586	166.559	165.789
5.6236		0.916	165.967	166.883	166.683
5.5628		0.896	165.986	166.883	166.193
5.3758		0.837	166.095	166.932	166.162
5.1572		0.770	166.267	167.037	166.917
4.8804		0.690	166.412	167.101	167.101
4.2254		0.517	167.003	167.520	166.870
3.0344		0.267	167.645	167.911	167.171

This data set is used to calculate the head discharge relation of the system and the friction slope coefficient of the conduit. An additional data, head pond level, is required to calculate

a system curve. Since no digital measurement system for the head pond levels was available, hourly operating records of head pond level change with respect to crest elevation using a rod installed at the head pond is used. The change in the reservoir level is measured and tabulated below together with flowrate and pressure (Table 6).

System losses are calculated from the slope of the curve $H_{inlet} - \Delta H_{HPL}$ vs Q^2 . The corresponding values are obtained by adding the velocity head, pressure head and subtracting the variation in the head pond level as given in Table 7.

Results are plotted for total head vs square of flowrate and a line is fitted to obtain friction slope coefficient from measurements as shown in Figure 4. As the head loss changes linearly with Q^2 value according to Darcy-Weisbach equation, a line is fitted and slope is calculated as -0.0562 (Figure 4).

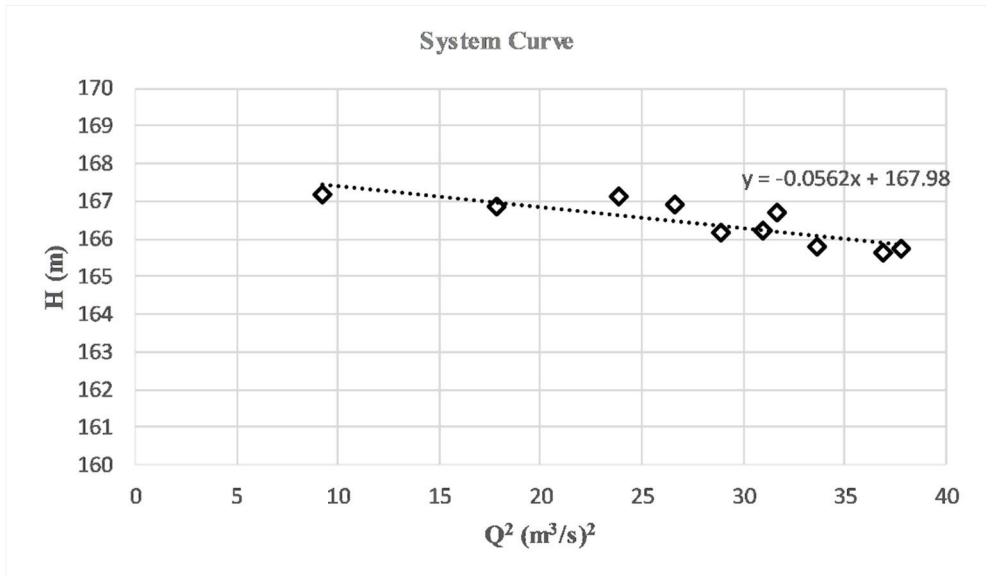


Figure 4 - Calculation of friction slope from measurements

The curve represents the change in the total head with increasing discharge, thus a negative value. Absolute value of this slope is 0.0562 which is compared with the various roughness values calculated and plotted via the numerical model, the surface roughness value (ϵ), 0.3mm shows a similar a slope of 0.0572.

4. LABORATORY MEASUREMENTS OF SURFACE ROUGHNESS

Once the design and manufacturing of the new turbine was completed, dismantling of the old turbine system was started. Energy production interrupted, the penstock was emptied. The old turbine system as well as the inlet valve was removed. At that stage, access to the penstock was available. A sample block of calcinated residue is carefully taken for testing purposes

Roughness Coefficient of a Highly Calcinated Penstock

without disturbing the surface, size and thickness of the calcinated sample taken from the penstock are shown in Figure 5.



Figure 5 - Calcinated sample from penstock

Sides of the block are grinded and the block is attached to a clamp. A Zeiss Surfcom 130 A surface profiler is used to measure the surface profile of the block.

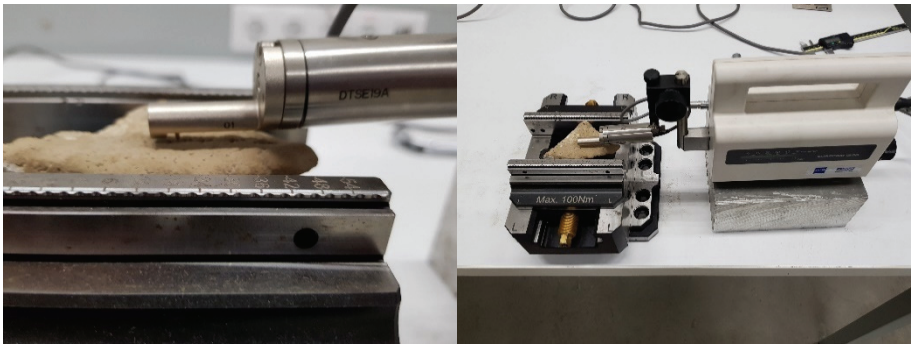


Figure 5 - Measurement of Surface profile

A sampling section is measured with a length of 38 mm. A probe with a tip radius of $2\ \mu\text{m}$, a speed of 0.6mm/s is used. The primary (total) profile, which is the surface height measured throughout the sampling section, is measured and shown in Figure 6. The waviness component is obtained from an electronic low-pass filtering of the primary profile with a cut off wavelength value of $8.0\ \text{mm}$ (Figure 6). Finally, roughness profile is obtained (Figure 7). By doing so, the measured profile is filtered for large scale waviness effects and a representative data set for the surface characteristics that effect friction is obtained. This data set is necessary to calculate measurable surface roughness characteristics R_a , R_q and R_z .

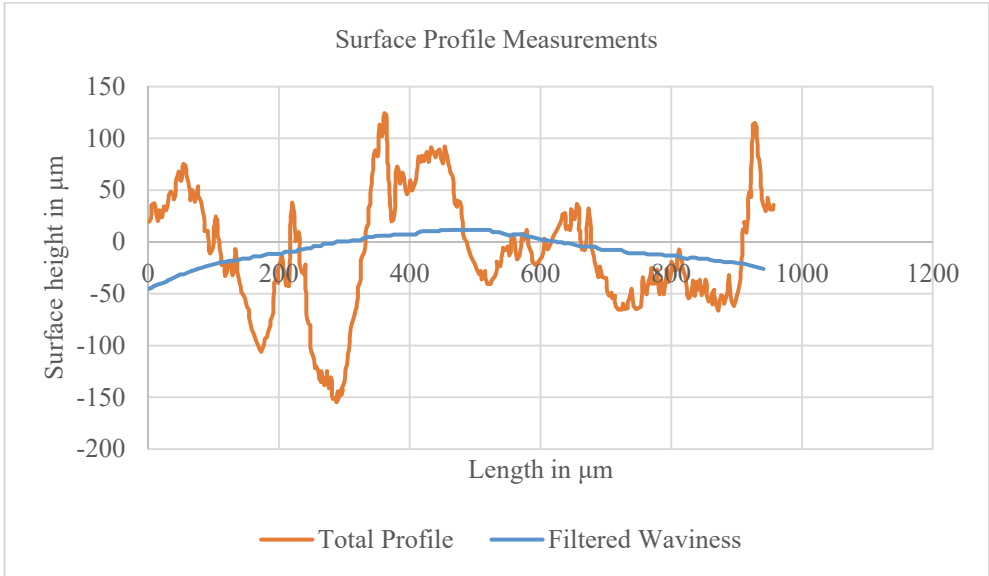


Figure 6 - Total profile and waviness

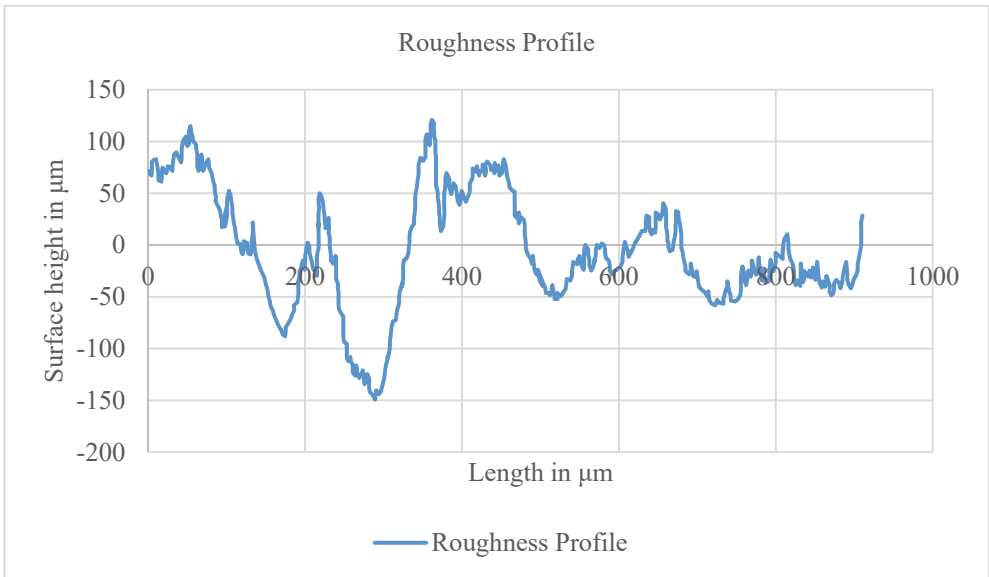


Figure 7 - Roughness profile

Once the roughness profile is obtained, standard surface roughness parameters (R_a , R_q , R_z) are calculated using equations 7, 8 and 9. The first parameter R_a represents the arithmetical

Roughness Coefficient of a Highly Calcinated Penstock

mean of the absolute values of the profile deviations from the mean line of the roughness and is given by:

$$Ra = \frac{1}{L} \int_0^L |z(x)| dx \quad (7)$$

whereas the root mean square roughness Rq is given by:

$$Rq = \sqrt{\frac{1}{L} \int_0^L z^2(x) dx} \quad (8)$$

The last parameter Rz is called ten-point height roughness which gives the average absolute value of five highest peaks and five lowest valleys over the evaluation length.

$$Rz = \sum_{i=1}^5 \frac{z_{max(i)} - z_{min(i)}}{5} \quad (9)$$

These three measured parameters are the parameters that are commonly used to describe the surface finish of materials. The calculated values for each of these parameters are given in Table 8.

Table 8 - Surface roughness parameters

Ra (μm)	Rq (μm)	Rz (μm)
47.20	59.46	287.45

The surface roughness value (ϵ) is not directly measurable. The friction factor given by Moody's chart derived from the friction coefficient of various fluid experiments conducted originally by Nikuradse by the evaluation of loss terms and equivalent sand roughness. There are numerous studies that relate the directly measurable quantities Ra, Rq and Rz to the surface roughness values (ϵ) used to calculate the friction factor f in Darcy-Weisbach equation.

Computational models that utilize surface roughness values (ϵ) for pipes, pumps and turbines simulate roughness data acquired from experiments that include many different roughness characterizations. On the other hand, manufacturers use directly measurable quantities Ra, Rq and Rz to represent the surface texture of their products. Equations available in literature [16- 31] that try to relate these parameters vary greatly and there is no consensus on a single relation on these parameters. Equations proposed by [19-24] mostly use sand grains, emery papers or machined surfaces to produce the empirical equations using Ra, while suggested equations for groove height or liquid crystal surfaces, Rq [26-27] is mostly used for surfaces with sprayed particles as an alternative.

Naturally occurring calcination deposits were not studied in any of these works; however, for a wide range of surfaces, a general trend is to use Rz, peak to valley roughness height, equal to surface roughness value (ϵ) ($Rz \approx \epsilon$) [16][17]. This corresponds to 287.45 μm for the

calcinated surface sample. Regardless, a table is prepared from available literature to calculate and check surface roughness values (ϵ) using all three parameters Ra, Rq, Rz. Values of surface roughness (ϵ) are calculated using these three parameters as given in Table 9 [16-31].

These values are averaged to find a single representative number for ϵ which is found to be 281.70 μm . The calculated average surface roughness (ϵ) value of 281.70 μm is also found to be very close to simulated 300 μm roughness value which corresponds to combined friction coefficient of 0.0572 for the system.

Table 9 - Calculated values of surface roughness (ϵ) in μm

Reference	Equation proposed	ϵ (calculated)
[18]	$\epsilon=Rz/5$	57.49
[18]	$\epsilon=Rz/2.56$	112.29
[19]	$\epsilon=2Ra$	94.40
[19]	$\epsilon=7Ra$	330.41
[20]	$\epsilon=6Ra$	283.21
[21]	$\epsilon=2.2Ra^{0.88}$	65.39
[22]	$\epsilon=8.9Ra$	420.09
[23]	$\epsilon=2Ra$	94.40
[24]	$\epsilon=16Ra$	755.22
[16]	$\epsilon=Rz$	287.45
[17]	$\epsilon=Rz$	287.45
[25]	$\epsilon=4Ra$	188.80
[26]	$\epsilon=2.1Rq$	124.87
[27]	$\epsilon=4.8Rq$	285.41
[28]	$\epsilon=10Ra$	472.01
[29]	$\epsilon=8.9Ra$	420.09
[30]	$\epsilon=1.9Rz$	546.16
[31]	$\epsilon=5.2Ra$	245.45
	Average	281.70

5. CONCLUSIONS

For turbine rehabilitation, roughness of old penstocks must be known in order to calculate head-discharge characteristics of the system. The case of interest is the roughness of highly calcinated pipeline system for which no prior information is available in the literature. A multimethodology is proposed to obtain apparent surface roughness coefficient (ϵ) of

calcinated pipes. For this reason, a one-dimensional numerical model of the existing system is built to calculate the steady state head and discharge relation by varying apparent surface roughness values. A set of curves are obtained for the system to specify the relation between friction coefficient and apparent surface roughness. Friction coefficient is also calculated based on site measurements of flow rate, head pond level and inlet pressure of turbines. The measured friction slope is compared with the slopes obtained from the numerical model. The closest match points to a roughness value of 0.3 mm for calcinated surfaces. Lastly, a sample calcinated block is obtained from site to measure surface roughness parameters at the laboratory. Measurable surface roughness parameters of arithmetic mean deviation of the roughness profile (Ra), root mean square roughness (Rq) and peak and valley roughness (Rz) are obtained. Empirical equations available in literature that relate these parameters to apparent surface roughness (ε) are used to find an average roughness value of 0.282 mm for the sample. It is determined that, for all practical purposes, a surface roughness value of 0.3 mm can be used for calcinated surfaces which is much higher than steel surfaces but smaller than concrete.

Surface roughness values of both steel and concrete is widely used in both the theoretical studies in literature and practical applications. However, the obtained value for the surface roughness of calcinated pipes based on site measurements, laboratory experiments and the numerical study presented here, is different than the values of both of these materials. This study clearly shows that the surface roughness of the calcinated pipe is 0.3 and the design process for rehabilitation and output of turbines and related equipment is affected drastically, if the change in surface roughness is not considered where calcination is present. Therefore, utilization of the methodology presented here, would provide the hydraulic power equipment designer the information necessary for rehabilitation works.

Symbols

D	Diameter of the pipe segment
f	Darcy - Weisbach friction factor
H_L	Head loss
k	Combined friction coefficient
k_{Friction}	Friction coefficient caused by friction losses in the pipe
k_{Local}	Friction coefficient caused by local losses
L	Length of the pipe segment
P	Pressure
Ra	Arithmetic mean deviation of roughness height
Re	Reynolds number
Rq	Root mean square roughness height
Rz	10 point roughness height (peak and valley roughness height)

V	Average velocity in pipe
Z	Elevation head
g	Gravitational acceleration
z	Height of each measured surface
ΔH_{HPL}	Deviation in elevation of the head pond level
ε	Apparent surface roughness
ρ	Density of water

Acknowledgement

This study is financially supported by TÜBİTAK under grant 113G109.

References

- [1] Kumar, R., Singal, S.K., Penstock material selection in small hydropower plants using MADM methods, *Renewable and Sustainable Energy Reviews*, 52(C), 240-255, 2015.
- [2] Munson, B. R., Young, D. F., & Okiishi, T. H.. *Fundamentals of fluid mechanics*. Hoboken, NJ: J. Wiley & Sons., 2006
- [3] Gilley, J. E., Kottwitz, E. R., Wieman, G. A., *Roughness Coefficients for Selected Residue Materials*, *J. Irrig. Drain. Eng.*, 117, 503–514., 1991
- [4] Weisbach, J., *Lehrbuch der Ingenieur- und Maschinen-Mechanik*, Vol. 1. Theoretische Mechanik, Vieweg und Sohn, Braunschweig., 1845.
- [5] Darcy, H. *Recherches expérimentales relatives au mouvement de l'eau dans les tuyaux*, Mallet-Bachelier, Paris. 268 pages and atlas, 1857
- [6] Colebrook, C. F. and White, C. M., *Experiments with fluid- friction in roughened pipes.*, *Proc. Royal Soc. London*, 161, 367-381, 1937.
- [7] Moody, L. F., *Friction factors for pipe flow*. *Trans. ASME*, 66,671-678, 1944.
- [8] Swamee, P. K., and Jain, A. K., *Explicit equations for pipe-flow problems.*, *J. Hydraulics Division*, ASCE, 102(5), 657-664, 1976.
- [9] Drtina P and Sallaberger M, *Hydraulic turbines—basic principles and state-of-the-art computational fluid dynamics applications*, *Proceedings of the Institution of Mechanical Engineers*, Part C: *Journal of Mechanical Engineering Science*, 213(1), 85 – 102, 1999
- [10] Celebioglu K, Altintas B, Aradag S, Tascioglu Y, *Numerical research of cavitation on Francis turbine runners*, *International Journal of Hydrogen Energy* 42(28), 17771-17781, 2017
- [11] Ayancik F, Acar E, Celebioglu K, Aradag S, *Simulation-based design and optimization of Francis turbine runners by using multiple types of metamodels*, *Proceedings of the*

- Institution of Mechanical Engineers, Part C: Journal of Mechanical Engineering Science, 231 (8), 1427-1444, 2017
- [12] Ayli E, Celebioglu K, Aradag S, Computational Fluid dynamics based hill chart construction and similarity study of prototype and model francis turbines for experimental tests 12th International Conference on Heat Transfer, Fluid Mechanics and Thermodynamics, Costa de Sol, 2016
- [13] Celebioglu K, Aradag S, Ayli E, Altintas B, Rehabilitation of Francis Turbines of Power Plants with Computational Methods, Hittite Journal of Science & Engineering 5 (1), 37-48, 2018
- [14] Kavurmaci B, Celebioglu K, Aradag S, Tascioglu Y, Model Testing of Francis-Type Hydraulic Turbines, Measurement and Control 50 (3), 70-73, 2017
- [15] TUBİTAK MAM Enerji Enstitüsü, “MİLHES Türbin Verim Ölçüm Raporu”, MLS.İP11.D.80.3009.V30, Elektrik Üretim Anonim Şirketi (EÜAŞ), 2018.
- [16] Hoffs, A., Drost, U., and Boics, A., “Heat Transfer Measurements on a Turbine Airfoil at Various Reynolds Numbers and Turbulence Intensities Including Effects of Surface Roughness,” International Gas Turbine and Aeroengine Congress & Exhibition, ASME Paper No. 96-GT-169, 1996.
- [17] Guo, S. M., Jones, T. V., Lock, G. D., and Dancer, S. N., Computational Prediction of Heat Transfer to Gas Turbine Nozzle Guide Vanes With Roughened Surfaces, Journal of Turbomachinery, 120, 343-350, 1998
- [18] Speidel, L., Determination of the Necessary Surface Quality and possible Losses due to Roughness in Steam Turbines, Elektrizitätswirtschaft, 1(21), 799-804, 1962
- [19] Forster, V.T., Performance Loss of Modern Steam Turbine Plant due to Surface Roughness, Proc. Instrn. Mech Engrs, 181(1), 391-405. 1967
- [20] Koch, C. C., Smith, L. H. Jr., Loss Sources and Magnitudes in Axial-Flow Compressors, Journal of Engineering for Power, 98(3), 411-424, 1976
- [21] Bammert, K., and Sandstede, H., Influences of Manufacturing Tolerances and Surface Roughness of Blades on the Performance of Turbines, Journal of Engineering Power, 98(1), 29-36, 1976
- [22] Schäffler, A., Experimental and Analytical Investigation of the Effects of Reynolds Number and Blade Surface Roughness on Multistage Axial Flow Compressors, Journal of Engineering for Power, 102, 5-13, 1980
- [23] Simon, H., Bülskämper, A., On the Evaluation of Reynolds Number and Relative Surface Roughness Effects on Centrifugal Compressor Performance Based on Systematic Experimental Investigations, Journal of Engineering for Gas Turbines and Power, 106, 489-501, 1984
- [24] Barlow, D.N. and Kim, Y.W., Effect of Surface Roughness on Local Heat Transfer and Film Cooling Effectiveness, ASME International Gas Turbine Exposition, Houston, Texas, ASME paper #95-GT-14. 1995

- [25] Bogard, D.G., Schmidt, D.L., and Tabbita, M., Characterization and Laboratory Simulation of Turbine Airfoil Surface Roughness and Associated Heat Transfer, *Journal of Turbomachinery*, 120(2), 337-342, 1998
- [26] Boyle, R. J., Spuckler, C. M., Lucci, B. L., and Camperchioli, W. P., Infrared Low-Temperature Turbine Vane Rough Surface Heat Transfer Measurements, *Journal of Turbomachinery*, 123, 168-177, 2001
- [27] Boyle, R. J., and Senyitko, R. G., Measurements and Predictions of Surface Roughness Effects on Turbine Vane Aerodynamics, *Proceedings of ASME TURBO EXPO 2003*, GT2003-38580, 2003.
- [28] Bunker, R. S., The Effects of Thermal Barrier Coating Roughness Magnitude on Heat Transfer With and Without Flowpath Surface Steps, *Proceedings of IMECE 2003 ASME International Mechanical Engineering Congress & Exposition*, IMECE2003-41073, 2003.
- [29] Shabbir, A., Turner, M. G., A Wall Function for Calculating the Skin Friction with Surface Roughness, *Proceedings of ASME Turbo Expo 2004*, GT2004-53908, 2004.
- [30] Zhang, Q., and Ligrani, P. M., Aerodynamic Losses of a Cambered Turbine Vane: Influences of Surface Roughness and Freestream Turbulence Intensity, *Journal of Turbomachinery*, 128, 536-546, 2006
- [31] Hummel, F., Lotzerich, M., Cardamone, P., Fottner, L., Surface Roughness Effects on Turbine Blade Aerodynamics, *Proceedings of ASME Turbo Expo 2004 Power for Land, Sea, and Air*, GT2004-53314, 2004

Efficient Dynamic Analysis of Foundation via a Coupled Axisymmetric SBFEM-3D FEM

Mojtaba ASLMAND¹
Iradj Mahmoudzadeh KANI²
Mehmet Cemal GENES³

ABSTRACT

An axisymmetric scaled boundary finite element method for the elastodynamic analysis of 3D layered systems is derived in frequency domain. The general three-dimensional problem of unbounded domain can be divided into a number of independent two-dimensional problems and a pseudo three-dimensional analysis can be performed. The aforementioned analysis offers considerable savings in terms of storage and computation cost when compared with a full three-dimensional analysis. A new coupled strategy is proposed in order to match the axis-symmetrically modeled unbounded far field to a general 3D finite element model of the near field. The derived formulation is implemented for frequency domain analysis of foundation embedded in or resting on the surface of 3D layered homogenous or inhomogeneous soil deposits over rigid bedrock. The dynamic response calculated using the proposed method is compared with analytical or numerical solutions. Numerical examples demonstrate the accuracy and high efficiency of the new proposed method.

Keywords: Axisymmetric scaled boundary finite element method, layered soil, dynamic soil-structure interaction, Fourier series, dynamic stiffness.

1. INTRODUCTION

Dynamic response of heavy and embedded structures such as nuclear reactors, turbine towers and offshore wind plants, liquid-storage tanks and high-rise buildings are affected by the interaction between the structures and their foundations. These problems are known as soil-

Note:

- This paper has been received on July 25, 2018 and accepted for publication by the Editorial Board on November 12, 2018.
- Discussions on this paper will be accepted by September 30, 2019.
- <https://dx.doi.org/10.18400/tekderg.447721>

1 University of Tehran, School of Civil Engineering, Tehran, Iran - maslmand@ut.ac.ir - <https://orcid.org/0000-0003-1241-094X>

2 University of Tehran, School of Civil Engineering, Tehran, Iran - imkani@ut.ac.ir - <https://orcid.org/0000-0003-0124-7868>

3 Eastern Mediterranean University, Civil Engineering Department, Famagusta, North Cyprus - cemal.genes@emu.edu.tr - <https://orcid.org/0000-0002-9052-7361>

structure interaction (SSI) problems. The main goal of many related engineering studies is to develop SSI models, which are reliable and easy to implement.

One of the major challenges in this area is the lack of a precise and consistent template to model radiation damping of the unbounded soil domain. Consequently, the conventional finite element method is not directly applicable, since outgoing waves are reflected at the artificial boundaries of the finite element mesh. Over the past five decades, various approaches have been introduced in order to overcome this problem [1-6].

Most of the common approaches to model dynamic soil-structure interaction problems in layered media can be classified as the boundary element method [7-9], the thin layer method (TLM) [10-15] or approximate methods based on physical models [16-22] and semi-analytical methods [23, 24].

The boundary element method is a popular tool for the solution of dynamic problems in unbounded domains since it is based on the use of fundamental solutions, which satisfies the radiation condition explicitly. Green's functions for layered media are complex and computationally expensive [25-27].

A widely used method for dynamic analysis of layered media is the thin-layer method which has mainly been applied to plane and cylindrical problems [28]. It is a semi-analytical approach based on the coupling of an axisymmetric finite element formulation with an analytical solution in the wave number and frequency-domain in the direction of wave propagation. The latter is obtained by discretization in the direction of layering.

Interesting from a practical point of view, simplified or physical models lead to approximate solutions. Cone models [29] have been introduced for the analysis of rigid foundations by one-dimensional wave propagation formulation in the frequency-domain. Semi-analytical solutions are based on a discretization of the footing-subsoil interface and the element-wise use of Green's functions [24,30].

A relatively recent semi-analytical approach, which shows certain parallels to the thin-layer method, is the scaled boundary finite element method (SBFEM) [31]. It is particularly suitable for the analysis of dynamic problems in unbounded domains. The SBFEM combines some important advantages of the finite element method (FEM) and the boundary element method (BEM). When this method is applied, the spatial dimension of the problem is reduced by one eliminating the need for fundamental solution. The material anisotropy only affects the constitutive matrix and is implemented straightforwardly. A SBFE model of an unbounded domain can be coupled seamlessly with a finite element model of the near-field. The combined formulation has been used for dynamic 2D and 3D SSI problems in both the frequency domain and time domain [32-37].

The original SBFEM [31] is based on the use of a scaling centre, somehow the reference point for assessing the visibility of the complete boundary. It defines a transformation of the geometry such that the problem can be solved numerically in the circumferential directions and analytically in the radial direction. It can be used for the description of 2D or 3D half-space or full-space unbounded domains.

A modified version of the SBFEM for two-dimensional domains with parallel boundaries [38], for three-dimensional prismatic domains [39] and for axisymmetric domain [40] exists. All three versions of the SBFEM, however, are not used to model a truly three-dimensional

layered system. Recently, a Modified SBFEM for the analysis of dynamic problems in three-dimensional layered continua is derived [28]. The latter is based on the use of a scaling line, rather than a scaling centre and it fully couples the 3D FEM with 2D SBFEM. In order to reduce the computational cost and accuracy of the solution, the formulation has been modified to an axisymmetric SBFEM, in which only a line discretization is needed and the solution could be obtained for each term of the Fourier series separately [41].

The recently derived formulation by Aslmand et al. [41] for coupling a semi-analytical axisymmetric far field formulation and a 3D finite element model is available. The coupling is done by the aid of Fourier coefficients and the time domain developments were achieved by FFT. The proposed novel SBFEM for 3D layered media is considerably different from the original SBFEM. In combination with a finite element model of the near field, it can be used efficiently for the dynamic analysis of flexible three-dimensional foundations of arbitrary shape embedded in or resting on the surface of layered soil deposits over rigid bedrock.

The radiation condition states that there are not any incoming waves. For special cases the radiation requirement can be expressed as a local formulation, such as Sommerfeld radiation condition [42] for the Helmholtz's equation in infinite homogeneous domains. Generalized radiation conditions involve elastodynamic Green's functions for the semi-infinite solid and for the layered half-space which have been established in studies of Guzina et al. [43] and Madyarov and Guzina [44]. Nevertheless, in this study, the radiation condition at infinity is satisfied automatically by using the SBFEM [31, 45] to model the far field with axisymmetric formulation.

This paper focuses on frequency domain examples by coupling between axisymmetric SBFEM and 3D FEM. The further outline of this paper is as follows. In the first section, the assumptions in this paper to analyze three-dimensional foundation-soil systems are summarized. Then, the formulation of axisymmetric SBFEM for unbounded layered media is summarized. The coupling to a 3D finite element model of the near field is addressed in the next section, and finally frequency domain analysis of various layered soil-foundation systems are held for verification and present the efficiency of the newly developed coupling method.

2. PROBLEM DEFINITION

The substructure method has been used for the analysis of structures with flexible foundations embedded in a layered soil (Figure 1). The material properties of layer j which is unbounded in horizontal direction has been defined as shear modulus (G_j), Poisson's ratio (ν_j), mass density (ρ_j) and thickness (d_j) and a constant damping ratio D for all layers.

In order to have an axisymmetric geometry for the interface of near field/far field, the near field shall be defined by a cylinder containing the arbitrary shaped foundation and a certain part of the irregular soil. Within this context, the near field/far field interface is denoted as S as depicted in Figure 1. For modeling of the near field, traditional 3D FEM technique is adopted. On the other hand, the far field is analyzed through utilization of an axisymmetric SBFEM where this approach has been previously implemented and validated in the study conducted by Aslmand et al. [41]. In the next section, executed axisymmetric SBFEM analysis is summarized.

It is assumed that dynamic loads are concentrated either in the near field or on the structure system only and hence outwardly propagating waves including surface and interfacial waves are generated.

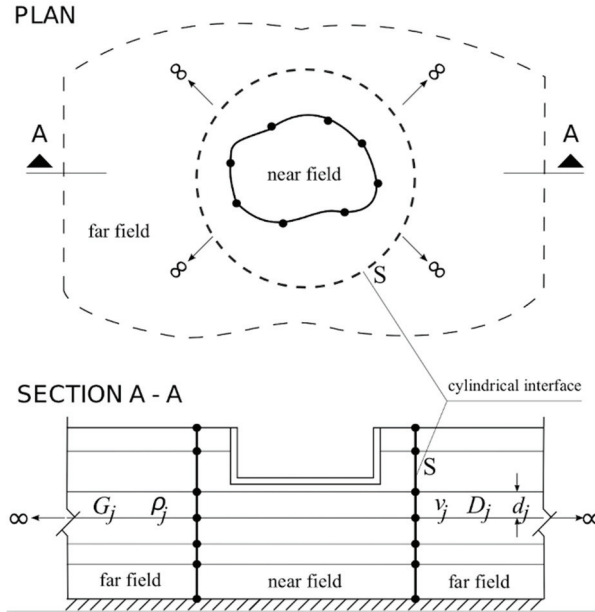


Figure 1 - 3D soil-structure system with foundation embedded in layered soil deposit resting on rigid bedrock

2.1. Axisymmetric Scaled Boundary Finite Element Method

2.1.1. Scaled Boundary Transformation of the Geometry

The modified SBFEM uses a coordinate system, which scales a defining curve S relative to a scaling line. As shown in Figure 2, in axisymmetric SBFEM the scaling line is identical to the axis of symmetry (the \hat{z} -axis). The radial direction ξ is described by a series of parallel rays, which are perpendicular to the scaling line. Radial coordinate ξ is equal to 0 and 1 at the intersection with the \hat{z} -axis and the line S , respectively. But also, ξ could be considered greater than 1 ($0 \leq \xi < \infty$).

Due to consideration of axisymmetric geometry, using the advantage of cylindrical coordinates (r, z, θ) in the far field is more convenient (Figure 2).

The governing equation for the linear elastodynamics in cylindrical coordinate state,

$$\bar{L}^T \sigma + \omega^2 \rho u = 0 \tag{1}$$

where σ, \mathbf{u} and $\bar{\mathbf{L}}$ are stresses, displacements and the equilibrium operator in cylindrical coordinate, respectively. Assuming linear elasticity, the stress-strain relationship can be expressed according to Hooks' law

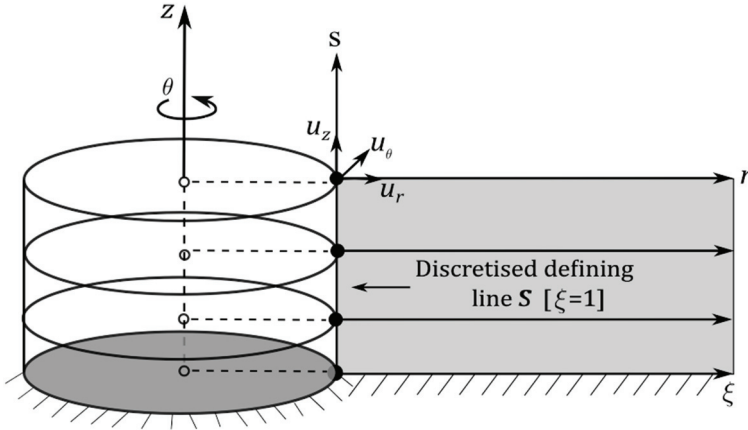


Figure 2 - Definition of SBFEM local coordinates for an axisymmetric unbounded domain

$$\sigma = \mathbf{D}\varepsilon \tag{2}$$

where, \mathbf{D} is constitutive matrix and

$$\varepsilon = \mathbf{L}u \tag{3}$$

where \mathbf{L} is a differential operator in cylindrical coordinate [41]. The approximate solution of Eq. (1) is obtained using a Fourier series in the circumferential θ direction and using conventional one-dimensional finite-element shape functions along the boundary S which leads to a series of ordinary differential equations in terms of the radial coordinate ξ [41]. Hence, a solution is written in the form

$$\begin{Bmatrix} u_r(\xi, s, \theta) \\ u_z(\xi, s, \theta) \\ u_\theta(\xi, s, \theta) \end{Bmatrix} = \sum_{n=0}^{\infty} \{ \mathbf{F}_u^s(\theta, n) \mathbf{N}(s) \mathbf{u}^s(\xi, n) + \mathbf{F}_u^a(\theta, n) \mathbf{N}(s) \mathbf{u}^a(\xi, n) \} \tag{4}$$

where,

$$\mathbf{F}_u^s(\theta, n) = \begin{bmatrix} \cos n\theta & 0 & 0 \\ 0 & \cos n\theta & 0 \\ 0 & 0 & -\sin n\theta \end{bmatrix}, \quad \mathbf{F}_u^a(\theta, n) = \begin{bmatrix} \sin n\theta & 0 & 0 \\ 0 & \sin n\theta & 0 \\ 0 & 0 & \cos n\theta \end{bmatrix} \tag{5}$$

$\mathbf{N}(s)$ is the shape functions matrix corresponding to the discretization of s , and $\mathbf{u}^s(\xi, n)$ and $\mathbf{u}^a(\xi, n)$ represent the variation of the nodal displacement in the ξ direction for the symmetric and anti-symmetric Fourier terms, respectively.

Mapping to the scaled boundary co-ordinate system, the linear operator \mathbf{L} can be expressed as

$$\mathbf{L} = \mathbf{b}^1(s) \frac{\partial}{\partial r} + \mathbf{b}^2(s) \frac{\partial}{\partial z} + \mathbf{b}^3(s) \frac{1}{r} + \mathbf{b}^4(s) \frac{1}{r} \frac{\partial}{\partial \theta} + \mathbf{b}^5(s) \frac{1}{r} \frac{\partial}{\partial \theta} \quad (6)$$

Where $\mathbf{b}^1(s)$ to $\mathbf{b}^5(s)$ are defined in [41].

Substituting Eqs. (4), (6) and (3) in Hooks' law (2), the stress can be expressed more clearly [41].

The virtual work principle for the dynamic case (in absence of body loads) reads

$$\int_V \delta \boldsymbol{\epsilon}(\xi, s, \theta)^T \boldsymbol{\sigma}(\xi, s, \theta) dV + \int_V \delta \mathbf{u}(\xi, s, \theta) \rho \ddot{\mathbf{u}}(\xi, s, \theta) dV - \int_S \int_0^{2\pi} \delta \mathbf{u}(s, \theta)^T \mathbf{t}(s, \theta) |J(s)| d\theta ds = 0 \quad (7)$$

The first term denotes the virtual work of internal strain energy. The second term is the virtual work of inertia forces and last but not least, the third term is the virtual work of external forces such as surface tractions $\mathbf{t}(s, \theta)$ acting on the discretized boundary (It is assumed that all of the surface tractions are in the near field). As aforementioned, the contribution of the three terms to the virtual work is already derived in the study of Aslmand et al. [41] to obtain the SBFEM equations in displacement for an unbounded layered axisymmetric medium as given in Eqs. (8)-(11). It is a must for these equations to satisfy each symmetric and anti-symmetric component of the Fourier series.

$$\mathbf{P}^s(n) = \mathbf{E}^{0s}(n) \mathbf{u}^s(n)_{,\xi} + (\mathbf{E}^{1s}(n)^T + \mathbf{E}^{3s}(n)) \mathbf{u}^s(n) \quad (8)$$

$$\begin{aligned} & \mathbf{E}^{0s}(n) \xi \mathbf{u}^s(\xi, n)_{,\xi\xi} + (\mathbf{E}^{0s}(n) - \mathbf{E}^{1s}(n) + \mathbf{E}^{1s}(n)^T + \xi \mathbf{E}^{3s}(n) - \xi \mathbf{E}^{3s}(n)^T) \mathbf{u}^s(\xi, n)_{,\xi} \\ & + \left(\frac{1}{\xi} \mathbf{E}^{2s}(n) + \mathbf{E}^{3s}(n) - \mathbf{E}^{4s}(n) - \mathbf{E}^{4s}(n)^T - \xi \mathbf{E}^{5s}(n) \right) \mathbf{u}^s(\xi, n) + \\ & \omega^2 \mathbf{M}_0^s(n) \xi \mathbf{u}^s(\xi, n) = 0 \end{aligned} \quad (9)$$

$$\mathbf{P}^a(n) = \mathbf{E}^{0a}(n) \mathbf{u}^a(n)_{,\xi} + (\mathbf{E}^{1a}(n)^T + \mathbf{E}^{3a}(n)) \mathbf{u}^a(n) \quad (10)$$

$$\begin{aligned} & \mathbf{E}^{0a}(n) \xi \mathbf{u}^a(\xi, n)_{,\xi\xi} + (\mathbf{E}^{0a}(n) - \mathbf{E}^{1a}(n) + \mathbf{E}^{1a}(n)^T + \xi \mathbf{E}^{3a}(n) - \xi \mathbf{E}^{3a}(n)^T) \mathbf{u}^a(\xi, n)_{,\xi} \\ & + \left(\frac{1}{\xi} \mathbf{E}^{2a}(n) + \mathbf{E}^{3a}(n) - \mathbf{E}^{4a}(n) - \mathbf{E}^{4a}(n)^T - \xi \mathbf{E}^{5a}(n) \right) \mathbf{u}^a(\xi, n) + \\ & \omega^2 \mathbf{M}_0^a(n) \xi \mathbf{u}^a(\xi, n) = 0 \end{aligned} \quad (11)$$

The solution of Eqs. (9) and (11) must be sought for each term of the Fourier Series independently. Eqs. (9) and (11) are the *scaled boundary finite element equation* in

displacement for each term of Fourier series in an unbounded layered system. A particular solution for $u(\xi, n)$ is less interesting compared to a general solution for the dynamic stiffness matrix which relates the amplitude of coupling forces to the amplitudes of coupling.

The significance of this is that the system of equations decouples into pairs of equations for each symmetric and anti-symmetric term in the Fourier series representing the applied loading and displacement. Should a particular Fourier term in the loading series be zero, the corresponding term in the displacement series will also be zero. Thus, if the loading series only contains a single Fourier term, only a single set of equations need to be solved. Should the loading series contain more than one term, the set of equations for each term can be solved independently, and the resulting displacements and stresses superposed [40].

With the intention of obtaining equations in dynamic stiffness, the linear second-order differential Eqs. (9) and (11) in displacement are transformed into equivalent nonlinear first-order differential equations as in Ref. [28], Eq. (60). After the derivation, Equations for the dynamic stiffness matrix of unbounded medium is obtained,

$$\begin{aligned} & (\mathbf{S}^s(\omega, \xi, n) + \mathbf{E}^{1s}(n) + \xi \mathbf{E}^{3s}(n)^T) \mathbf{E}^{0s}(n)^{-1} (\mathbf{S}^s(\omega, \xi, n) + \mathbf{E}^{1s}(n)^T + \xi \mathbf{E}^{3s}(n)) \\ & - \xi \mathbf{S}^s(\omega, \xi, n)_{,\xi} - \xi (\mathbf{E}^{4s}(n) + \mathbf{E}^{4s}(n)^T) - \xi^2 \mathbf{E}^{5s}(n) + \omega^2 \xi^2 \mathbf{M}^{0s}(n) = 0 \end{aligned} \quad (12)$$

$$\begin{aligned} & (\mathbf{S}^a(\omega, \xi, n) + \mathbf{E}^{1a}(n) + \xi \mathbf{E}^{3a}(n)^T) \mathbf{E}^{0a}(n)^{-1} (\mathbf{S}^a(\omega, \xi, n) + \mathbf{E}^{1a}(n)^T + \xi \mathbf{E}^{3a}(n)) \\ & - \xi \mathbf{S}^a(\omega, \xi, n)_{,\xi} - \xi (\mathbf{E}^{4a}(n) + \mathbf{E}^{4a}(n)^T) - \xi^2 \mathbf{E}^{5a}(n) + \omega^2 \xi^2 \mathbf{M}^{0a}(n) = 0 \end{aligned} \quad (13)$$

Eqs. (12) and (13) are the *scaled boundary finite element equations in dynamic stiffness* for an unbounded axisymmetric layered medium.

The nonlinear first-order differential equation with respect to ξ is solved numerically using a Runge-Kutta scheme for a given frequency ω^* instead. An initial value is required to start the numerical integration scheme. It is calculated in the following using an asymptotic expansion of the dynamic stiffness $\mathbf{S}^\infty(\omega^*, \xi)$ with respect to the radial coordinate ξ .

2.1.2. Asymptotic Expansion of Dynamic Stiffness in ξ

The unknown dynamic stiffness matrix $\mathbf{S}^\infty(\xi, n)$ for both symmetric and anti-symmetric is expressed as a power series in (ξ) with decreasing exponent. In the following the superscript s and a and the series number n has been omitted for convenience

$$\mathbf{S}^\infty(\xi) \approx (\xi)^1 \mathbf{C}_\infty + (\xi)^0 \mathbf{K}_\infty + \sum_{j=1}^m \frac{1}{(\xi)^j} \mathbf{A}_j \quad (14)$$

The eigenvalue problem

$$\mathbf{M}^0 \Phi = \mathbf{E}^0 \Phi \mathbf{m}^0, \quad \Phi^T \mathbf{E}^0 \Phi = \mathbf{I}, \quad \Phi^T \mathbf{M}^0 \Phi = \mathbf{m}^0 \quad (15)$$

is used to transform Eqs. (12) and (14) into

$$\begin{aligned} & \left(\mathbf{s}^\infty(\xi) + \mathbf{e}^1 + \xi \mathbf{e}^{3T} \right) \left(\mathbf{s}^\infty(\xi) + \mathbf{e}^{1T} + \xi \mathbf{e}^3 \right) - \xi \mathbf{s}^\infty(\xi)_{,\xi} - \mathbf{e}^2 - \xi \left(\mathbf{e}^4 + \mathbf{e}^{4T} \right) \\ & - \xi^2 \mathbf{e}^5 + \omega^2 \xi^2 \mathbf{m}^0 = 0 \end{aligned} \quad (16)$$

With

$$\mathbf{s}^\infty(\xi) = \mathbf{\Phi}^T \mathbf{S}^\infty(\xi) \mathbf{\Phi}, \quad \mathbf{e}^j = \mathbf{\Phi}^T \mathbf{E}^j \mathbf{\Phi}, \quad j = 1, 2, \dots, 5 \quad (17)$$

Note that both \mathbf{M}^0 and \mathbf{E}^0 are positive definite values, thus all eigenvalues are real positive. Thus, Eq. (14) is transformed analogously,

$$\mathbf{s}^\infty(\xi) \approx (\xi)^1 \mathbf{c}_\infty + (\xi)^0 \mathbf{k}_\infty + \sum_{j=1}^m \frac{1}{(\xi)^j} \mathbf{a}_j \quad (18)$$

Where

$$\mathbf{c}_\infty = \mathbf{\Phi}^T \mathbf{C}_\infty \mathbf{\Phi}, \quad \mathbf{k}_\infty = \mathbf{\Phi}^T \mathbf{k}_\infty \mathbf{\Phi}, \quad \mathbf{a}_j = \mathbf{\Phi}^T \mathbf{A}_j \mathbf{\Phi} \quad (19)$$

The derivative with respect to $\mathbf{s}^\infty(\xi)_{,\xi}$ is expressed as

$$\mathbf{s}^\infty(\xi)_{,\xi} \approx \mathbf{c}_\infty - \sum_{j=1}^m \frac{j}{(\xi)^j} \mathbf{a}_j \quad (20)$$

The power series Eq. (18) and its derivative Eq. (20) are substituted in Eq. (16). The coefficients \mathbf{c}_∞ , \mathbf{k}_∞ and \mathbf{a}_j are calculated equating terms in the resulting formulation corresponding to decreasing powers of ξ to zero. The quadratic term yields

$$\mathbf{c}_\infty \mathbf{c}_\infty + \mathbf{e}^{3T} \mathbf{c}_\infty \mathbf{e}^3 + \mathbf{e}^{3T} \mathbf{e}^3 - \mathbf{e}^5 + \omega^2 \mathbf{m}^0 = 0 \quad (21)$$

Eq. (21) is an algebraic Riccati equation for the coefficient \mathbf{C}_∞ [46].

Its solution involves the Schur decomposition of an associated Hamiltonian matrix \mathbf{H} . The eigenvalues occur in pairs $\pm \boldsymbol{\lambda}$ where $\boldsymbol{\lambda}$ contains all eigenvalues with negative real part or positive imaginary part, if $\boldsymbol{\lambda}$ is purely imaginary. Complex eigenvalues with negative real parts correspond to modes which are decaying with $\xi \rightarrow \infty$ purely imaginary eigenvalues with positive imaginary part correspond to physically acceptable outwardly propagating modes. Only the Schur vectors associated with $\pm \boldsymbol{\lambda}$ are used to construct \mathbf{C}_∞ . In doing so, the radiation condition is taken into account.

The linear term yields

$$\begin{aligned} & (\mathbf{c}_\infty + \mathbf{e}^{3T}) \mathbf{k}_\infty + \mathbf{k}_\infty \mathbf{c}_\infty + \mathbf{e}^3 = -(\mathbf{c}_\infty + \mathbf{e}^{3T}) \mathbf{e}^{1T} - \mathbf{e}^1 (\mathbf{c}_\infty + \mathbf{e}^3) \\ & + \mathbf{c}_\infty + (\mathbf{e}^4 + \mathbf{e}^{4T}) \end{aligned} \quad (22)$$

Eq. (22) is a Lyapunov equation for the coefficient \mathbf{k}_∞ with a symmetric coefficient matrix \mathbf{c}_∞ . Its solution is computed using Schur decomposition and subsequently solving a Sylvester equation [47].

The constant term yields

$$(\mathbf{c}_\infty + \mathbf{e}^{3T})\mathbf{a}_1 + \mathbf{a}_1(\mathbf{c}_\infty + \mathbf{e}^3) = -(\mathbf{k}_\infty + \mathbf{e}^1)(\mathbf{k}_\infty + \mathbf{e}^{1T}) + \mathbf{e}^2 \quad (23)$$

Eq. (23) is again a Lyapunov equation for the coefficient \mathbf{a}_1 , which is solved analogously to Eq. (22).

Equations for higher order terms $\mathbf{a}_j, j>1$, can be derived in an analogous manner. The initial value of the dynamic stiffness is constructed evaluating Eq. (24) for a high but finite value ξ_h .

$$\mathbf{S}^\infty(\omega^*, \xi_h) \approx (\Phi^{-1})^T \xi_h \mathbf{C}_\infty + \mathbf{k}_\infty + \sum_{j=1}^m \frac{j}{(\xi_h)^j} \mathbf{a}_j \Phi^{-1} \quad (24)$$

In order to consider material damping in the formulation given above, Linear hysteretic material damping is incorporated to the proposed method by using a complex-valued shear modulus G^* instead of the real-valued quantity G ,

$$G^* = (1 + i2D)G \quad (25)$$

In Eq. (25) the symbols i and D denote the imaginary unit and the damping ratio, respectively.

3. COUPLING OF 3D FEM-AXISYMMETRIC SBFEM

The interior domain is modeled by using an ordinary 3D finite element approach. The coupling between the finite element model of the near field and the axisymmetric scaled boundary finite element model of the far field is not straightforward, provided that the 2D near field/ far field interface surface shall be presented by the 1D discretization of a line regarding axisymmetric SBFEM.

To couple axisymmetric and non-axisymmetric domains each mesh node in the circumference of the cylinder enclosing the near field (interface) should be considered to find the corresponding columns of the unbounded stiffness matrix. The r^{th} column of the unbounded stiffness matrix represents the nodal load vector to enforce a certain deformation configuration, where the r^{th} nodal dof is unity and the rest are zero. The stiffness matrix of the interface will be constructed from this concept. For instance, supposition a unit value of displacement in r direction of point i as is depicted in Figure 3(a), the variation of displacement around the circumferential line contain node i would be a linear function which has the value of unity at node i and zero elsewhere (Figure 3(b)). Note that the variation of displacement in z direction would be satisfied with the shape functions of linear elements on the line of discretization matching with the finite element ones (here the mesh is restricted to 8-node brick elements for the near field and linear elements for the far field). The Fourier series of the corresponding function named $u(\theta)$ is written as:

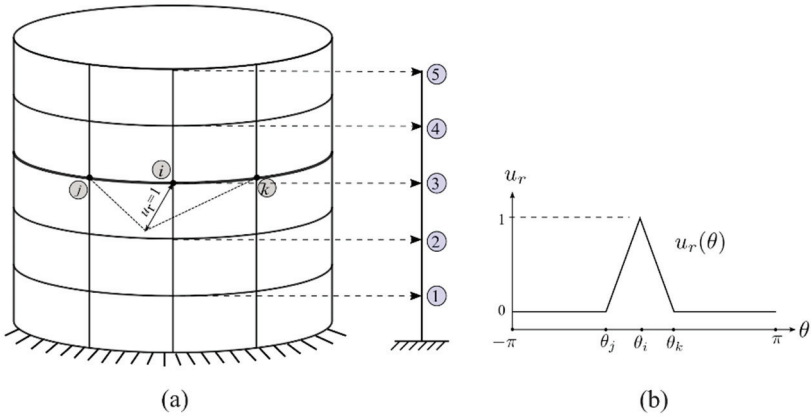


Figure 3 - (a) Interface of near field/far field (b) Linear variation of displacement around circumference due to the imposed unit displacement

$$u(\theta) = \frac{a_0}{2} + \sum_{k=1}^n (a_k \cos k\theta + b_k \sin k\theta) \tag{26}$$

where the Fourier coefficients $a_k, k=0,1,2,\dots,n$ and $b_k, k=1,2,\dots,n$ are given by

$$a_k = \frac{1}{\pi} \int_{-\pi}^{\pi} u(\theta) \cos k\theta \, d\theta, \quad b_k = \frac{1}{\pi} \int_{-\pi}^{\pi} u(\theta) \sin k\theta \, d\theta \tag{27}$$

Each of these Fourier coefficients corresponds to the symmetric and anti-symmetric displacement of node i for a particular Fourier term on the discretized line. Having the corresponding stiffness matrix for each particular Fourier series, one could find the loading contribution as:

$$f^s(\omega, k) = \mathbf{S}^s(\omega, k) \mathbf{u}_k^s(\omega, k), \quad \mathbf{u}_k^s = \{0, 0 \dots a_k \dots 0\}^T \quad k = 0, 1, 2, \dots \tag{28a}$$

$$f^a(\omega, k) = \mathbf{S}^a(\omega, k) \mathbf{u}_k^a(\omega, k), \quad \mathbf{u}_k^a = \{0, 0 \dots b_k \dots 0\}^T \tag{28b}$$

where \mathbf{u}_n^s are \mathbf{u}_n^a the displacement vectors of our discretized line which have only one non zero element on the corresponding degrees of freedom of node i (See Fig. 3). Superposing the results of forces for each term of Fourier series, the total forces for each particular position (θ, s) becomes obtainable with the help of the following equation:

$$\begin{Bmatrix} F_r(\theta, s) \\ F_z(\theta, s) \\ F_\theta(\theta, s) \end{Bmatrix} = \sum_{n=0}^{\infty} \{ \mathbf{F}_u^s(\theta, n) \mathbf{N}(s) \mathbf{f}^s(n) + \mathbf{F}_u^a(\theta, n) \mathbf{N}(s) \mathbf{f}^a(n) \} \tag{29}$$

Where $\mathbf{F}_u^s(\theta, n)$ and $\mathbf{F}_u^a(\theta, n)$ were given in Eq. (5), and $\mathbf{N}(s)$ is the one-dimensional finite-element shape functions.

The Eq. (29) should be set for each node on the near field/far field interface to obtain one column of total stiffness matrix due to the particular deformation in node i . This procedure shall be repeated for all degrees of freedom for all the nodes to obtain the total stiffness matrix.

In the frequency-domain, the interior FEM model is represented by the following finite element equation:

$$(\mathbf{K} - \omega^2 \mathbf{M}) \hat{\mathbf{u}} = \hat{\mathbf{P}} \tag{30}$$

with the static stiffness matrix \mathbf{K} , the mass matrix \mathbf{M} , the vector of unknown displacement amplitudes $\hat{\mathbf{u}}$ and the vector of nodal forces $\hat{\mathbf{P}}$. The system matrices and the nodal vectors are partitioned such that all degrees of freedom corresponding to the soil-structure interface are assembled in $\hat{\mathbf{u}}_b$, whereas all remaining interior degrees of freedom are denoted as $\hat{\mathbf{u}}_1$.

$$\left(\begin{bmatrix} \mathbf{K}_{ii} & \mathbf{K}_{ib} \\ \mathbf{K}_{bi} & \mathbf{K}_{bb} \end{bmatrix} - \omega^2 \begin{bmatrix} \mathbf{M}_{ii} & \mathbf{M}_{ib} \\ \mathbf{M}_{bi} & \mathbf{M}_{bb} \end{bmatrix} \right) \begin{bmatrix} \hat{\mathbf{u}}_i \\ \hat{\mathbf{u}}_b \end{bmatrix} = \begin{bmatrix} \hat{\mathbf{P}}_i \\ \hat{\mathbf{P}}_b \end{bmatrix} - \begin{bmatrix} \mathbf{0} \\ \hat{\mathbf{R}}_b \end{bmatrix} \tag{31}$$

Here, the vector of nodal forces $\hat{\mathbf{P}}$ is split into contributions due to external loads $\hat{\mathbf{P}}_{ex} = [\hat{\mathbf{P}}_i \ \hat{\mathbf{P}}_b]^T$ and due to the coupling forces $\hat{\mathbf{R}}_b$. The external loads are partitioned into the interior loads $\hat{\mathbf{P}}_i$ and interface loads $\hat{\mathbf{P}}_b$. This is illustrated in Figure 4. The dynamic stiffness matrix $\mathbf{S}^\infty(\omega^*, \xi = 1)$ relates the amplitudes of the coupling forces to the amplitudes of the displacements at the near field/far field interface all in cylindrical coordinate. To obtain the coupling force vector $\hat{\mathbf{R}}_b(\theta, s)$ in cylindrical coordinate

$$\hat{\mathbf{R}}_b(\theta, s) = \mathbf{TS}^\infty(\omega^*, \xi = 1) \mathbf{T}^T \hat{\mathbf{u}}_b \tag{32}$$

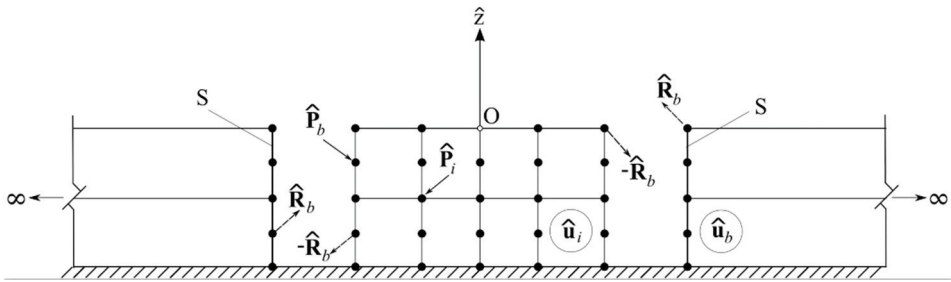


Figure 4 - FEM-SBFEM coupling: partitioning of degrees of freedom

Where the transformation matrix \mathbf{T} is for converting cylindrical to Cartesian coordinate. Substituting Eq. (32) into Eq. (31)

$$\begin{bmatrix} \mathbf{K}_{ii} - \omega^2 \mathbf{M}_{ii} & \mathbf{K}_{ib} - \omega^2 [\mathbf{M}_{ib}] \\ \mathbf{K}_{bi} - \omega^2 \mathbf{M}_{bi} & \mathbf{K}_{bb} - \omega^2 \mathbf{M}_{bb} + \mathbf{TS}^\infty(\omega^*, \xi = 1) \mathbf{T}^T \end{bmatrix} \begin{bmatrix} \hat{\mathbf{u}}_i \\ \hat{\mathbf{u}}_b \end{bmatrix} = \begin{bmatrix} \hat{\mathbf{P}}_i \\ \hat{\mathbf{P}}_b \end{bmatrix} \tag{33}$$

or

$$\mathbf{S}_G(\omega)\hat{\mathbf{u}}=\hat{\mathbf{P}}_{ex} \tag{34}$$

with the complex dynamic stiffness matrix $\mathbf{S}_G(\omega)$ of the coupled soil-structure system. Using Eq. (34), the displacement amplitudes of the near field due to time-harmonic external loads $\hat{\mathbf{P}}_{ex}$ can be calculated.

4. NUMERICAL EXAMPLES

In this section, dynamic response of various foundations has been calculated with respect to the aforementioned derivation. A combined 3D FEM-Axisymmetric SBFEM program has been developed in the MATLAB programming language. In the solution procedure, 3D 8-node isoparametric brick elements are used for the FE mesh and a conforming mesh of 2-node linear elements are utilized for the SBFEM. The mesh needed for modeling the structure are first created in ANSYS commercial software [48] and then imported into the program as input. The numerical results obtained using the proposed method is later compared to reference solutions. Stiffness coefficients are presented in numerical results which is defined by:

$$\mathbf{S}(a_0) = \mathbf{K}_{stat} (\mathbf{k}(a_0) + ia_0\mathbf{c}(a_0)) \tag{35}$$

In Eq. (35), the symbols \mathbf{K}_{stat} , $\mathbf{k}(a_0)$ and $\mathbf{c}(a_0)$ denote the static stiffness coefficient and the frequency-dependent spring and damping coefficient, respectively. The dimensionless frequency a_0 is defined as

$$a_0 = \omega \frac{r_0}{c_s} \tag{36}$$

where r_0 is a typical physical dimension of the foundation and c_s is the shear wave velocity, $c_s = \sqrt{G/\rho}$.

4.1. Rigid Circular Foundation on Homogeneous Soil Layer

A rigid, massless circular foundation of radius r_0 resting on a homogeneous soil layer of thickness $d=3r_0$ and Poisson’s ratio $\nu = 1/3$ is considered. The influence of the discretization on the static stiffness coefficient computed using the proposed method is studied. For the particular problem considered here, only the first two terms of the Fourier series is needed. Only the first term ($n=0$) is necessary for the analysis of vertical vibration (symmetric case) or torsional vibration (antisymmetric case), and only the second term ($n=1$) is needed for the study of horizontal or rocking vibration. The vertical, horizontal, rocking or torsional static stiffness coefficients of the rigid foundation computed using different meshes are summarized in Table 1. Four of these meshes are shown in Figure 5 for illustration purpose.

Good agreement between these reference solutions [30] and the numerical results is obtained modeling the near field with only 6 finite elements (discretization 2). Using this coarse mesh, the static stiffness coefficients calculated using the proposed method differ from the reference solutions by 8%, 8%, 9% and 23% for vertical, horizontal, rocking and torsional excitation, respectively. Table 1 provides the computed static stiffness coefficients that converge to the values given by Gazetas when the mesh is refined. Using discretization 4 (1430 finite elements, 12 scaled boundary elements), the vertical, horizontal, rocking and torsional stiffness coefficients obtained numerically differ from the reference solutions by only 4%, 1%, 1% and 11% respectively. This confirms that the derivation of the proposed axisymmetric SBFEM and the novel coupling method for three-dimensional layered systems is correctly implemented.

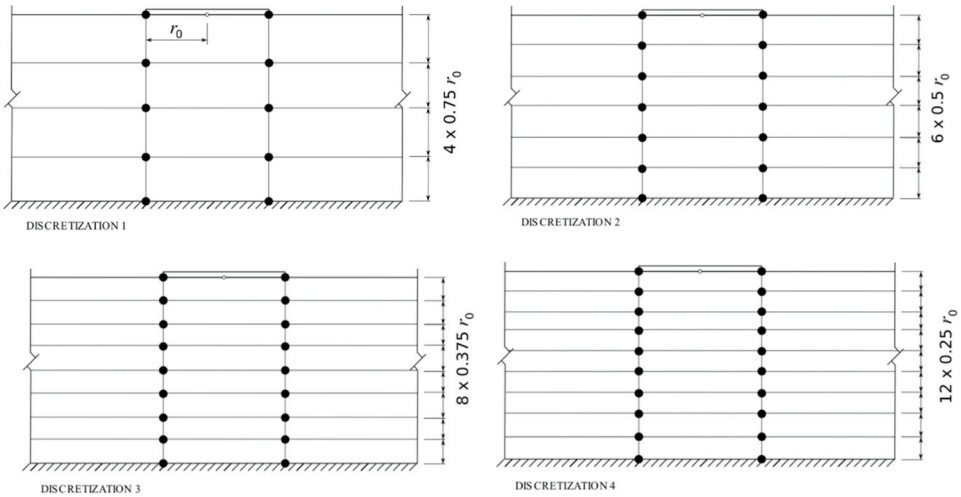


Figure 5 - Rigid circular foundation resting on homogeneous soil over rigid bedrock: Discretization 1 to 4

Table 1 - Convergence of static stiffness coefficients with decreasing mesh size

Discretization		Vertical	Horizontal	Rocking	Torsion
Nr.	Number of layers	$n=0$ $k_{stat,v}$ [Gor ⁰]	$n=1$ $k_{stat,h}$ [Gor ⁰]	$n=1$ $k_{stat,r}$ [Gor ³]	$n=0$ $k_{stat,t}$ [Gor ³]
1	4	9.541	6.430	4.907	7.221
2	6	9.213	6.060	4.603	6.570
3	8	9.052	5.870	4.449	6.258
4	12	8.882	5.667	4.285	5.948
Reference solution [30]		8.560	5.600	4.222	5.333

4.2. Rigid Circular Foundation on Homogeneous Soil Layer under Dynamic Load

Consider a rigid, massless circular foundation of radius r_0 which is resting on a homogeneous soil layer of thickness $d = r_0$ which the axisymmetric system is discretized using 10 2-node scaled boundary elements and 4752 8-node finite elements, as shown in Figure 6.

The computed dynamic spring and damping coefficients are given by Figures 7 and 8 for horizontal and vertical, rocking and torsional motion, respectively.

The numerically obtained static stiffness coefficients K_{stat} are summarized in Table 2.

The dynamic stiffness coefficients computed using the proposed method are compared to reference solutions, where original results were previously published in Ref. [28, 29].

In general, the dynamic stiffness coefficients of layered soil resting over bedrock are strongly frequency-dependent. The first three eigen frequencies of the homogeneous layer corresponding to propagating P-waves or shear waves, respectively, are given in Table 3.

As depicted in Figures 7 and 8, the cutoff-frequency and higher Eigen frequencies are represented accurately using the proposed method. For all four modes of vibration, the damping coefficient is zero below the cutoff-frequency (that is 1.571). In general, the stiffness coefficients computed using the proposed method agrees well with the reference solutions. For the horizontal vibration which is obtained from the second term of series ($n=1$), the curves produced using the proposed method are more different than those calculated using TLM. This could be due to the fact that solid elements produced by the ANSYS mesh generator [49] suffer from shear locking in numerical modelling while they have not been used in TLM. Moreover the components of coupled swaying-rocking stiffness could be defined differently with the results of TLM published in [29].

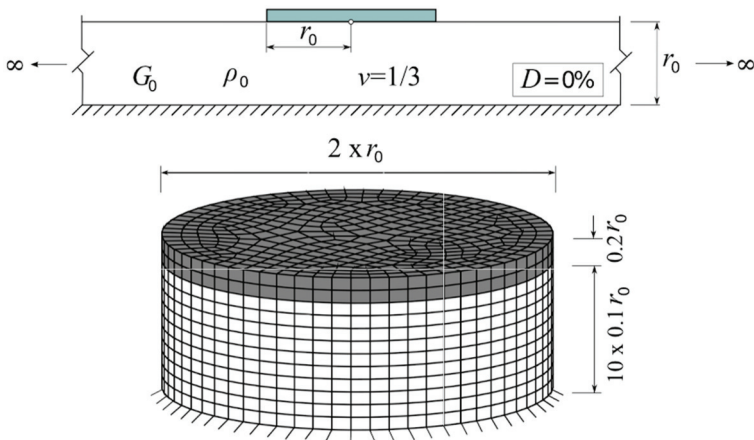


Figure 6 - Rigid circular foundation of radius r_0 resting on homogeneous soil layer of thickness $d = r_0$. System and discretization

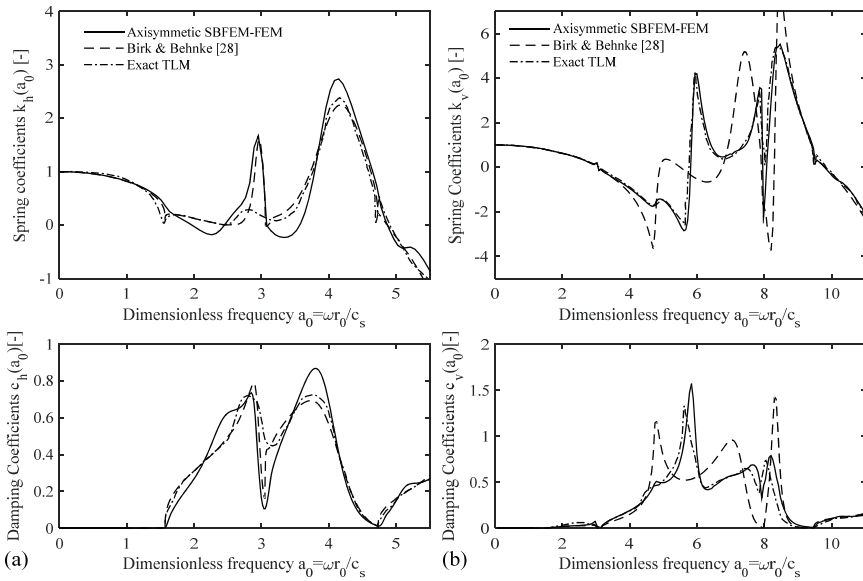


Figure 7 - Dynamic stiffness coefficients of rigid circular foundation of radius r_0 resting on a homogeneous soil layer of thickness d_0 : (a) horizontal ($n=1$), (b) vertical ($n=0$).

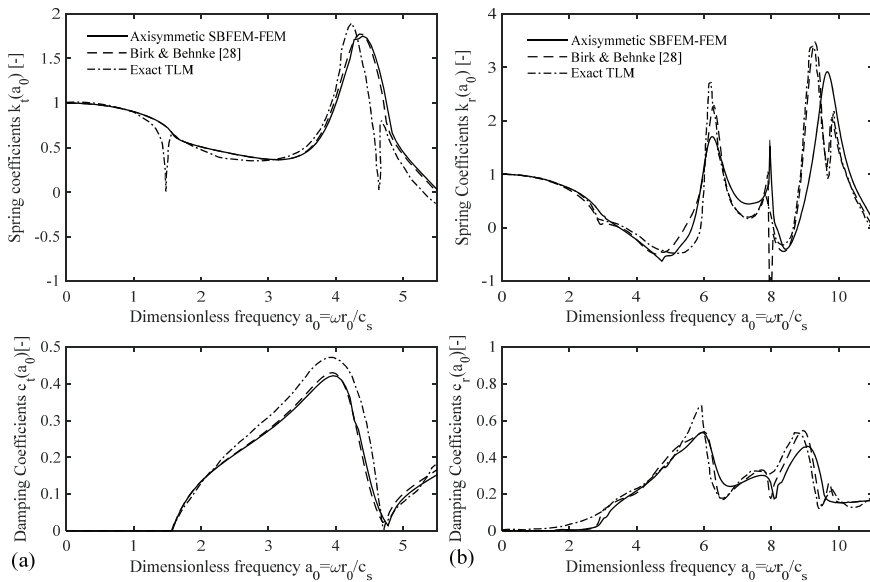


Figure 8 - Dynamic stiffness coefficients of rigid circular foundation of radius r_0 resting on a homogeneous soil layer of thickness d_0 : (a) torsion ($n=0$), (b) rocking ($n=1$).

Table 2 - Static stiffness coefficients of rigid circular foundation of radius r_0 resting on homogeneous soil layer of thickness $d=r_0$

	Vertical $k_{stat,v}$	Horizontal $k_{stat,h}$	Rocking $k_{stat,r}$	Torsion $k_{stat,t}$
Birk and Behnke [28]	15.927 G_0r_0	7.775 G_0r_0	5.514 $G_0r^3_0$	6.027 $G_0r^3_0$
Axisymmetric SBFEM-FEM	15.956 G_0r_0	8.081 G_0r_0	5.603 $G_0r^3_0$	6.124 $G_0r^3_0$

Table 3 - Dimensionless eigen frequencies of homogeneous soil layer of depth d

Eigen frequency j	Shear waves c_s horizontal and torsion	P-waves c_p vertical and rocking
1 (Cut-off frequency)	$\frac{1}{2}\pi = 1.570$	$\pi = 3.141$
2	$\frac{3}{2}\pi = 4.712$	$3\pi = 9.424$
3	$\frac{5}{2}\pi = 7.853$	$5\pi = 15.707$

4.3. Rigid Circular Foundation on Inhomogeneous Soil Layer

Considering a rigid circular foundation resting on a three parallel soil strata, as shown in Figure 9, the proposed method has been used to analyze a layered system with inhomogeneous material properties.

A constant hysteretic damping ratio of $D=0.05$ is assumed throughout the total thickness of the layer. This system has also been analyzed by Wolf and Preisig [18], and Birk and Behnke [28].

The soil depth has been discretized using 20 2-node scaled boundary elements and 7392 8-node finite elements. The corresponding mesh is shown in Figure 9.

Figure 10 shows the computed dynamic stiffness coefficients normalized using corresponding static stiffness.

The reference solutions shown in Figure 10 are the 'TLM exact' solutions published in Ref. [29] by thin-layer method and 3D-modifeid scaled boundary method published in Ref. [28].

The numerical results shown in Figure 10 agree well with the reference solutions.

Moreover, the explanation for deviation of horizontal vibration overlaps with the discussions made under section 4.2.

4.4. Rigid Circular Foundation Embedded in Homogeneous Soil Layer

A rigid circular foundation of radius r_0 is embedded with depth $t = r_0$ in a homogeneous soil layer of thickness $d = 3r_0$ with Poisson's ratio $\nu = 1/3$. Hysteretic damping of $D=0.05$ is assumed.

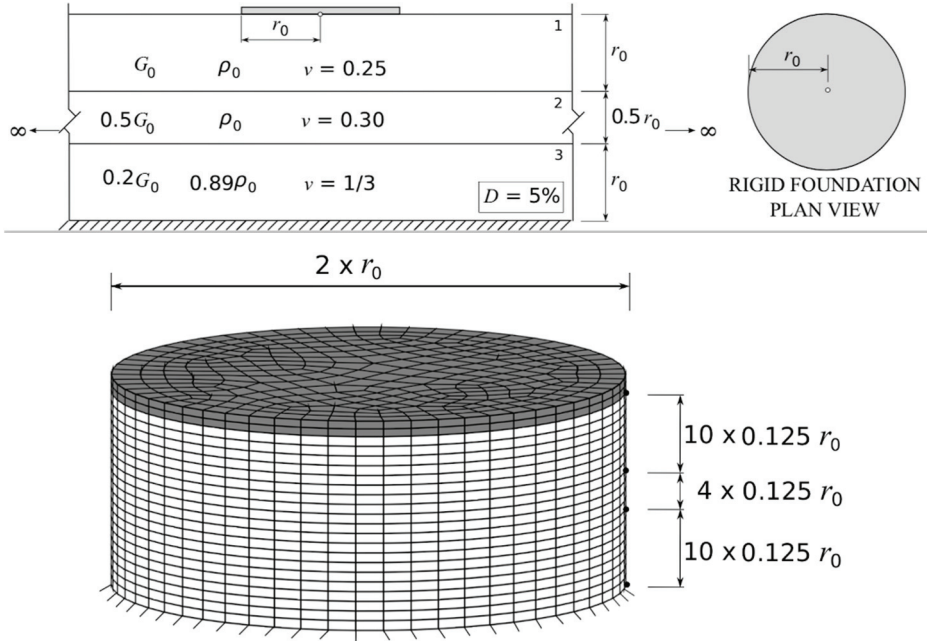


Figure 9 - Rigid circular foundation resting on inhomogeneous soil layer - discretization

The cylinder is modeled using 10 2-node scaled boundary elements and 440 8-nodes finite elements, as shown in Figure 11.

The static stiffness coefficients given in Refs. [18, 28] and the corresponding values calculated using the proposed method are summarized in Table 4.

The vertical and torsional dynamic stiffness coefficients which are calculated by using the proposed method are given in Figure 12.

These numerical results are compared to reference solutions which have been published in Refs. [18, 28]. The 'exact' solutions in Ref. [18] and in Figure 12 have been calculated by Emperor and Dominguez [50] using the boundary element method with a very fine discretization.

The agreement of the stiffness coefficient computed using the proposed method with the reference solutions based on the boundary element method and modified 3D SBFEM is found to be excellent.

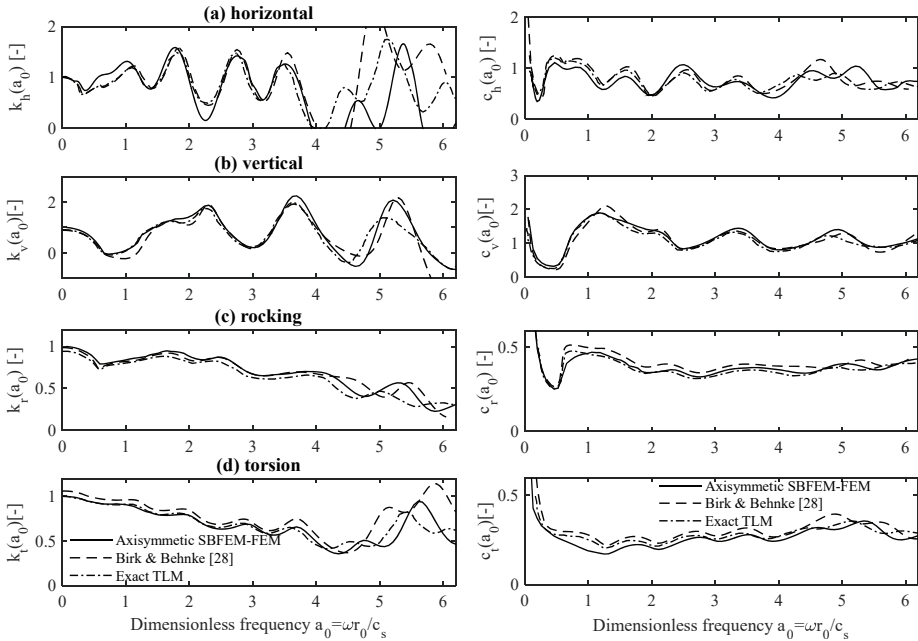


Figure 10 - Dynamic stiffness coefficients of rigid circular foundation of radius r_0 resting on inhomogeneous soil layer shown in Figure 9: (a) horizontal ($n=1$), (b) vertical ($n=0$), (c) rocking ($n=1$), (d) torsion ($n=0$).

4.5. Rigid Rectangular Foundation on Homogeneous Soil Layer

To demonstrate the suitability of the proposed method for dynamic analysis of arbitrary shape foundation and study the effect of Fourier series terms, a rigid rectangular foundation of $L/B=2$ on a homogenous soil layer is considered, where B and L are half width and half length of foundation respectively. A constant Hysteretic damping of $D=0.05$ is assumed. The rectangular foundation enclosed by a cylinder of radius= $3B$ which is the near field.

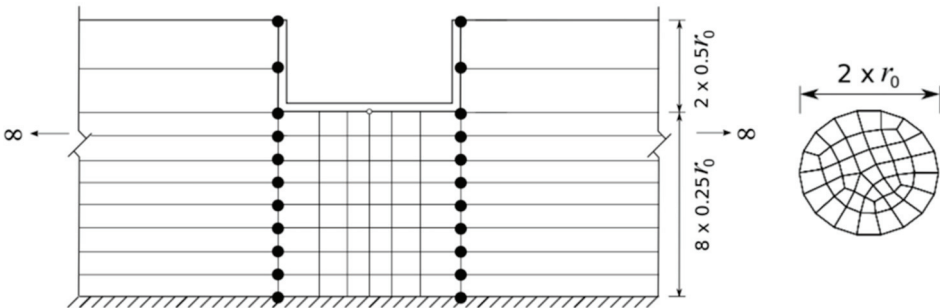


Figure 11 - Rigid circular foundation of radius r_0 embedded in homogeneous soil layer of thickness $d = 3r_0$ - discretization

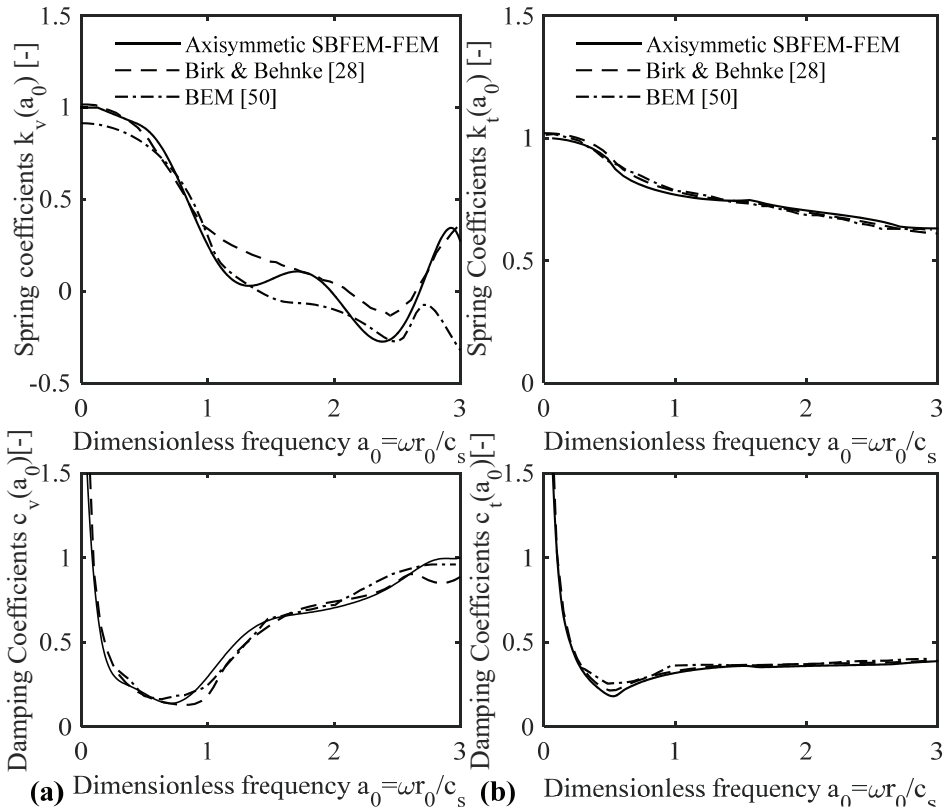


Figure 12 - Dynamic stiffness coefficients of rigid circular foundation of radius r_0 embedded with depth $t = r_0$ in homogeneous soil layer of depth $d = 3r_0$: (a) vertical ($n=0$), (b) torsion ($n=0$)

Two cases with different depth ratios ($h=4B$ and $6B$) are considered. The boundaries of these two systems have been discretized using 16 and 24 scaled boundary elements respectively (Figure 13).

Table 4 - Static stiffness coefficients of rigid circular foundation of radius r_0 embedded with depth $r=r_0$ in homogeneous soil layer of thickness $d=3r_0$

	Vertical $k_{stat,v}$	Torsion $k_{stat,s}$
Axisymmetric SBFEM- FEM	16.509 $G_0 r_0$	20.482 $G_0 r^3_0$
Wolf and Preisig [17]	16.14 $G_0 r_0$	20.22 $G_0 r^3_0$
Birk and Behnke [28]	14.771 $G_0 r_0$	20.641 $G_0 r^3_0$

Three terms of series are needed to accurately represent the problem. Figure 14 shows the numerically obtained vertical impedances for $n=2$ along with values obtained by other researcher. The other results were obtained using the boundary solution method by Chow [51] and 3D frequency-dependent infinite element method by Seo et al., [52]. The proposed solution is found to be close to the reference values. Obtained results revealed that for a rigid rectangular foundation under vertical pressure, the Fourier series terms up to $n=2$ is sufficient.

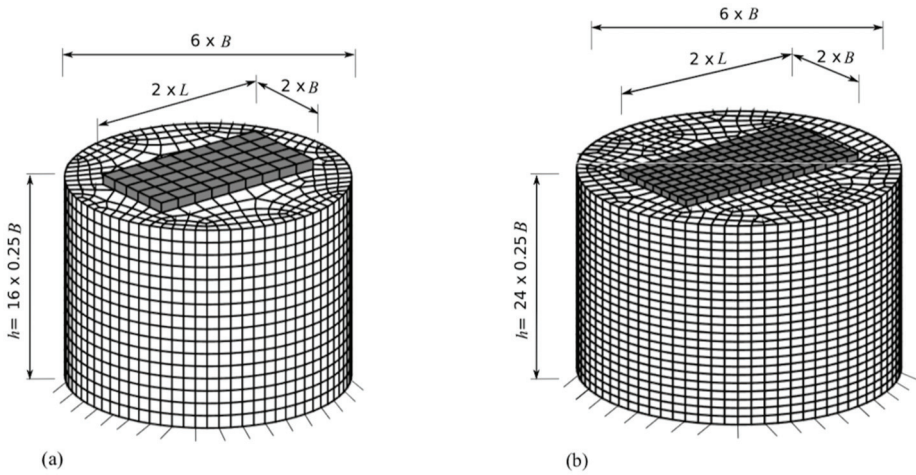


Figure 13 - Rigid rectangular foundation ($L=B=2$) resting on homogeneous soil layer - discretization: (a) $h/B = 4$, (b) $h/B = 6$

5. CONCLUSION

In this paper, an efficient computational model is presented for harmonic analysis of soil-structure interaction problem via a novel coupling of Axisymmetric SBFEM-3D FEM model.

It is based on deriving an axisymmetric scaled boundary finite element method for elastodynamic problems in three-dimensional layered media. Major differences both with respect to formulation and solution techniques occur with the original scaled boundary finite element method.

In the next step, the axisymmetric SBFEM formulation of unbounded domain will be coupled to the 3D finite element of the near field by a novel idea using the Fourier coefficients. The proposed method has been validated by calculating the static and dynamic stiffness of various foundation-soil systems.

The near field which can be of arbitrary complexity should be enclosed by a cylinder. Only the first term of series ($n=0$) is needed for the vertical and torsional vibration of rigid circular foundation, while for the horizontal and rocking vibration, the second term ($n=1$) should be used. The study demonstrate the need of three terms of Fourier series ($n=2$) for a rigid rectangular foundation.

To sum up, it can be said that the proposed method is very well suited for the frequency analysis of three-dimensional foundations of arbitrary shape, which are embedded in or resting on layered inhomogeneous soil.

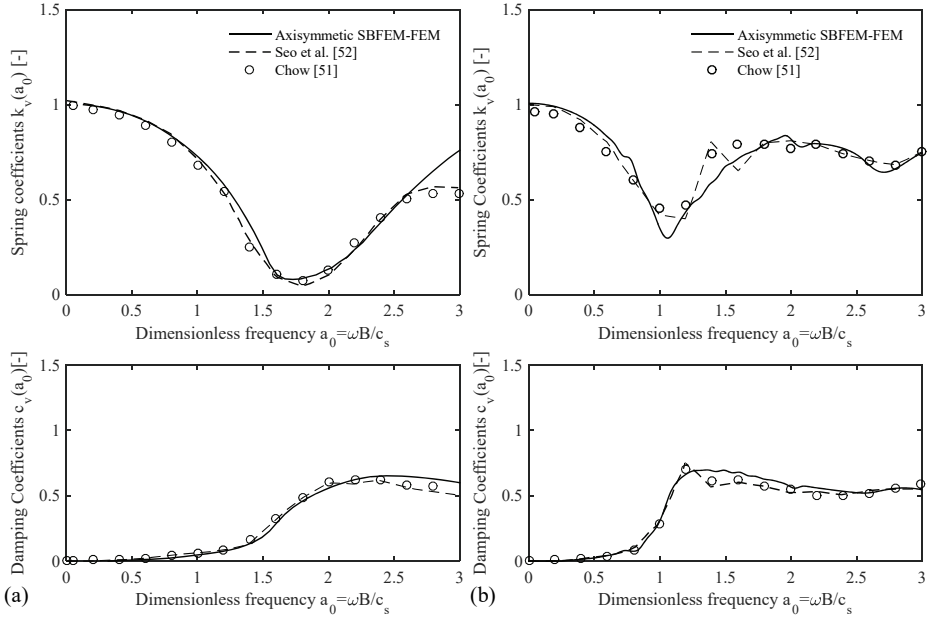


Figure 14 - Vertical impedances of rigid rectangular foundation resting on homogeneous soil layer ($L/B = 2$, $\nu = 0.33$, $D = 0.05$) (a) $h/B = 4$, (b) $h/B = 6$

Symbols

- ξ : Scaled radial coordinate
- ω : Angular frequency
- σ : Stress
- D : Constitutive matrix
- u : Displacement
- ε : Strain
- L : Differential operator in cylindrical coordinate
- \bar{L} : Equilibrium operator in cylindrical coordinate
- $N(s)$: Shape function matrix
- n : Term of Fourier series ($n \geq 0$)
- F_u^s, F_u^a : Symmetric and anti-symmetric trigonometric matrix

P^s, P^a	: Symmetric and anti-symmetric equivalent nodal force
E^{is}, E^{ia}	: Symmetric and anti-symmetric coefficient matrix ($0 \leq i \leq 5$)
M_0^s, M_0^a	: Symmetric and anti-symmetric mass matrix
S^s, S^a	: Symmetric and anti-symmetric stiffness matrix
a_k, b_k	: Fourier coefficients
f_k^s, f_k^a	: Symmetric and anti-symmetric loading vector of the discretized line
K	: Static stiffness matrix
M	: Mass matrix
\hat{P}	: Nodal force
\hat{R}_b	: Coupling force
\hat{P}_{ex}	: External loads
\hat{P}_i	: Interior loads
\hat{P}_b	: Interface loads
T	: Transformation matrix
a_0	: Dimensionless frequency
G	: Shear modulus
ρ	: Density
ν	: Poisson's ratio
c_s	: Shear Wave velocity
K_{stat}	: Static stiffness coefficient

Acknowledgements

The first author (M.A.) would like to thank professor Carolin Birk from the university of Duisburg-Essen for her brilliant ideas, supportive and respectful supervision during the author's visit in 2017. Dr. Hauke Gravenkamp is to be acknowledged gratefully for his considerable contribution and support in the computer programming.

References

- [1] Kausel E., "Local transmitting boundaries", *Journal of engineering mechanics*, 114(6), 1011–1027, 1988.
- [2] Givoli D., "Non-reflecting boundary conditions: a review", *Journal of Computational Physics*, 8, 1–29, 1991.

- [3] Givoli D., Numerical methods for problems in infinite domains. vol. 33, Elsevier, 2013.
- [4] Tsynkov S.V., “Numerical solution of problems on unbounded domains. a review”, Applied Numerical Mathematics, 27(4), 465–532, 1998.
- [5] Givoli D., “High-order local non-reflecting boundary conditions: a review”, Wave motion, 39(4), 319–326, 2004.
- [6] Astley R.J., “Infinite elements for wave problems: a review of current formulations and an assessment of accuracy”, International Journal for Numerical Methods in Engineering, 49, 951–976, 2000.
- [7] Karabalis D.L., and Mohammadi M., “3-D dynamic foundation-soil-foundation interaction on layered soil”, Soil Dynamics and Earthquake Engineering, 17(3), 139 – 152, 1998.
- [8] Bouchon M., “A simple method to calculate Green’s functions for elastic layered media”, Bulletin of the Seismological Society of America, 71(4), 959 – 971, 1981.
- [9] Schmid G., Willms G., Huh Y., and Gihardt M., “SSI 2D/3D soil structure interaction: Ein Programmsystem zur Berechnung von Bauwerk-Boden-Wechselwirkungsproblemen mit der Randelementmethode”, Wissenschaftliche Mitteilungen, Nr. 12, SFB 151, Ruhruniversität Bochum, 1988.
- [10] Lysmer J., and Waas G., “Shear waves in plane infinite structures”, Journal of the Engineering Mechanics Division, 98(EM1), 85–105, 1972.
- [11] Kausel E., and Roesset J.M., “Dynamic stiffness of circular foundations”, Journal of the Engineering Mechanics Division, 101, 771–785, 1975.
- [12] Kausel E., and Peek R., “Dynamic loads in the interior of a layered stratum: An explicit solution”, Bulletin of the Seismological Society of America, 72, 1459–1480, 1982.
- [13] Kausel E., “Wave propagation in anisotropic layered media”, International Journal for Numerical Methods in Engineering, 23, 1567–1578, 1986.
- [14] Seale S.H., and Kausel E., “Point loads in cross-anisotropic layered half spaces”, Journal of Engineering Mechanics, 115, 509– 524, 1989.
- [15] Kausel E., “Thin-layer method: formulation in the time domain”, International Journal for Numerical Methods in Engineering, 37, 927–941, 1994.
- [16] Meek J.W., and Wolf J.P., “Cone models for soil layer on rigid rock. II”, Journal of Geotechnical Engineering, 118, 686–703, 1992.
- [17] Wolf J.P., and Paronesso A., “Lumped-parameter model for a rigid cylindrical foundation embedded in a soil layer on rigid rock”, Earthquake Engineering and Structural Dynamics, 21, 1021–1038, 1992.
- [18] Wolf J.P., and Preisig M., “Dynamic stiffness of foundation embedded in layered halfspace based on wave propagation in cones”, Earthquake Engineering and Structural Dynamics, 32(7), 1075 – 1098, 2003.

- [19] Pradhan P.K., Baidya D.K., and Ghosh D.P., “Dynamic response of foundations resting on layered soil by cone model”, *Soil Dynamics and Earthquake Engineering*, 24(6), 425 – 434, 2004.
- [20] Baidya D.K., Muralikrishna G., and Pradhan P.K., “Investigation of foundation vibrations resting on a layered soil system”, *Journal of Geotechnical and Geoenvironmental Engineering*, 132(1), 116 – 123, 2006.
- [21] Anam I., and Roësset J.M., “Dynamic stiffness of surface foundations: An explicit solution”, *International Journal of Geomechanics*, 4(3), 216–223, 2004.
- [22] Nogami T., Mahbub A.A., and Chen S.H., “A new method for formulation of dynamic responses of shallow foundations in simple general form”, *Soil Dynamics and Earthquake Engineering*, 25(7-10), 679 – 688, 2005.
- [23] Gazetas G., “Static and dynamic displacements of foundations on heterogeneous multilayered soils”, *Géotechnique*, 30(2), 159 – 177, 1980.
- [24] Andersen L., and Clausen J., “Impedance of surface footings on layered ground”, *Computers and Structures*, 86(1-2), 72 – 87, 2008.
- [25] Bouchon M., “A simple method to calculate Green’s functions for elastic layered media”, *Bulletin of the Seismological Society of America*, 71(4), 959-971, 1981.
- [26] Luco J.E., and Apsel R.J., “On the Green’s functions for a layered half-space. Part I”, *Bulletin of the Seismological Society of America*, 73(4), 909–929, 1983.
- [27] Apsel R.J., and Luco J.E., “On the Green’s functions for a layered half-space. Part II”, *Bulletin of the Seismological Society of America*, 73(4), 931–951, 1983.
- [28] Birk C., and Behnke R., “A modified scaled boundary finite element method for three-dimensional dynamic soil-structure interaction in layered soil”, *International Journal for Numerical Methods in Engineering*, 89(3), 371–402, 2012.
- [29] Wolf J.P., *Foundation Vibration Analysis Using Simple Physical Models*, Prentice-Hall, Englewood Cliffs NJ, 1994.
- [30] Gazetas G., “Analysis of machine foundation vibrations: State of the art”, *Soil Dynamics and Earthquake Engineering*, 2(1), 2 – 42, 1983.
- [31] Wolf J.P., *The Scaled Boundary Finite Element Method*, Wiley & Sons: Chichester, 2003.
- [32] Genes M.C., and Kocak S., “Dynamic soil-structure interaction analysis of layered unbounded media via a coupled finite element/ boundary element/scaled boundary finite element model”, *International Journal for Numerical Methods in Engineering*, 62(6), 798–823, 2005.
- [33] Genes M., and Kocak S., “A combined finite element based soil-structure interaction model for large-scale systems and applications on parallel platforms”, *Engineering Structures*, 24(9), 1119–1131, 2002.

- [34] Genes M.C., “Dynamic analysis of large-scale SSI systems for layered unbounded media via a parallelized coupled finite element/ boundary-element/scaled boundary finite-element model”, *Engineering Analysis with Boundary Elements*, 36(5), 845–857, 2012.
- [35] Yaseri A., Bazyar M., and Hataf N., “3D coupled scaled boundary finite-element/finite-element analysis of ground vibrations induced by underground train movement”, *Computers and Geotechnics*, 60, 1–8, 2014.
- [36] Syed N.M., and Maheshwari B.K., Improvement in the computational efficiency of the coupled FEM-SBFEM approach for 3D seismic SSI analysis in the time domain. *Computers and Geotechnics*, 67, 204–212, 2015.
- [37] Rahnema H., Mohasseb S., and JavidSharifi B., “2-D soil-structure interaction in time domain by the SBFEM and two non-linear soil models”, *Soil Dynamics and Earthquake Engineering*, 88,152–175, 2016.
- [38] Li B., Cheng L., Deeks A.J., and Teng B., “A modified scaled boundary finite-element method for problems with parallel side-faces. Part I. Theoretical developments”, *Applied Ocean Research*, 27(4 - 5), 216 – 223, 2005.
- [39] Lin G., Du J., and Hu Z., “Dynamic dam-reservoir interaction analysis including effect of reservoir boundary absorption”, *Science in China Series E: Technological Sciences*, 50, 1 – 10, 2007.
- [40] Doherty J.P, and Deeks A.J., “Scaled boundary finite-element analysis of a non-homogeneous elastic half-space”, *International journal for numerical methods in engineering*, 57(7), 955–973, 2003.
- [41] Aslmand M., Kani I.M., Birk C., Gravenkamp H., Krome F., Ghadi M.E., “Dynamic soil-structure interaction in a 3D layered medium treated by coupling a semi-analytical axisymmetric far field formulation and a 3D finite element model” *Soil Dynamics and Earthquake Engineering*, 115, 531-544, 2018.
- [42] Sommerfeld A. *Partial Differential Equations in Physics*, Academic Press: New York, 1949.
- [43] Guzina B.B., Fata S.N., and Bonnet M., “On the stress-wave imaging of cavities in a semi-infinite solid”, *International Journal of Solids and Structures*, 40, 1505–1523, 2003.
- [44] Madyarov A.I., and Guzina B.B., “A radiation condition for layered elastic media”, *Journal of Elasticity*, 82, 73–98, 2006.
- [45] Song C., and Wolf J.P., “The scaled boundary finite-element method – alias consistent infinitesimal finite-element cell method – for elastodynamics”, *Computer Methods in Applied Mechanics and Engineering*, 147, 329–355, 1997.
- [46] Laub A.J., “A Schur method for solving algebraic Riccati equations”, *IEEE Transactions on Automatic Control* 1979, 24(6):913–921.
- [47] Bartels R.H., and Stewart G.W., “Solution of the equation $AX+XB=C$ ”, *Communications of the ACM* 15, 9, 820-826, 1972.

- [48] Ansys computer program, Ansys Inc. Version 18.0, 2016.
- [49] Sun E.Q. Shear locking and hourglassing in msc nastran, abaqus, and ansys, Msc software users meeting, 2006.
- [50] Emperador J.M., and Dominguez J., “Dynamic response of axisymmetric embedded foundations”, *Earthquake Engineering and Structural Dynamics*, 18(8), 1105 – 1117, 1989.
- [51] Chow Y., “Vertical vibration of three-dimensional rigid foundations on layered media”, *Earthquake engineering & structural dynamics*, 15(5), 585–594, 1987.
- [52] Seo C.G., Yun C.B., and Kim J.M., “Three-dimensional frequency-dependent infinite elements for soil–structure interaction”, *Engineering Structures*, 29(11), 3106–3120, 2007.

TEKNİK DERGİ MANUSCRIPT DRAFTING RULES

1. The whole manuscript (text, charts, equations, drawings etc.) should be arranged in Word and submitted in ready to print format. The article should be typed on A4 (210 x 297 mm) size paper using 10 pt (main title 15 pt) Times New Roman font, single spacing. Margins should be 40 mm on the left and right sides and 52.5 mm at the top and bottom of the page.
2. Including drawings and tables, articles should not exceed 25 pages, technical notes 6 pages.
3. Your contributed manuscript must be sent over the DergiPark system. (<http://dergipark.gov.tr/tekderg>)
4. The text must be written in a clear and understandable language, conform to the grammar rules. Third singular person and passive tense must be used, and no inverted sentences should be contained.
5. Title must be short (10 words maximum) and clear, and reflect the content of the paper.
6. Sections should be arranged as: (i) abstract and keywords, (ii) title, abstract and keywords in the other language, (iii) main text, (iv) symbols, (v) acknowledgements (if required) and (vi) references.
7. Both abstracts should briefly describe the object, scope, method and conclusions of the work and should not exceed 100 words. If necessary, abstracts may be re-written without consulting the author. At least three keywords must be given. Titles, abstracts and keywords must be fitted in the first page leaving ten line space at the bottom of the first page and the main text must start in the second page.
8. Section and sub-section titles must be numbered complying with the standard TS1212.
9. Symbols must conform to the international rules; each symbol must be defined where it appears first, additionally, a list of symbols must be given in alphabetic order (first Latin, then Greek alphabets) at the end of the text (before References).
10. Equations must be numbered and these numbers must be shown in brackets at the end of the line.
11. Tables, drawings and photographs must be placed inside the text, each one should have a number and title and titles should be written above the tables and below the drawings and photographs.
12. Only SI units must be used in the manuscripts.
13. Quotes must be given in inverted commas and the source must be indicated with a reference number.
14. Acknowledgement must be short and mention the people/ institutions contributed or assisted the study.
15. References must be numbered (in brackets) in the text referring to the reference list arranged in the order of appearance in the text. References must include the following information:
If the reference is an article: Author's surname, his/her initials, other authors, full title of the article, name of the journal, volume, issue, starting and ending pages, year of publication.
Example : Naghdi, P. M., Kalnins, A., On Vibrations of Elastic Spherical Shells. J. Appl. Mech., 29, 65-72, 1962.
If the reference is a book: Author's surname, his/her initials, other authors, title of the book, volume number, editor if available, place of publication, year of publication.
Example : Kraus. H., Thin Elastic Shells, New York. Wiley, 1967.
If the reference is a conference paper: Author's surname, his/her initials, other authors, title of the paper, title of the conference, location and year.
If the source is a thesis: Author's surname, his/her initials, thesis title, level, university, year.
If the source is a report: Author's surname, his/her initials, other authors, title of the report, type, number, institution it is submitted to, publication place, year.
16. Discussions to an article published in Teknik Dergi should not exceed two pages, must briefly express the addressed points, must criticize the content, not the author and must be written in a polite language. Authors' closing remarks must also follow the above rules.
17. A separate note should accompany the manuscript. The note should include, (i) authors' names, business and home addresses and phone numbers, (ii) brief resumes of the authors and (iii) a statement "I declare in honesty that this article is the product of a genuinely original study and that a similar version of the article has not been previously published anywhere else" signed by all authors.
18. Copyright has to be transferred to UCTEA Turkish Chamber of Civil Engineers. The standard copyright form signed by the authorised author should therefore be submitted together with the manuscript.

CONTENTS

Effects of Mixing Temperature on the Mechanical Properties of Hot Mix Asphalt... 9221 Gül BALIK, Mehmet YILMAZ, Baha Vural KÖK, Taner ALATAŞ	
Examination of the Efficiency of Retrofitting Methods through Fragility Analysis .. 9243 Murat S. KIRÇIL, Erdem Çağlar KOCABEY	
Timber Floors and Strengthening Techniques (Illustrated With a Numerical Example)..... 9261 Žiga UNUK, Miroslav PREMROV, Vesna ŽEGARAC LESKOVAR	
Rotary Inertia and Higher Modes Effect on the Dynamic Response of Timoshenko Beams on Two-Parameter Elastic Foundation..... 9289 Çağlayan HIZAL, Hikmet Hüseyin ÇATAL	
Roughness Coefficient of a Highly Calcinated Penstock 9309 Kutay ÇELEBIOĞLU	
Efficient Dynamic Analysis of Foundation via a Coupled Axisymmetric SBFEM-3D FEM..... 9327 Mojtaba ASLMAND, Iradj Mahmoudzadeh KANI, Mehmet Cemal GENES	